Optical/IR interferometry: history and basic principles

Jean Surdej[1,2,*]

[1]Institute of Astrophysics and Geophysics, Liège University, Allée du 6 Août 19c, 4000 Liège, Belgium
[2]Astronomical Observatory Institute, Poznań Adam Mickiewicz University, Poland

Abstract. The present notes refer to a series of lectures delivered in September 2017 in Roscoff (France) during the 2017 Evry Schatzman School, at IUCAA (Inter-University Center for Astronomy and Astrophysics, Pune, India) in April 2018, during the July-September 2020 period and during the November 2020-January 2021 period via on-line lectures organized by IUCAA and by the Astronomical Observatory Institute, Adam Mickiewicz University in Poznań, respectively. It concerns a general introduction to optical/IR interferometry, including a brief history, a presentation of the basic principles, some important theorems and relevant applications. The layout of these lecture notes is as follows. After a short introduction, we proceed with some reminders concerning the representation of a field of electromagnetic radiation. We then present a short history of interferometry, from the first experiment of Fizeau and Stefan to modern optical interferometers. A first intuitive approach of the Zernicke-van Cittert theorem is proposed. We then discuss the notions of light coherence, including a rigorous demonstration of the theorem of Zernicke-van Cittert and describe the principle of interferometry using two telescopes. We present some examples of modern interferometers and observational results obtained with these. Finally, we address three important theorems: the fundamental theorem, the convolution theorem and the Wiener-Khinchin theorem which enable to get a better insight into the field of optical/IR interferometry.

*e-mail: jsurdej@uliege.be

1 Introduction

In the absence of the Earth atmosphere above a ground-based telescope equipped with a mirror having a diameter D_1, Figure 1 illustrates the image one would observe from a point-like star recorded in the focal plane in monochromatic light at a wavelength λ. It is a dot of light, the well-known Airy disc, which angular radius measured in radian is simply given by 1.22 λ/D_1. Unfortunately, the Airy disc does not contain any information relative to the star being imaged, irrespective of its size, shape, effective temperature, luminosity, distance, etc. A larger telescope with a diameter $D_2 > D_1$, would similarly lead to a smaller Airy disc (1.22 λ/D_2) of light for the star being imaged (see Fig. 2), providing a slightly better angular resolution image but with no more specific information related to the star. While observing an extended celestial source (cf. a distant resolved Earth-like planet as shown in Fig. 3), more details are seen with the telescope having a larger diameter. The dream of astronomers is therefore to construct always larger telescopes but presently there is a limit (D ~ 40m) over which it is technologically difficult to construct a single mirror telescope (cf. the ELT, TMT, GMT projects).

Fortunately, in 1868 Fizeau and Stephan just realized that "In terms of angular resolution, two small apertures distant of B are equivalent to a single large aperture of diameter B." (see Fig. 4). This is actually the subject of the present course: to understand how it is possible to reconstruct high angular resolution images of a distant celestial source using modern optical/IR interferometers such as VLTI, CHARA, etc. In fact, the image of a distant star that one would see in the focal plane of a Fizeau-type interferometer is no longer just an Airy disc due to each single telescope aperture but a brighter Airy disc superimposed with a series of interference fringes, alternately bright and dark, perpendicularly oriented with respect to the line joining the two telescopes and with an inter-fringe angular separation equal to λ/B, where B is the baseline of the interferometer (see Fig. 5). This naturally leads to the hope that it will be possible to retrieve along the direction of the baseline having a length B an angular resolution that is equivalent to that of a single dish telescope having a diameter B. As a summary, figure 6 illustrates the improvement expected in angular resolution while observing an extended celestial source with telescopes of increasing size ($D_2 > D_1$) and with an interferometer composed of two telescopes separated by a distance $B > D$.

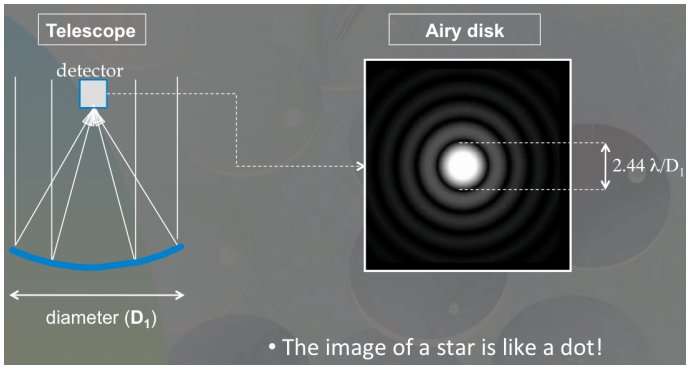

Figure 1. Airy disc of a point-like star recorded in the focal plane of a telescope with diameter D_1. The angular diameter of the Airy disc is 2.44 λ/D_1.

In mathematical terms, the convolution theorem states that the image I(ζ, η) we observe in the focal plane of an instrument (single dish telescope or interferometer) from a distant extended source as a function of its angular coordinates (ζ, η) is the convolution product of the real source image (cf. the extended Earth-like planet) O(ζ, η) by the point spread function PSF(ζ, η) of the telescope (i.e. the Airy disc, see Fig. 7) or of the interferometer (i.e. the Airy disc crossed by the interference fringes).

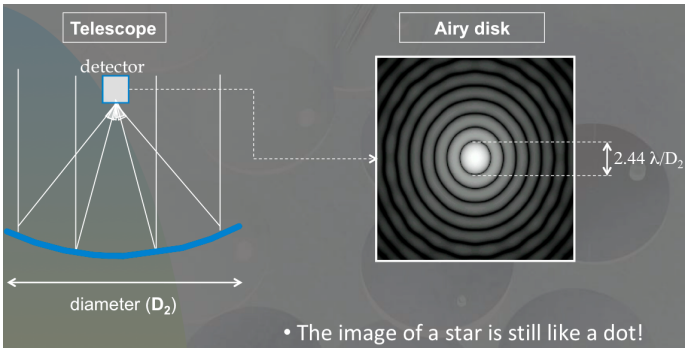

Figure 2. As the diameter of a telescope increases ($D_2 > D_1$), the Airy disc of a point-like star gets smaller.

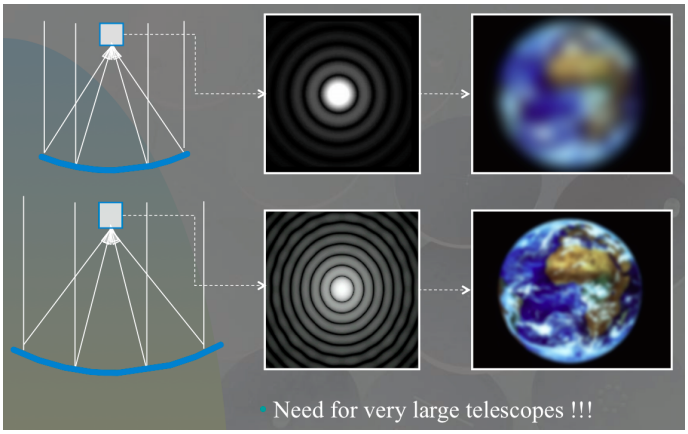

Figure 3. While observing an extended celestial object (cf. an Earth-like planet) above the atmosphere, we see more details as the diameter of the telescope increases.

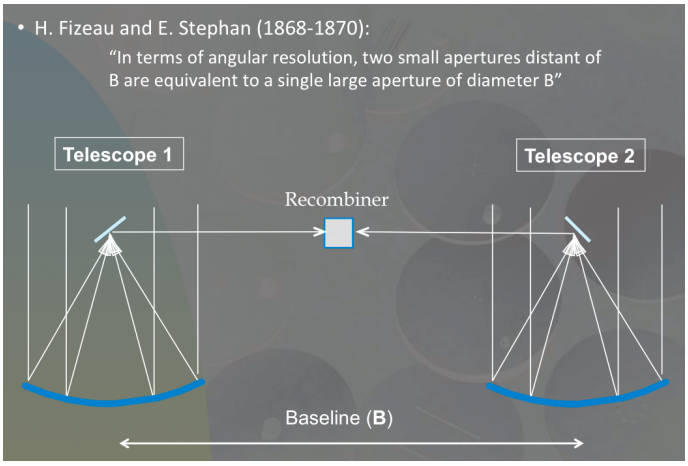

Figure 4. Fizeau and Stephan proposed to recombine the light from two independent telescopes separated by a baseline B to recover the same angular resolution as that given by a single dish telescope having a diameter B.

While taking the Fourier transform (FT) of the first expression given in Fig. 7, we find that $FT[I(\zeta,\eta)](u,v)$ is simply equal to the natural product of $FT[PSF(\zeta,\eta)](u,v)$ and $FT[O(\zeta,\eta)](u,v)$ where u,v represent the angular space frequencies defined as $u = B_u/\lambda$ and $v = B_v/\lambda$, respectively, where B_u and B_v correspond to the projected baselines of the interferometer along the directions parallel to the angles ζ,η. One can then expect that by just taking the inverse Fourier transform FT^{-1} of $FT[O(\zeta,\eta)](u,v)$, it will become possible to retrieve high angular resolution information about the extended source with an angular resolution

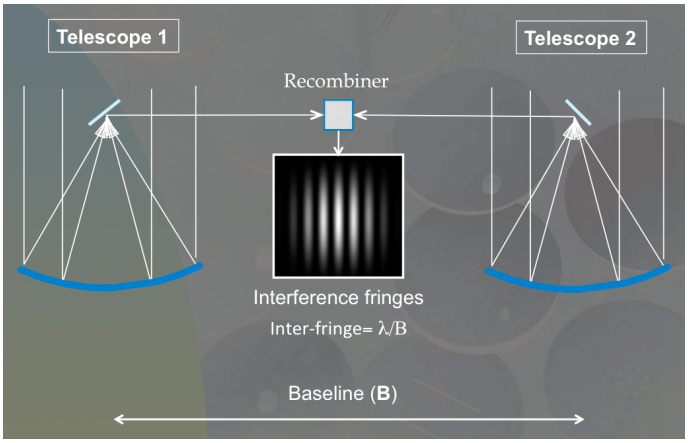

Figure 5. When recombining the monochromatic light of two independent telescopes, there results the formation of a pattern of bright and dark fringes superimposed over the combined Airy disc. The angular inter-fringe separation is equal to λ/B.

equivalent to $1/u = \lambda/B_u$ and $1/v = \lambda/B_v$, respectively:

$$O(\zeta,\eta) = FT^{-1}[FT[O(\zeta,\eta)](u,v)](\zeta,\eta) = FT^{-1}[\frac{FT[I(\zeta,\eta)](u,v)}{FT[PSF(\zeta,\eta)](u,v)}](\zeta,\eta). \qquad (1)$$

The quantity $FT[I(\zeta,\eta)](u,v)$ can be directly derived from the observation of the extended source with the optical/IR interferometer while the other quantity $FT[PSF(\zeta,\eta)](u,v)$ can be obtained from the observation of a point-like (unresolved) star. During the forthcoming lectures, we shall see that the Wiener-Khinchin theorem states that the latter quantity is also merely given by the auto-correlation function of the distribution of the complex amplitude of the radiation field in the pupil plane of the observing instrument being used (single dish telescope or interferometer). The goal of the present course is to establish and fully understand relations such as Eq. (1).

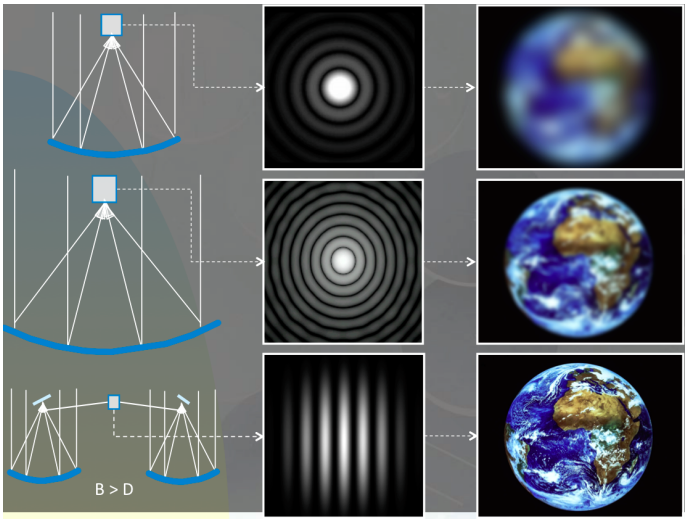

Figure 6. Improvement expected in angular resolution while observing an extended celestial source (cf. an Earth-like planet) with telescopes of increasing size ($D_2 > D_1$) and with an interferometer composed of two telescopes separated by a baseline $B > D$.

2 Some reminders

With a few exceptions (cf. the Moon, the Sun, the Andromeda Galaxy, etc.), all the celestial objects that we see in the sky appear to us, with the naked eye, as point-like objects. Apart

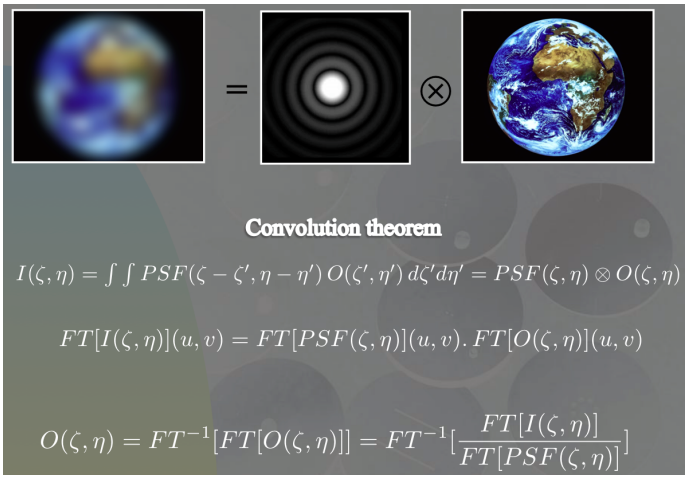

Figure 7. The image I(ζ, η) we observe in the focal plane of an instrument (cf. single dish telescope) from a distant extended source as a function of its angular coordinates (ζ, η) is the convolution product of the real source image (cf. the extended Earth-like planet, O(ζ, η)) by the point spread function PSF(ζ, η) of the telescope.

from their apparent motion with respect to the fixed stars on the celestial sphere, we are not even able to distinguish between the images of Jupiter, Saturn or even Venus from those of ordinary stars. We describe in this course an observation method based on the principle of a Fizeau-type interferometer, which allows with just some basic cooking equipment to resolve angularly a planet such as Venus, when it is at its maximum apparent brightness ($V \sim -4.4$).

If we assimilate for a moment the disc of a star, or even that of Venus, to the filament of a light bulb, the goal of the present course can still be formulated as follows: given a common electric light bulb inside which is a filament, having a certain thickness T (measured perpendicularly to the line-of-sight) and which is incandescent (cf. a star), how to measure the thickness T of this filament (diameter of the star) not only without breaking the bulb but also assuming that it is so far away from us, at a distance z, that it is not possible for us to angularly resolve the filament with the naked eye (see Fig. 8a)?

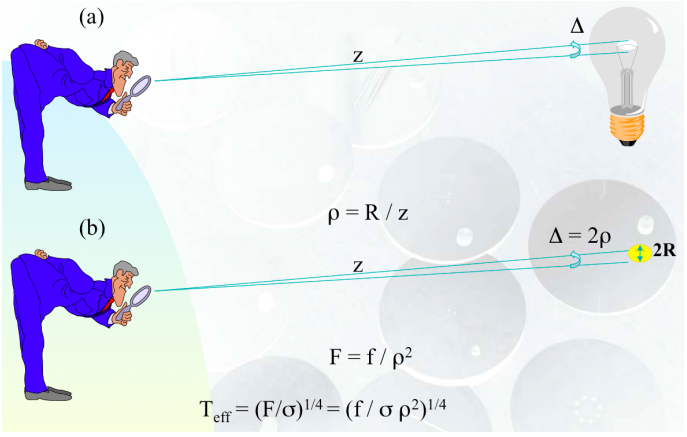

Figure 8. Resolving the angular diameter of a star (b) is alike trying to estimate the angular size of the filament of a light bulb (a).

Let us now recall that knowledge of the angular radius ($\rho = R/z$) of a star located at a distance z ($z >> R$) and having a linear radius R allows the direct determination of its flux F at the stellar surface from the flux f observed on Earth (as a reminder $F = f/\rho^2$, see Fig. 8b). If we can measure the absolute distance z of the star, we can also determine its linear radius R from its angular radius ρ ($R = \rho z$). Moreover, knowledge of the intrinsic flux F of the star allows an immediate determination of its effective temperature T_{eff}, thanks to the application

of the Stefan-Boltzmann law ($F = \sigma T_{eff}^4$). It then results that $T_{eff} = (f/\sigma\rho^2)^{1/4}$. The measurements of the angular radius and of the flux of a star measured on Earth thus lead to the determination of the effective temperature T_{eff} of that star. As a reminder, this temperature is directly involved in the construction of stellar atmosphere models and stellar evolution. We will also show that Fizeau-type stellar interferometry literally allows direct imaging with very high angular resolution of distant bodies by the method of aperture synthesis. Let us now proceed with a few theoretical reminders about the description of a field of electromagnetic light radiation.

2.1 Complex representation of an electromagnetic wave

Let us first remind that a beam of light radiation can be assimilated to the propagation of a multitude of electromagnetic waves at the speed of 299,792 $km\,s^{-1}$ in the vacuum. If, for the sake of simplicity, we assume that we deal with a plane monochromatic wave, linearly polarized, propagating along the direction of abscissa z, the electric field E at any point in space and at time t, can be represented by a sinusoidal type function taking for example the shape

$$E = a\ cos[2\pi(\nu t - z/\lambda)] \tag{2}$$

where

$$\lambda = c\ T = c/\nu \tag{3}$$

with c, λ, ν, T and a representing the speed of light, the wavelength, the frequency, the period and the amplitude of the electromagnetic vibrations, respectively (see Figure 9).

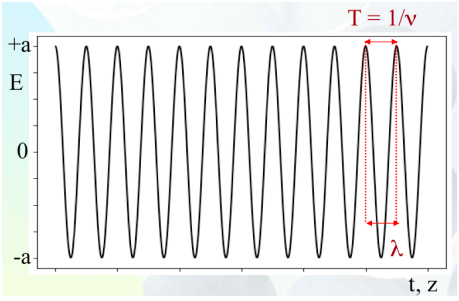

Figure 9. Representation of an electromagnetic wave.

We know how convenient it is to rewrite the previous equation in complex notation:

$$E = Re\{a\ \exp[i2\pi(\nu t - z/\lambda)]\} \tag{4}$$

where Re represents the real part of the expression between the two curly braces. This complex representation of an electromagnetic wave has the great advantage that the exponential function can now be expressed as the product of two functions depending separately on the spatial and temporal coordinates

$$E = a\ \exp(-i\phi)\ \exp(i2\pi\nu t) \tag{5}$$

where

$$\phi = 2\pi z/\lambda \tag{6}$$

just represents a phase shift.

If we suppose that all the operations that we carry out on the electric field E are linear, it is of course very convenient to use in our calculations its complex representation (see Eq.(5)) and to take at the end the real part of the result obtained.

We can then rewrite the previous equation as follows:

$$E = A\ \exp(i2\pi\nu t), \tag{7}$$

where

$$A = a\ \exp(-i\phi) \tag{8}$$

with A representing the complex amplitude of the vibration.

Because of the extremely high frequencies of electromagnetic waves corresponding to visible radiations ($\nu \sim 6\ 10^{14} Hz$ for $\lambda = 5000$ Å), we recall that it is not presently possible to make direct observations of the electric field E (the situation is different in the radio domain). The only measurable quantity is the intensity I, which is the time average of the amount of energy passing through a unit surface element, per unit of time and solid angle, placed perpendicularly to the direction of propagation of the light beam.

The intensity I being proportional to the temporal average of the square of the electric field, we find

$$I = \left\langle E^2 \right\rangle = lim_{T\to\infty} \frac{1}{2T} \int_{-T}^{+T} E^2 dt = \frac{1}{2T} \int_{-T}^{+T} A \exp(i2\pi\nu t)\ A^* \exp(-i2\pi\nu t)\, dt = A\ A^*. \tag{9}$$

The intensity of the radiation is thus simply defined by the relation:

$$I = A\ A^* = |A|^2 = a^2, \tag{10}$$

where a is the real amplitude of the electric field.

2.2 Principle of Huygens-Fresnel

We recall that, according to Huygens, each point of a wavefront can be considered as being the centre of a secondary wave leading to the formation of spherical wavelets, and that the main wavefront, at any subsequent moment can be considered as the envelope of all these wavelets (see Fig. 10).

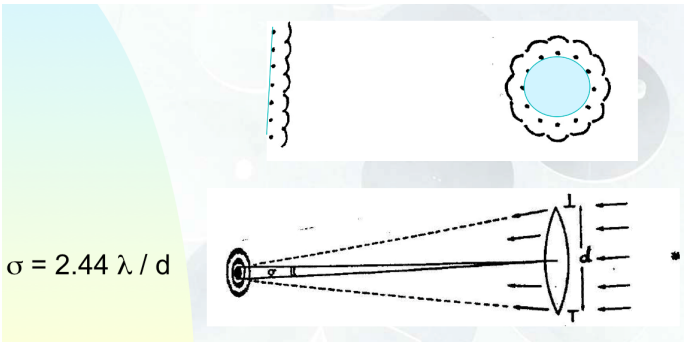

Figure 10. Illustration of the Huygens-Fresnel principle during the propagation of a plane or circular wavefront and diffraction of light which encounters a converging lens.

Using this model, Fresnel was the first to account for the observed effects of light diffraction, assuming that secondary wavelets interfere with each other. In accordance with this principle, the encounter of two waves oscillating with a same period T and which are in phase will result in a wave still oscillating with the period T and with an amplitude equal

to the summation of the two individual amplitudes. If they are oscillating in phase opposition, the resulting amplitude will be the difference between the two individual amplitudes. This combination of the Huygens construction method and the Fresnel interference principle is called the Huygens-Fresnel principle. This is the basis of the concept of the Fourier transform.

Let us remind a direct application of this principle when studying the formation of the image of a distant object at the focus of a telescope having a linear diameter d. Following the diffraction of the waves at the passage of the opening of the telescope (as if the waves were trying to spread and bypass the obstacles), we observe a phenomenon of redistribution of the energy of the light wave: the image of a point-like source produced by a converging circular objective (lens or mirror) is not a point but spreads in a diffraction pattern called the "Airy disc" (see Fig. 10). We shall demonstrate in Section 7 that the angular diameter of the central spot is (in radian):

$$\sigma = 2.44\,\lambda/d \tag{11}$$

where λ is the wavelength of light and d is the linear diameter of the aperture.

We can resolve an extended source by direct imaging, if and only if, its angular diameter Δ ($= 2\rho$) is somewhat larger than σ. For example, our pupil whose approximate diameter varies between 1 and 5 mm, allows us to angularly resolve nearby objects separated by more than 138" and 28", respectively. In the visible range, a telescope, with a diameter of 14 cm, will allow us to resolve objects with an angular dimension larger than 1", and for diameters larger than 14 cm, their collecting area will naturally be enhanced but their angular resolution will remain limited to (more or less) 1" because of the atmospheric agitation (see Fig. 11). In fact, under the influence of temperature and pressure gradients, a regime of eddies establishes itself in the Earth atmosphere which, at low altitude ($\sim$ 10 km), have dimensions of the order of 20 cm (sometimes only a few cm, sometimes 30 or 40 cm) and evolution periods of the order of a few milliseconds. Optically, these changes manifest themselves by an inhomogeneity in the refractive index distribution. The amplitude and the relative phase shift of the electromagnetic field in the pupil plane thus get disturbed in a random manner.

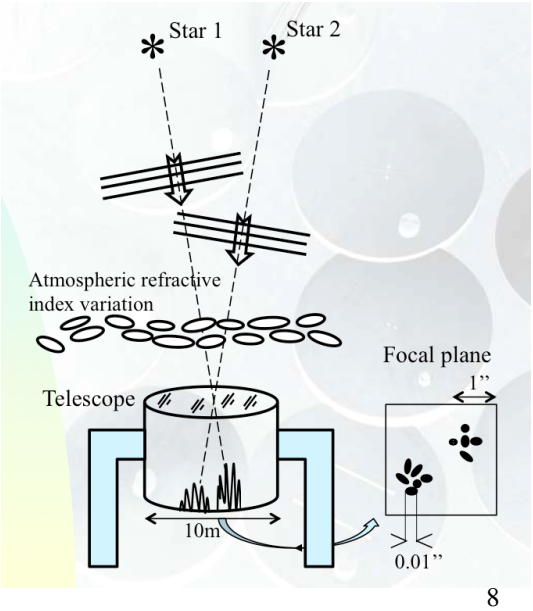

Figure 11. Atmospheric agitation above the objective of a large telescope causing the seeing effects seen in its focal plane.

It follows that if we observe the Moon, Jupiter, etc. either with the largest telescope in the world having a diameter of 10m (σ = 0.014") or with an amateur telescope with a diameter of 14 cm (σ = 1"), we will see the same details under good seeing conditions. The brightness will of course be larger with the 10m telescope ... but probably too bright for the eye not to be blinded by the image of the Moon or Jupiter.

The diffusion indicator of the atmosphere is defined as being the average inclination perturbation of the wave surfaces. This tilt disturbance reaches values that vary between 1" and 10", depending on the site and the moment. This phenomenon is detected differently according to the dimensions of the instrument used. The eye, which has an angular resolution close to one minute of arc, will be sensitive only to variations of amplitude: we then see stars flickering. An instrument of 10 to 20 cm in diameter will detect tilt variations and the focal image will oscillate around an average position. For larger instruments, a large number of eddies will, at the same time, be involved in the formation of the focal image. This will therefore have the dimensions of the diffusion indicator of the atmosphere. The spatial coherence of the entrance pupil will allow, for a point-like source, the realization of interference phenomena between the radiations passing through different points of the pupil. A statistical study makes it possible to show that the resulting focal image, delimited by the diffusion indicator, consists of a set of granules (called 'speckles') which smallest size is comparable to that of the Airy disc of the instrument (see Fig. 11). These granules swarm in the diffusion spot at the rhythm of the change of the atmospheric eddies. The stability of the focal image is therefore also of the order of the millisecond. The technique of speckle interferometry, developed by the French astronomer Antoine Labeyrie, allows to re-construct the images of the stars observed with the angular resolution given by the true diameter of the telescope.

3 Brief history about the measurements of stellar diameters

In the past, there have been numerous attempts to measure angular diameters of stars, and we will first recall three of these approaches that clearly show the difficulties encountered.

3.1 Galileo

A first experimental attempt to measure the angular diameter of stars was made by Galileo (1632). He proceeded as follows: placing himself behind a rigid wire (whose thickness D was known, see Fig. 12) suspended vertically, he determined the distance z to which he had to move in so that the image of the star Vega (α Lyrae) of magnitude zero got completely obscured by the wire (see Hughes, D. W. 2001, Journal of the British Astronomical Association, vol.111, no.5, p.266-270). Galileo deduced that the angular diameter of Vega, equal to that of the wire, was about 5", which was in itself a rather revolutionary result, since the value adopted at that epoch for the angular diameter of the stars was close to 2'. As we saw earlier, the value of 2' is certainly the result of the low angular resolution of our eye, while the 5" angular diameter measured by Galileo was the result of the effects of the atmospheric agitation (seeing effects) at the time of his observations.

3.2 Newton

A theoretical estimate of the angular dimension of a star of magnitude zero (cf. that of the star Vega) was performed by Newton. His approach was as follows: if we suppose that the Sun, located at a distance $z_\odot$ (approximately 150 million km) with an apparent magnitude $V_\odot = -26.7$, is a star similar to the stars situated on the celestial sphere and if we place our

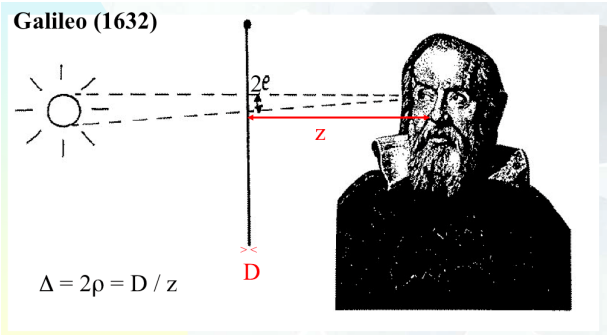

Figure 12. Experimental measurement by Galileo of the angular diameter of a star (see text).

Sun at a distance z such that its apparent brightness becomes comparable to that of a star of magnitude equal to zero, then its angular diameter Δ should be easy to derive. Indeed, we successively find

$$\begin{aligned} V_\odot - 0 &= -2.5 \log_{10}\left(\frac{\frac{L_\odot}{z_\odot^2}}{\frac{L_\odot}{z^2}}\right), \\ V_\odot &= 5 \log_{10}\left(\frac{z_\odot}{z}\right), \\ \frac{z_\odot}{z} &= 10^{\frac{V_\odot}{5}}, \text{ and finally} \\ \Delta = \Delta_\odot\left(\frac{z_\odot}{z}\right) &= \Delta_\odot 10^{\frac{V_\odot}{5}}, \end{aligned} \tag{12}$$

where $L_\odot$ and $\Delta_\odot$ ($\simeq 30'$) represent respectively the Sun luminosity and its apparent diameter as seen from Earth. Newton then estimated $\Delta \simeq 2\,10^{-3}$" (with the current value of the visual apparent magnitude of the Sun $V_\odot = -26.7$, we derive $\Delta \sim 8\,10^{-3}$"). It should be noted that the value currently established for the star Vega with modern interferometers is $3\,10^{-3}$".

3.3 Fizeau-type interferometry

The third experimental attempt of measuring stellar diameters, based on Fizeau-type interferometry, is in fact the work of prominent scientists such as Young, Fizeau, Stephan, Michelson and Pease, the latter two having measured the first angular diameter of a star in 1920. Although other methods of interferometric measurements of stellar angular diameters appeared later (cf. the intensity interferometry of Brown and Twiss in 1957, speckle interferometry by Antoine Labeyrie in 1970, etc.), we will only describe in detail the Fizeau-type interferometry, which is still the most powerful technique used and the most promising measurement of angular diameters of stars and imagery at very high angular resolution of distant bodies by the aperture synthesis method.

Let us first remind the results obtained in the Young double hole experiment (1803, see Fig. 13).

A monochromatic plane wave coming from a distant point-like source is falling on a screen drilled with two holes (P_1 and P_2) separated along the x axis by a baseline B and positioned at a same height h (i.e. $y = h$). In accordance with the Huygens-Fresnel principle, the two holes emit spherical waves that interfere constructively whenever the difference in their propagation lengths is a multiple of λ (see Eq. (13) below), and destructively if it corresponds to an odd number of half wavelengths.

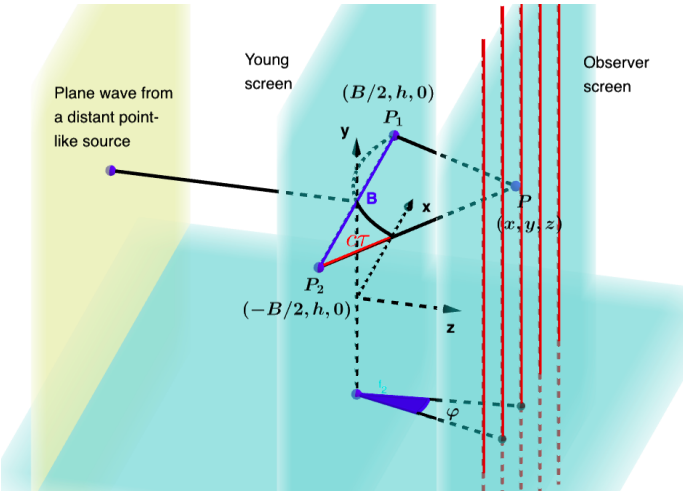

Figure 13. The double hole experiment of Young (see text).

The locus of points $P(x, y, z)$ in the observer screen with cartesian coordinates x, y, z (see Fig. 13) where there will be a constructive interference is thus given by

$$|P_1P| - |P_2P| = n\lambda = c\tau, \tag{13}$$

with $n = 0, \pm 1, \pm 2$, etc. and where $c\tau$ represents the path length difference between the two light rays arriving at the point P from P_1 and P_2; τ does therefore correspond to the time delay between the arrivals of the two light rays at P.

Let the points $P_i(x_i, y_i, 0)$ in the screen plane and $P(x, y, z)$ in the observer plane be such that $|x_i|, |y_i|, |x|, |y| << |z|$. Making use of the Pythagorean theorem, we then find that

$$|P_iP| = \sqrt{(x - x_i)^2 + (y - y_i)^2 + z^2} \tag{14}$$

which can be simplified at first order (given the above conditions) as follows:

$$|P_iP| = z\{1 + \frac{(x - x_i)^2 + (y - y_i)^2}{2z^2}\}. \tag{15}$$

Considering the two points P_1 and P_2 in the Young's screen, Eq. (13) reduces to

$$z\{1 + \frac{(x + B/2)^2 + (y - h)^2)}{2z^2}\} - z\{1 + \frac{(x - B/2)^2 + (y - h)^2}{2z^2}\} = n\lambda = c\tau \tag{16}$$

and finally [1]

$$\frac{xB}{z} = n\lambda = c\tau \tag{17}$$

or else

$$\varphi = \frac{x}{z} = n\frac{\lambda}{B} = \frac{c\tau}{B}. \tag{18}$$

The angle φ, expressed in radian, measures the separation between two successive maxima (or minima) as seen from the Young screen (see Fig. 13). Since it does not depend on the coordinate y, there results a pattern of bright and dark fringes, oriented perpendicularly with respect to the line joining the two holes, and with an inter-fringe angular separation $\varphi = \lambda/B$.

[1] To the second order, we would have found $|P_1P| - |P_2P| = \frac{Bx}{z}(1 - \frac{x^2+y^2+(B/2)^2}{2z^2})$.

In case the two holes were not infinitely small, we would intuitively expect that the observed interference pattern overlaps the combined Airy discs produced by each single hole. For $\lambda = 5500\,\text{Å}$ and $B = 1$ mm, we find that $\varphi = 113$", just at the limit of our eye visual resolution. It is also interesting to note that the height h of the pair of holes does not appear in Eqs. (17)-(18), meaning that we should observe an enhanced fringe pattern if we would replace the pair of holes by a pair of slits. Considering again the case of the two pinholes, and in accordance with Eqs. (10), (16)-(18), the resulting intensity I_T at the point P in the observer plane due to the interfering secondary waves coming from P_1 and P_2 is successively given by

$$\begin{aligned} I_T &= [A + A\exp(i2\pi\nu\tau)][A^* + A^*\exp(-i2\pi\nu\tau)], \\ &= AA^* + AA^*[\exp(-i2\pi\nu\tau) + \exp(i2\pi\nu\tau)] + AA^*, \\ &= 2I[1 + \cos(2\pi\nu\tau)], \\ &= 2I[1 + \cos(2\pi\frac{\varphi}{\lambda/B})], \text{ (a)} \\ &= 2I[1 + \cos(2\pi u\varphi)], \text{ (b)} \\ &= 2I[1 + \cos(2\pi\frac{ux}{z})], \text{ (c)} \end{aligned} \tag{19}$$

where

$$u = \frac{B}{\lambda} \tag{20}$$

is the angular space frequency, often referred to as the space frequency, corresponding to the selected baseline B and wavelength λ. In these relations, the quantity $I = AA^*$ does represent the expected intensity at point P that would be due to the contribution of the electromagnetic wave coming from just one of the two holes located in the Young screen. These relations indicate that the fringe pattern intensity in the observer screen varies as a (co-)sine function of the variable φ with an equivalent angular period λ/B (a), or the angular space frequency $u = B/\lambda$ (b). Relation (c) expresses the dependence of the fringe pattern intensity in the observer screen as a function of the variable x. We see here that for the case of a point-like source emitting monochromatic light at the wavelength λ and a Young screen with two pinholes, the resulting intensity I_T varies between 0 (total dark fringe) and $4I$ (bright fringe). In the absence of interference, the maximum intensity in the observer screen would have been that due to the waves coming from the two holes, i.e. $I_T = 2I$.

In 1868, the French optician Hyppolite Fizeau realized that in the Young's hole experiment presented above, the contrast of the interference fringes decreased as the diameter of the light source widened. Similarly, it decreased when the distance B between the two holes was extended. Was there a simple relation between the angular diameter Δ of the source and the spacing B between the two holes corresponding to the disappearance of the fringes? Before establishing such a rigorous relationship, let us try to understand this observation intuitively on the basis of simple geometrical considerations (see Fig. 14). Indeed, if instead of considering the diffraction pattern given by Young's holes for a single point-like source, we consider a composite source made of two (or more) incoherent point-like sources separated by an angle Δ, that is to say between which there is no interference between their light, it will result in the plane of the observer a superposition of two systems of Young fringes, separated by an angle Δ. If $\Delta \sim \varphi/2$, there will result a total scrambling of the fringes. The bright fringes of one source will overlap the dark fringes of the second one and their contrast will totally vanish.

If $\Delta \geq \varphi/2 = \frac{\lambda}{2B}$,

fringe disappearance!

Fringe visibility:

$v = \frac{I_{max} - I_{min}}{I_{max} + I_{min}}$.

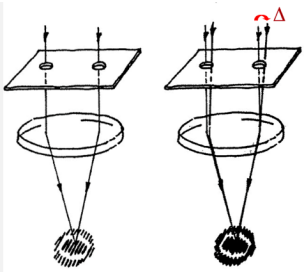

Figure 14. Fizeau experiment: for the case of a single star (left drawing) and for the case of a double star with an angular separation Δ (right drawing, see text).

From Fig. 14, it is clear that the visibility of the fringes will significantly decrease whenever the following condition takes place

$$\Delta > \frac{\varphi}{2} = \frac{\lambda}{2B}. \tag{21}$$

A quantity that objectively measures the contrast of the fringes is called the visibility. It is defined by the following expression:

$$v = \left(\frac{I_{\max} - I_{\min}}{I_{\max} + I_{\min}} \right). \tag{22}$$

Whenever a star is not resolved, we have $I_{min} = 0$, and thus the visibility $v = 1$. If the star is being resolved, $I_{max} = I_{min}$ and thus the resulting visibility $v = 0$.

Fizeau proposed in 1868 to apply this method to stellar sources. He found sufficient to place a screen drilled with two elongated apertures at the entrance of a telescope pointed towards a star and to look in the focal plane by means of a very powerful eyepiece the Airy disc crossed by the Young's fringes and to increase the distance between the two apertures until the visibility of the fringes vanishes.

This experiment is attempted in 1873 by Stephan with the 80cm telescope of the Marseille Observatory. All the bright stars visible in the sky are observed. The two openings at the entrance were actually in the form of crescents but one may demonstrate that the contrast of the fringes is independent of the shape of the two openings if they are identical. The result was disappointing: with a maximum base separation of 65cm between the openings, no attenuation of the contrast of the fringes was observed for any star. This proved that no star could be resolved using that instrument. Stephan concluded that the angular diameter of the stars is much smaller than 0.16" (see Fig. 15). From these observations, it is of course possible to set a lower limit on the effective temperature T_{eff} of all those stars (see Section 2). Figure 16 illustrates the 80 cm Marseille telescope used by Stephan and Fizeau.

3.4 Case of an extended source: a first intuitive approach towards the Zernicke-van Cittert theorem

We have seen in the previous section that a point-like source emitting monochromatic light at wavelength λ and giving rise to plane waves parallel to both the Young and observer screens gives rise to a pattern of white and dark fringes oriented perpendicularly to the direction connecting the two holes. This corresponds to the case of the source $Star1$ located at the angular position ($\zeta = 0, \eta = 0$) in Fig. 17. The first maximum takes place for $n = 0$ (or $c\tau = 0$, see Eq. (13)) and all wavelengths λ. It corresponds to the so-called white fringe located at the position $x = 0$ in the observer screen.

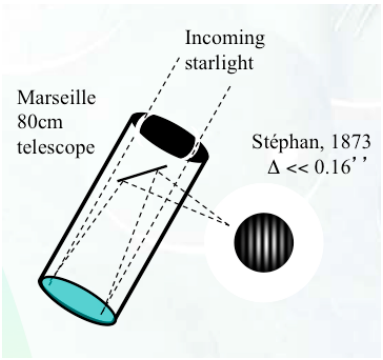

Figure 15. Diagram illustrating the way Fizeau and Stephan proceeded in order to measure the angular diameters of stars with the interferometric technique.

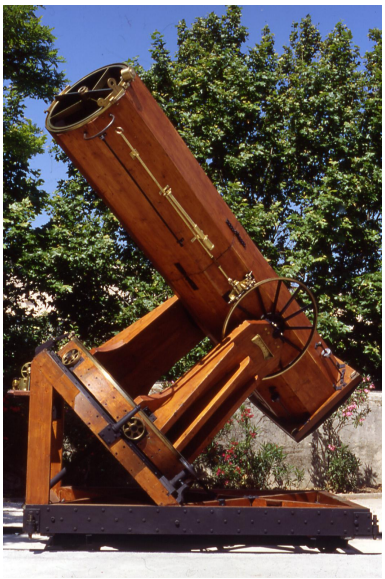

Figure 16. The 80cm Marseille telescope used by Fizeau and Stephan. © Michel Marcelin.

The expression of the fringe pattern intensity corresponding to $Star1$ may thus be rewritten as (see Eq. (19))

$$I_T(\zeta = 0, \eta = 0) = 2I(\zeta = 0, \eta = 0)[1 + \cos(2\pi \frac{ux}{z})]. \tag{23}$$

Let us just insist that its angular position is $(\zeta = 0, \eta = 0)$. If the same source was located a little above or below its original $\eta = 0$ position, we would still observe the same pattern of fringes, which would simply be translated along the y axis. This means that a same pattern of fringes is observed for sources located at positions $\zeta = 0$ and $\eta = 0$ or $\eta \neq 0$ (cf. $Star3$ in Fig. 17).

Considering the case of an extended source along the η axis, we may thus rewrite the above expression for the intensity of the fringes as

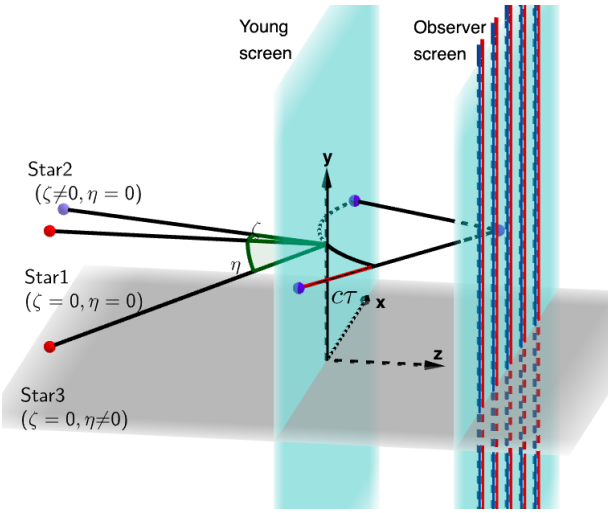

Figure 17. Illustration of the fringe patterns in the observer screen produced by point-like sources located at various angular positions (ζ, η). The fringes due to Star1 and Star3 are represented in red color, those due to Star2, in blue color.

$$
\begin{aligned}
I_T(\zeta = 0) &= \int I_T(\zeta = 0, \eta) d\eta, \\
&= 2 \int I(\zeta = 0, \eta) \, (1 + \cos{(2\pi \frac{ux}{z})}) d\eta, \\
&= 2 \int I(\zeta = 0, \eta) d\eta \, (1 + \cos{(2\pi \frac{ux}{z})}), \\
&= 2 \, I(\zeta = 0) \, (1 + \cos{(2\pi \frac{ux}{z})}),
\end{aligned} \tag{24}
$$

where we have defined

$$
I(\zeta = 0) = \int I(\zeta = 0, \eta) d\eta. \tag{25}
$$

The quantity $I(\zeta = 0)$ represents the integrated intensity of the source along the direction perpendicular to the baseline for the particular choice of the position angle $\zeta = 0$. It is thus the intensity of the slice of the source (cf. a linear source) perpendicular to the baseline at the position $\zeta = 0$. For another angular position $\zeta \neq 0$, we would similarly define

$$
I(\zeta) = \int I(\zeta, \eta) d\eta. \tag{26}
$$

If the linear source was located at an angle $\zeta \neq 0$, the distribution of the fringes in the observer plane would simply be moved laterally by the same angle ζ (cf. $Star2$ in Fig. 17). The expression representing its intensity distribution would then become

$$
\begin{aligned}
I_T(\zeta) &= 2 \, I(\zeta) \, [1 + \cos{(2\pi u (\frac{x}{z} - \zeta))}], \\
I_T(\zeta) &= \Re [2 \, I(\zeta) \, [1 + \exp(-i 2\pi u \zeta) \exp(\frac{i 2\pi u x}{z})]],
\end{aligned} \tag{27}
$$

where $\mathfrak{R}$ represents the real part of the complex quantity inserted between the brackets.

Due to the incoherent nature of the light source, all those systems of fringes for different angular positions ζ of the source slices are independent from each other and their respective intensities are just being co-added in the observer plane. Therefore, the resulting intensity distribution is given by the expression

$$\begin{aligned} I_T &= \int I_T(\zeta) d\zeta, \\ &= \mathfrak{R}[2 \int I(\zeta)(1 + \exp(-i2\pi u\zeta) \exp(\frac{i2\pi ux}{z}))d\zeta], \\ &= 2\{\int I(\zeta)d\zeta + \mathfrak{R}[\int I(\zeta) \exp(-i2\pi u\zeta)d\zeta \exp(\frac{i2\pi ux}{z})]\}, \\ &= 2\{I + \mathfrak{R}[\gamma(u) \exp(\frac{i2\pi ux}{z})]\}, \\ &= 2\{I + \mathfrak{R}[|\gamma(u)| \exp(i\beta) \exp(\frac{i2\pi ux}{z})]\}, \\ &= 2\{I + |\gamma(u)| \cos(\beta + 2\pi \frac{ux}{z})\}, \end{aligned} \tag{28}$$

where I represents the source intensity integrated over its full angular extent

$$I = \int I(\zeta)d\zeta = \iint I(\zeta, \eta)d\zeta d\eta, \tag{29}$$

$\gamma(u)$ the Fourier transform of the integrated source intensity along a direction perpendicular to the baseline

$$\gamma(u) = \int I(\zeta) \exp(-i2\pi u\zeta)d\zeta. \tag{30}$$

This result is the essence of the Zernicke-van Cittert theorem that we shall establish more rigorously in one of the next sections.

For the rest, $|\gamma(u)|$ is the module of the complex quantity $\gamma(u)$, also known as the complex degree of mutual coherence

$$\gamma(u) = |\gamma(u)| \exp(i\beta), \tag{31}$$

β being a phase angle associated with the distribution of the integrated light source intensity along a direction perpendicular to the baseline.

Making use of Eq. (22) for the expression of the visibility of the resulting fringes, we find

$$V = |\gamma(u)|, \tag{32}$$

namely that the module of the complex degree of mutual coherence is equal to the visibility V of the fringes.

The main conclusions are twofold: 1) the measurement of the complex degree of mutual coherence $\gamma(u)$ (i.e. $|\gamma(u)|$ and β) essentially provides one Fourier component at the angular space frequency u of the source intensity distribution over the sky; 2) the module of the complex degree of mutual coherence, i.e. $|\gamma(u)|$, is given by the visibility of the observed fringes whereas the phase angle β can be obtained from the precise location of the fringe pattern in the observer plane with respect to the position of the white fringe.

Simulations illustrating all the above concepts have been prepared using the Geogebra open source applications (https://www.geogebra.org). They can be viewed on the videos Fringes_Interferometry.mp4 (just varying the value of $|\gamma_{12}|$), ZvC_1.mp4 (changing the position of the source element perpendicularly and/or in parallel to the baseline), ZvC_2.mp4 (co-adding all those fringe patterns) and Young_Fringes.mp4 (a nice summary of all the previous videos) to be downloaded via the URL: https://orbi.uliege.be/handle/2268/253241.

3.5 Home experiments: visualization of the Airy disc and the Young interference fringes

We propose hereafter two simple experiments that can be carried out at home in order to visualize with our own eyes the Airy disc and the interference fringe patterns. To do this[2], take a rectangular piece of cartoon (~ 5 cm x 10 cm) and fold it in the middle (see Fig. 18). Perforate through the two sides of this piece of cartoon two well separated circular holes having an approximate diameter of 1/2 cm. Cut a thin sheet of 'kitchen' aluminium paper into two small squares (cf. 1cm x 1cm). In one of the two squares, drill with a thin metallic pin a ~ 0.5 mm (or smaller) diameter circular hole near its centre. Glue inside the folded cartoon the first aluminium piece in such a way that the very small hole is centered with respect to one of the big holes (cf. the lower one) of the cartoon.

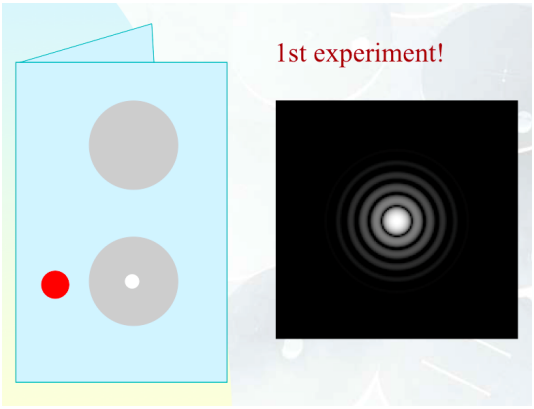

Figure 18. The one hole screen experiment: the small circular hole drilled in the aluminium paper is visible inside the lower bigger hole perforated in the cartoon screen. When looking through this hole at a distant compact light bulb, you perceive a nice Airy disc (cf. right image).

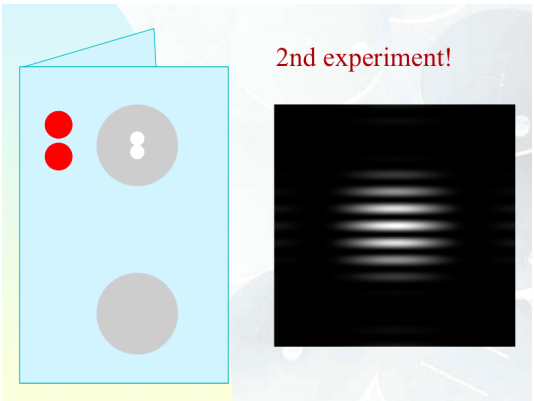

Figure 19. The two hole screen experiment: the two small circular holes drilled in the aluminium paper are visible inside the upper bigger hole perforated in the cartoon screen. When looking through these two holes at a distant compact light bulb, you perceive a nice Airy disc superimposed by a pattern of bright and dark fringes (cf. right image).

[2] You may also take photographs of the Airy disc and interference fringe patterns, see e.g. the content of the file Micro_Interferometers.pdf which can be downloaded from the URL: https://orbi.uliege.be/handle/2268/253241

Take the second square of aluminium and drill with the thin metallic pin two 0.5 mm (or smaller) circular holes near its centre separated by about 0.5-1 mm (see Fig. 19). Glue now near the second circular hole (cf. the upper one) inside the folded cartoon this second aluminium square. After, you should glue the two sides of the cartoon in such a way that you can hold it with ease in one hand. Of course you can do this on a single cartoon or on two separate ones. Place at a distance of about 10m a small light bulb (cf. the light of a cell phone) and look at it through the single hole drilled in the aluminium. You should see a nice Airy disc which angular diameter is $2.44\,\lambda/D$, with D being about 0.5 mm and λ the wavelength of the ambient light ($\sim$ 5000 Å). Now looking at the distant light source through the double hole drilled in the other square of aluminium, you should see an Airy disc superimposed by a series of white and dark fringes, oriented perpendicularly with respect to the line joining the two holes, with an angular inter-fringe separation λ/D, where $D \sim$ 0.5-1 mm. If you rotate azimuthally the screen, you will observe that the fringes also rotate since they constantly remain perpendicular to the line joining the two small holes of the milli-interferometer. While getting closer to the small light bulb, you will notice that the visibility of the fringes decreases. Let *Dist* be the distance around which the latter totally vanishes. The product of *Dist* by λ/D corresponds to the linear diameter of the light bulb. Instead of changing the distance between the light bulb and the milli-interferometer, one could change the separation between the two holes and determine the separation for which the interference fringes disappear. Adopting the same approach as Stephan, Abraham Michelson used in 1890 the Lick 30cm telescope to resolve the four Galilean satellites of Jupiter. Their angular sizes were of the order of 0.8" - 1.4" while the resolving power provided by the largest baseline he used was about 0.5". An excellent agreement was found for the angular diameters of the satellites with the classical measurements made at the same time. To resolve the biggest stars, much longer baselines are needed. Michelson and Pease built a 7m metal beam carrying four 15cm flat mirrors that they installed at the top of the Mount Wilson telescope, having a diameter of 2.5m (see Fig. 20).

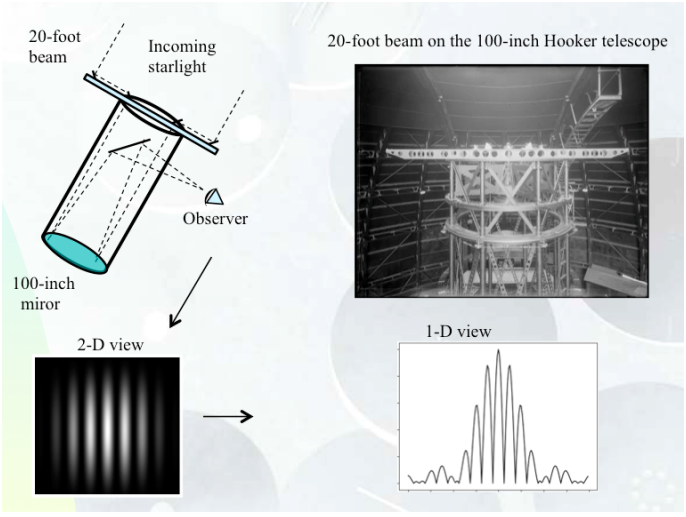

Figure 20. The stellar interferometer of Michelson and Pease set on top of the 2.5m Mount Wilson telescope. © The Observatories of the Carnegie Institution.

The two mobile exterior mirrors formed the basis of the interferometer and the two fixed interior mirrors returned the star's light into the telescope. With a maximum baseline of 7m, the smallest measurable angular diameter was 0.02". Use of this first stellar interferometer was very delicate because the visualization of the Young fringes was only possible if the two optical paths from the star passing through the two exterior mirrors and reaching the

observer eyes were equal to an accuracy of about 2 microns (see discussion below). Michelson and Pease finally obtained the first measurement of a stellar diameter during the winter of 1920, that of Betelgeuse (α Orionis), a red supergiant. They found an angular diameter of 0.047", that is a linear diameter 400 times larger than that of the Sun, given the distance of Betelgeuse (650 light years). Five more bright stars were also resolved. Anderson used the same observing technique with the 2.5m telescope at Mount Wilson to resolve very tight spectroscopic binaries (cf. Capella). Michelson and Pease did not stop there: they undertook the construction of a 15m optical beam based on the same principle, and began to use it in 1929. Unfortunately, the mechanical vibrations and deformations were such that this instrument was too delicate. It was abandoned in 1930, without having reached its limiting angular resolution of 0.01". It was not until 1956 that optical stellar interferometry was reborn and again, according to a principle different from that of Fizeau. Fizeau-type interferometry had indeed acquired a reputation of great operational difficulty. The intensity interferometry by the two radar manufacturers Hanbury Brown and Twiss (Australia) was then set up, based on an entirely new approach: the measurement of the space correlation of the stellar intensity fluctuations. Their interferometer made it possible to measure the diameter of 32 blue stars with a very high precision (< 0.0005") and to detect a few very tight binaries. But it is in the field of radio astronomy that the development of interferometry with independent telescopes became the most spectacular in the 1950s. At optical wavelengths, we had to wait until 1975 when Prof. Antoine Labeyrie and his close collaborators succeeded in combining the light from two independent telescopes. A boost then took place in the successful development of optical/IR interferometry.

4 Light coherence

When we previously established the relationship between the angular diameter Δ of a source and the separation B between the two apertures of the interferometer for which the interference fringes disappear, we assumed that the waves falling on Young's screen were purely monochromatic. In addition, the holes through which light is being scattered should have finite dimensions. Therefore, we shall later take into account the finite dimensions of the apertures (see Section 6) but let us first consider the effects due to the finite size of the spectral range across which light is being emitted from a distant source and to do so, we shall make use of some elements of the theory of light coherence. This theory consists essentially in a statistical description of the properties of the radiation field in terms of the correlation between electromagnetic vibrations at different points in the field.

4.1 Quasi-monochromatic light

The light emitted by a real source (see Fig. 21) is of course not monochromatic. As in the case of a monochromatic wave, the intensity of such a radiation field at any point in space is defined by

$$I = \langle V(t)V(t)^* \rangle \,. \tag{33}$$

In order to determine the electric field created by such a source, emitting within a certain frequency range $\pm\Delta\nu$, we must sum up the fields due to all the individual monochromatic components such that the resulting electric field $V(z,t)$ is given by the real part of the following expression:

$$V(z,t) = \int_{\nu-\Delta\nu}^{\nu+\Delta\nu} a(\nu') \, \exp[i2\pi(\nu' t - z/\lambda')] d\nu'. \tag{34}$$

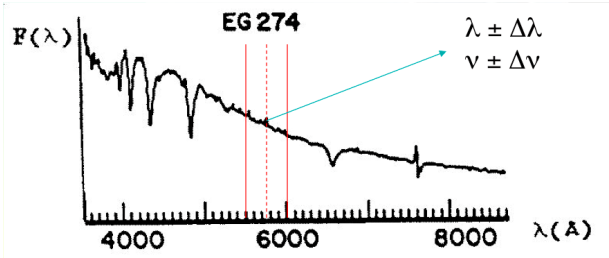

Figure 21. Stars do not emit monochromatic light. Quasi monochromatic light is assumed to be emitted at the wavelength λ (resp. the frequency ν) within the bandwidth $\pm\Delta\lambda$ (resp. $\pm\Delta\nu$).

While a monochromatic beam of radiation corresponds to an infinitely long wave train, it can easily be shown that the superposition of multiple infinitely long wave trains, with nearly similar frequencies, results in the formation of wave groups. Indeed, the expression of the electric field established in Eq. (34) can be reduced as follows. Insert in the integral of Eq. (34) the following factors: $\exp[i2\pi(\nu t - z/\lambda)]\ \exp[-i2\pi(\nu t - z/\lambda)]$. We then find that Eq. (34) may be rewritten as

$$V(z,t) = A(z,t)\ \exp[i2\pi(\nu t - z/\lambda)] \tag{35}$$

where

$$A(z,t) = \int_{\nu-\Delta\nu}^{\nu+\Delta\nu} a(\nu')\ \exp\{i2\pi[(\nu'-\nu)t - z(1/\lambda' - 1/\lambda)]\}d\nu'. \tag{36}$$

Expression (35) represents that of a monochromatic wave of frequency ν whose amplitude $A(z,t)$ varies periodically with a much lower frequency $\Delta\nu$ (cf. the sound illustration of the beat phenomenon in the video Beat_Phenomenon.mp4 which can be downloaded via the URL: https://orbi.uliege.be/handle/2268/253241).

As an exercise, it is instructive to set $a(\nu')$ constant in Eq. (36) and establish that indeed $A(z,t)$ varies as a function of time with a frequency $\Delta\nu$. This modulation therefore effectively splits the monochromatic wave trains having different but nearly similar frequencies into wave groups whose length is of the order of $\lambda^2/\Delta\lambda$, with $\Delta\lambda = -c\Delta\nu/\nu^2$ and the frequency of the order $\Delta\nu$ (see Figure 22).

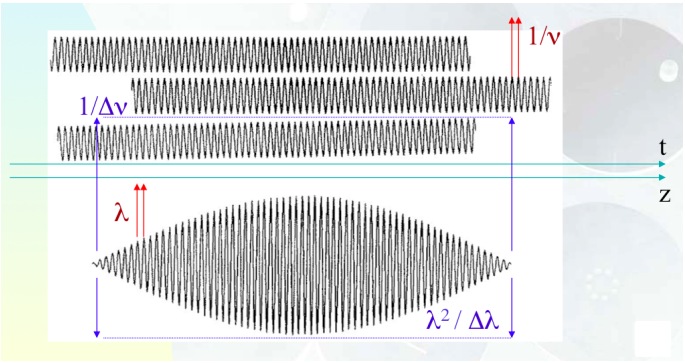

Figure 22. Superposition of long wave trains having quite similar frequencies ν' in the range $\nu \pm \Delta\nu$ (resp. wavelengths λ' in the range $\lambda \pm \Delta\lambda$) results in the propagation of long wave trains with the frequency ν (resp. wavelength λ) but which amplitude $A(z,t)$ is varying with a lower frequency $\Delta\nu$ (resp. longer wavelength $\lambda^2/\Delta\lambda$).

4.2 Visibility of the interference fringes

What becomes the visibility of the interference fringes in the Young's hole experiment for the case of a quasi-monochromatic source having a finite dimension?

Figure 23. Assuming an extended source S which quasi monochromatic light passes through the two holes P_1 and P_2, I_q represents the intensity distribution at the point q which accounts for the formation of the interference fringes.

We can re-write the expression of the intensity I_q at point q as indicated below (see Eqs. (37)-(40)). It is assumed that the holes placed at the points P_1, P_2 in the Young plane have the same aperture size (i.e. $V_1(t) = V_2(t)$) and that the propagation times of the light between P_1 (resp. P_2) and q are t_{1q} (resp. t_{2q}, see Fig. 23) :

$$I_q = \left\langle V_q^*(t) V_q(t) \right\rangle, \tag{37}$$

$$V_q(t) = V_1(t - t_{1q}) + V_2(t - t_{2q}) \tag{38}$$

and after a mere change of the time origin

$$V_q(t) = V_1(t) + V_2(t - \tau) \tag{39}$$

where we have defined

$$\tau = t_{2q} - t_{1q}. \tag{40}$$

It follows that Eq. (37) can be easily transformed into (41) where (42) represents the complex degree of mutual coherence, and the intensity $I = < V_1 V_1^* > = < V_2 V_2^* >$. Equation (41) is used to find what is the intensity distribution of the interference fringes in the observation plane. The complex degree of mutual coherence $\gamma_{12}(\tau)$ (see Eq. (42)) is a fundamental quantity whose significance will be highlighted when calculating the visibility of the interference fringes. By means of (35), this function $\gamma_{12}(\tau)$ can still be expressed as (43), and if $\tau << 1/\Delta\nu$ (i.e. the difference between the arrival times of the two light rays is less than the beat period $1/\Delta\nu$ of the quasi-monochromatic radiation), we can give it the form (44):

$$I_q = I + I + 2I\, Re[\gamma_{12}(\tau)], \tag{41}$$

$$\gamma_{12}(\tau) = \left\langle V_1^*(t) V_2(t - \tau) \right\rangle / I, \tag{42}$$

$$\gamma_{12}(\tau) = \left\langle A_1^*(z,t) A_2(z, t - \tau) \right\rangle \exp(-i2\pi\nu\tau)/I, \tag{43}$$

and if the condition of *temporal coherence* is fulfilled, i.e. $\tau << 1/\Delta\nu$, we may write

$$\gamma_{12}(\tau) = |\gamma_{12}(\tau = 0)| \exp(i\beta_{12} - i2\pi\nu\tau). \tag{44}$$

Equation (41) can then be rewritten as (45) and in this case the visibility v of the interference fringes is $|\gamma_{12}(\tau = 0)|$ (see Eq. (46)), I_{max} and I_{min} representing the brightest and weakest fringe intensities.

$$I_q = I + I + 2I\, |\gamma_{12}(\tau = 0)|\, cos(\beta_{12} - 2\pi\nu\tau) \tag{45}$$

and

$$v = \left(\frac{I_{\max} - I_{\min}}{I_{\max} + I_{\min}} \right) = |\gamma_{12}(\tau = 0)|. \tag{46}$$

We will see in the next section (but see also Section 3.4, Eq. (30)) that the module of $\gamma_{12}(\tau = 0)$ is directly related to the structure of the source that we are observing.

We propose hereafter to the reader to answer the two following questions. What is the value of $|\gamma_{12}(\tau = 0)|$ in the Young's holes experiment for the case of a monochromatic wave, two point-like holes and an infinitely small point-like source? And what can we say about the source when $|\gamma_{12}(\tau = 0)| = 0$?

Let us now evaluate what $\gamma_{12}(\tau = 0)$ is for the case we are interested in, namely an extended source emitting quasi-monochromatic light. This leads us directly to study the notion of the spatial coherence of light.

4.3 Zernicke-van Cittert theorem

Let us thus evaluate Eq. (42) for the case $\tau = 0$. We find

$$\gamma_{12}(\tau = 0) = \langle V_1^*(t) V_2(t) \rangle / I. \tag{47}$$

If $V_{i1}(t)$ and $V_{i2}(t)$ represent the electric fields at P_1 and P_2 due to a small surface element dS_i on the source S (see Fig. 24), we find that the fields $V_1(t)$ and $V_2(t)$ can be expressed as

$$\begin{aligned} V_1(t) &= \sum_{i=1}^{N} V_{i1}(t), \\ V_2(t) &= \sum_{i=1}^{N} V_{i2}(t). \end{aligned} \tag{48}$$

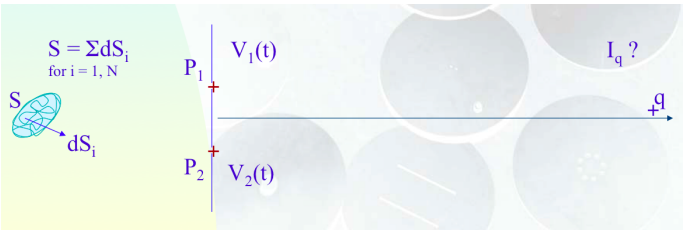

Figure 24. The extended source S is assumed to be composed of a large number of infinitesimal surface elements dS_i.

It is assumed that the distinct points i of the source are separated by small distances compared to the wavelength λ of the light they emit in a mutually incoherent manner. Obtaining the expression (49) for $\gamma_{12}(0)$ is then immediate

$$\gamma_{12}(0) = \left[\sum_{i=1}^{N} \left\langle V_{i1}^* V_{i2} \right\rangle + \sum_{i \neq j}^{N} \langle V_{i1}^* V_{j2} \rangle \right] / I. \tag{49}$$

For an incoherent light source, the second summation appearing in (49) is obviously equal to zero. As a reminder, the contributions $V_{ij}(t)$ can be expressed as

$$V_{i1}(t) = \frac{a_i(t - r_{i1}/c)}{r_{i1}} \exp[i2\pi\nu(t - r_{i1}/c)],$$
$$V_{i2}(t) = \frac{a_i(t - r_{i2}/c)}{r_{i2}} \exp[i2\pi\nu(t - r_{i2}/c)] \tag{50}$$

where r_{i1} and r_{i2} respectively represent the distances between the element i of the source and the points P_1 and P_2. The products $V^*_{i1}(t)V_{i2}(t)$ simplify themselves as

$$V^*_{i1}(t)V_{i2}(t) = \frac{|a_i(t - r_{i1}/c)|^2}{r_{i1}r_{i2}} \exp[-i2\pi\nu(r_{i2} - r_{i1})/c)], \tag{51}$$

as long as the following condition (equivalent to the *temporal coherence* condition) is verified

$$|r_{i1} - r_{i2}| \leq c/\Delta\nu = \lambda^2/\Delta\lambda = \ell. \tag{52}$$

We thus see how to naturally introduce the coherence length ℓ which characterizes the precision with which we must obtain the equality between the optical paths in order to be able to observe interference fringes (typically 2.5 microns in the visible for $\Delta\lambda = 1000$ Å).

To obtain the mutual intensity due to the whole source, it suffices to insert in the expression (49), the relation (51) using (53). The result is Eq. (54), also known as the Zernicke-van Cittert Theorem

$$I(s)ds = |a_i(t - r/c)|^2, \tag{53}$$

$$\gamma_{12}(0) = \int_S \frac{I(s)}{r_1 r_2} \exp[-i2\pi(r_2 - r_1)/\lambda)]ds/I. \tag{54}$$

When the distance between the source and the screen is very large, the expression of this theorem can be simplified as follows. Let us adopt the orthonormal coordinate system (x, y, z) shown in Fig. 25 such that the coordinates of the two elements P_1 and P_2 of the interferometer are respectively $(X, Y, 0)$ and $(0, 0, 0)$ and those of an infinitesimal element dS_i of the source (X', Y', Z'). It is then easy to find, by means of a relation analogous to (15), that

$$|r_2 - r_1| = |P_2P_i - P_1P_i| = |-\frac{(X^2 + Y^2)}{2Z'} + (X\zeta + Y\eta)| \tag{55}$$

where

$$\zeta = \frac{X'}{Z'}, \eta = \frac{Y'}{Z'} \tag{56}$$

represent the angular coordinates of the source measured from the interferometer. Using the two last relations, one can easily transform the expression (54) into (57). The X, Y coordinates in the first member of $\gamma_{12}(0, X/\lambda, Y/\lambda)$ represent the position of one element of the interferometer relative to the other. One often defines $u = X/\lambda$ and $v = Y/\lambda$ which are quantities having the dimensions of the inverse of an angle, thus of angular space frequencies.

Apart from a multiplicative factor, we thus find that the visibility of the fringes (the function $|\gamma_{12}(\tau = 0)|$) is simply the modulus of the Fourier transform of the normalized surface brightness I' of the source (Eq. (58)).

$$\gamma_{12}(0, X/\lambda, Y/\lambda) = \exp(-i\phi_{X,Y}) \int\int I'(\zeta, \eta) \exp[-i2\pi(X\zeta + Y\eta)/\lambda]d\zeta d\eta \tag{57}$$

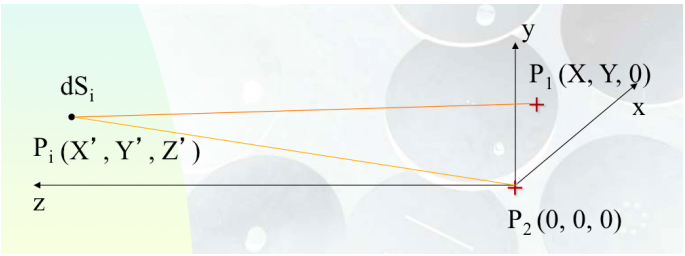

Figure 25. Positions of the two elements P_1 and P_2 of the interferometer and of the infinitesimal element P_i of the source assuming that the distance $Z' >> |X'|, |Y'|, |X|$ or $|Y|$.

with

$$I'(\zeta,\eta) = \frac{I(\zeta,\eta)}{\int\int_S I(\zeta',\eta')d\zeta' d\eta'}, \tag{58}$$

and

$$\phi_{X,Y} = \frac{2\pi}{\lambda}\frac{(X^2+Y^2)}{2Z'}. \tag{59}$$

In terms of the angular space frequencies $u = X/\lambda$, $v = Y/\lambda$, Eq. (57) becomes

$$\gamma_{12}(0,u,v) = \exp(-i\phi_{u,v}) \int\int_S I'(\zeta,\eta)\, \exp[-i2\pi(u\zeta + v\eta)]d\zeta d\eta, \tag{60}$$

with

$$\phi_{u,v} = 2\pi\lambda\frac{(u^2+v^2)}{2Z'}. \tag{61}$$

Assuming that we succeed in correcting the observed complex degree of mutual coherence $\gamma_{12}(0,u,v)$ for instrumental and/or atmospheric disturbances accounting for the $\exp(-i\phi_{u,v})$ perturbing factor (cf. Section 7.2.4), it becomes then possible, by a simple inverse Fourier transform, to recover the (normalized) surface brightness of the source with an angular resolution equivalent to that of a telescope whose effective diameter would be equal to the baseline of the interferometer consisting of two independent telescopes

$$I'(\zeta,\eta) = \int\int \gamma_{12}(0,u,v)\, \exp[i2\pi(\zeta u + \eta v)]dudv. \tag{62}$$

Equations (60) and (62) thus clearly highlight the power of the complex degree of mutual coherence since they make it possible to link the visibility and the normalized intensity distribution of the source by means of the Fourier transform $v = |\gamma_{12}(0)| = |FT[I']|$, and its inverse. Aperture synthesis consists in observing a maximum number of visibilities of the source, thus trying to cover as well as possible the (u,v) plane from which we shall try, sometimes with some additional assumptions, to determine the structure of the source from the inverse Fourier transform (62) in which the integrant is not the visibility (i.e. the module of the complex degree of mutual coherence) but the complex degree of mutual coherence itself. It is now good to remind some specific properties of the Fourier transform.

4.4 The Fourier transform: an intuitive approach, some remarkable properties and applications

4.4.1 Intuitive approach of the Fourier transform

The expression $e^{i\varphi}$ represents the complex exponential function of the real variable φ, expressed in radian:

$$e^{i\varphi} = \cos(\varphi) + i\sin(\varphi). \tag{63}$$

Its representation in the complex 2-D plane corresponds to a point P located on a circle which radius is unity, making an angle φ with respect to the real axis of reference (see Fig. 26). In this case, the variable φ does also represent the length of the subtended portion of the circular arc illustrated in red color.

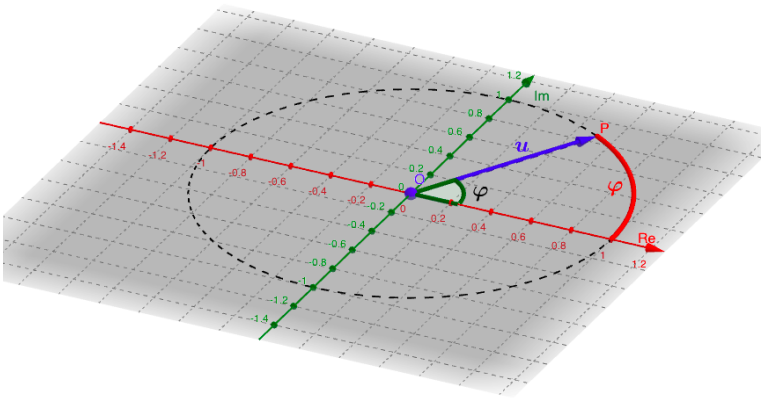

Figure 26. Illustration in the complex 2-D plane of the point P, or unit vector **u** (in blue color), corresponding to the representation of the function $e^{i\varphi}$. *Re* and *Im* represent the real and imaginary axes in that plane.

Similarly, the unit vector **u** provides another representation of the function $e^{i\varphi}$. This vector is sometimes referred in the literature as to the Fresnel vector.

In order to represent the position of the unit vector $\mathbf{u} = \mathbf{OP}$ as a function of the time t while the point P is continuously revolving around the point O with a periodicity T, it is convenient to make use of the function

$$e^{i2\pi(t/T)} = e^{i2\pi\nu t}, \tag{64}$$

with the frequency $\nu = 1/T$.

Preferring to adopt the positive sense of rotation around the point O in the clockwise direction, we shall rather represent the rotation of the point P by means of the expression

$$e^{-i2\pi\nu t}. \tag{65}$$

Let us now consider a real function $f(t)$ of the time variable t and the expression $f(t_i)e^{-i2\pi\nu t_i}dt_i$ at the time t_i during the time interval dt_i. It is then easy to assimilate this triple factor product to a vector having the same orientation as the unit vector **u** and which amplitude is $f(t_i)dt_i$.

Assuming that the function $f(t)$ is defined in the interval $[-\infty, \infty]$, we could then imagine performing the summation

$$\sum_{t_i=-\infty}^{+\infty} f(t_i)e^{-i2\pi\nu t_i}dt_i, \tag{66}$$

corresponding to a vector which is the summation of all the previously defined individual vectors and being indicative of a kind of vectorial gravity center having the following meaning. If the function $f(t)$ contains a feature appearing at a particular frequency ν_0, all the individual vectors corresponding to the summation elements $f(t_i)e^{-i2\pi\nu_0 t_i}dt_i$ will be oriented along a same direction and their summation will result in a vector which amplitude is very significant. If the function $f(t)$ does not contain features appearing as a function of time at the frequency ν_0, the corresponding individual vectors will be randomly oriented, also with random amplitudes, and the result of co-adding all of these will be a vector which amplitude is negligible. If the function $f(t)$ contains features appearing at various frequencies ν_j, there will then result several vectors which amplitudes and orientations are significant. It is then also easy to conceive that the orientations of the resulting vectors in the complex plane will be indicative of possible phase shifts of the function f(t) with respect to the corresponding functions $e^{-i2\pi\nu_j t}$.

Considering the time interval $dt_i \to 0$, we may replace the summation sign in Eq. (66) by an integral sign and find out that the result of integrating all the individual elementary vectors $f(t_i)e^{-i2\pi\nu t_i}dt_i$ results in

$$FT[f(t)](\nu) = \int_{-\infty}^{+\infty} f(t)e^{-i2\pi\nu t}dt, \tag{67}$$

which is the expression of the 1-D Fourier Transform of the function $f(t)$.

Let us illustrate this concept of vectorial gravity center by means of several examples.

For the case of the window -or door- function, i.e. $\Pi(t) = 1$ if $|t| \leq 0.5$ and 0 otherwise, and considering 10 values of t_i regularly spaced in the time interval $[-0.5, 0.5]$ we obtain by means of Eq. (66)

$$\sum_{t_i=-\infty}^{+\infty} f(t_i)e^{-i2\pi\nu t_i}dt_i = \frac{1}{10}[e^{i2\pi\nu 0.45} + e^{i2\pi\nu 0.35} + e^{i2\pi\nu 0.25} + e^{i2\pi\nu 0.15} +$$
$$e^{i2\pi\nu 0.05} + e^{-i2\pi\nu 0.05} + e^{-i2\pi\nu 0.15} + e^{-i2\pi\nu 0.25} + e^{-i2\pi\nu 0.35} + e^{-i2\pi\nu 0.45}]. \tag{68}$$

We have illustrated in Fig. 27, the ten individual vectors corresponding to the expression $f(t_i)e^{-i2\pi\nu t_i}dt_i$ assuming that $\nu = 1$. Since for the case $\nu = 1$ the 10 individual vectors are distributed symmetrically in the complex plane, their co-addition results in a vector which amplitude is equal to zero.

In Figs. 28 & 29, we have illustrated the situations for the cases $\nu = 0.2$ and $\nu = 0$. As we see, because the frequency ν decreases, the 10 individual vectors cover a smaller range in orientation and their co-addition, represented in accordance with Eq. (68) by the red vector, gets closer and closer to 1 in total amplitude. The case $\nu = 1.5$ is shown in Fig. 30. We see here that the 10 individual vectors cover a field of view larger than 2π and that the resulting combined vector is still aligned along the real axis, but in the opposite direction. Its total amplitude is real but negative. In all the previous cases we have seen that because of the symmetry of the function $\Pi(t)$, its Fourier transform is always real, sometimes positive but also sometimes negative.

Later in the course, we shall very precisely establish that the analytical expression of the Fourier transform of $\Pi(t)$ is

$$FT[\Pi(t)](\nu) = sinc(\nu) = \frac{\sin(\pi\nu)}{\pi\nu}. \tag{69}$$

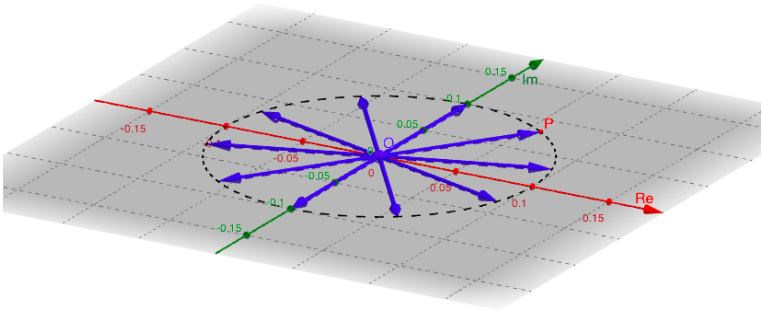

Figure 27. Illustration in the complex plane of the 10 individual vectors corresponding to the expression $\Pi(t_i)e^{-i2\pi\nu t_i}dt_i$ for the case $\nu = 1$. The co-addition of these individual vectors results in the zero null vector.

From this expression, we straightforwardly find that $FT[\Pi(t)](\nu) = 0, 0.94, 1$ and -0.21, respectively for the cases $\nu = 1, 0.2, 0$ and 1.5, in perfect agreement with our previous simulations.

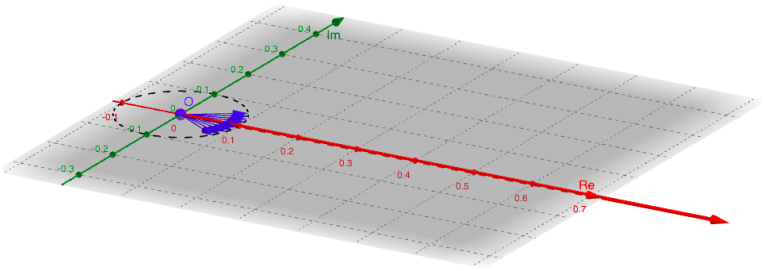

Figure 28. Illustration in the complex plane of the 10 individual vectors corresponding to the expression $\Pi(t_i)e^{-i2\pi\nu t_i}dt_i$ for the case $\nu = 0.2$. Co-addition of these individual vectors results in the red vector which amplitude is equal to 0.94.

Fig. 31 represents the Fourier transform $FT[\Pi(t)](\nu)$ of the window function $\Pi(t)$ as a function of the frequency $\nu \in [-3, 3]$. Because of the symmetry of the function $\Pi(t)$, its Fourier transform is real.

The case of an asymmetric function can be simply treated as follows. Let us still consider the window function $\Pi(t)$ but slightly translated with respect to its central position. We thus adopt the function $\Pi(t-\tau)$ where τ represents a time shift. In this case, the finite representation of the Fourier transform of $\Pi(t-\tau)$ becomes

$$\sum_{t_i=-\infty}^{+\infty} \Pi(t_i-\tau)e^{-i2\pi\nu t_i}dt_i = \frac{1}{10}[e^{-i2\pi\nu(-0.45-\tau)} + e^{-i2\pi\nu(-0.35-\tau)} + e^{-i2\pi\nu(-0.25-\tau)} + e^{-i2\pi\nu(-0.15-\tau)} + e^{-i2\pi\nu(-0.05-\tau)} + e^{-i2\pi\nu(0.05-\tau)} + e^{-i2\pi\nu(0.15-\tau)} + e^{-i2\pi\nu(0.25-\tau)} + e^{-i2\pi\nu(0.35-\tau)} + e^{-i2\pi\nu(0.45-\tau)}]. \quad (70)$$

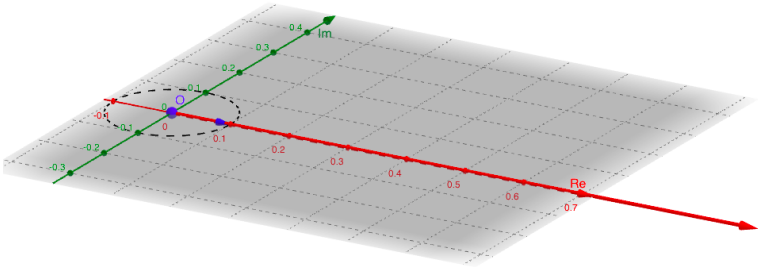

Figure 29. Illustration in the complex plane of the 10 individual vectors corresponding to the expression $\Pi(t_i)e^{-i2\pi\nu t_i}dt_i$ for the case $\nu = 0$. Co-addition of these individual vectors results in the red vector which amplitude is equal to 1.

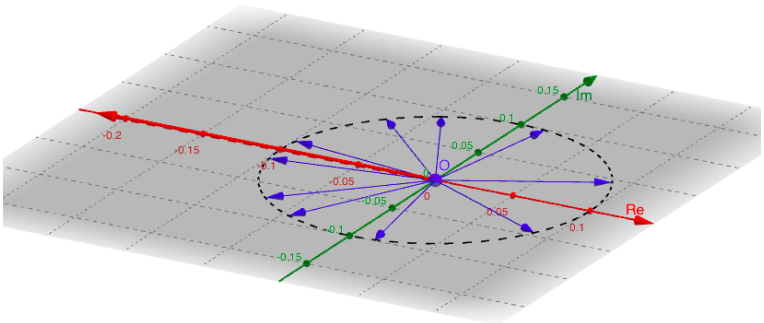

Figure 30. Illustration in the complex plane of the 10 individual vectors corresponding to the expression $\Pi(t_i)e^{-i2\pi\nu t_i}dt_i$ for the case $\nu = 1.5$. Co-addition of these individual vectors results in the red vector which amplitude is equal to -0.21, i.e. oriented along the negative side of the real axis.

In Fig. 32, we have illustrated the new situation for the case $\nu = 0.2$ and $\tau = 0.2$. As we see, because of the asymmetry of the function $\Pi(t - \tau)$ caused by the time shift τ, the 10 individual vectors are no longer symmetrically distributed around the real axis. Their summation results into the red vector which contains a real and imaginary component. The Fourier transform $FT[\Pi(t - \tau)](\nu)$ is now a complex function. Its dependence as a function of the frequency ν is illustrated in Fig. 33. Because of the asymmetry of the function $\Pi(t - \tau)$ when $\tau \neq 0$, its Fourier transform is a complex function.

4.4.2 Remarkable properties of the Fourier transform

Let us remind that the Fourier transform of the function $f(x)$, denoted $FT[f(x)](s)$, where $x \in \mathfrak{R}$, is the function

$$FT[f(x)](s) = \int_{-\infty}^{\infty} f(x)\ \exp(-2i\pi sx)dx \tag{71}$$

where $s \in \mathfrak{R}$. The functions f and $FT[f]$ form a Fourier pair. The function $FT[f]$ exists if the function $f(x)$ is bounded, summable and has a finite number of extrema and discontinuities. This does not necessarily imply that the inverse Fourier transform, denoted $FT^{-1}[FT[f]]$ transform, is f. For the Fourier transformation to be reciprocal,

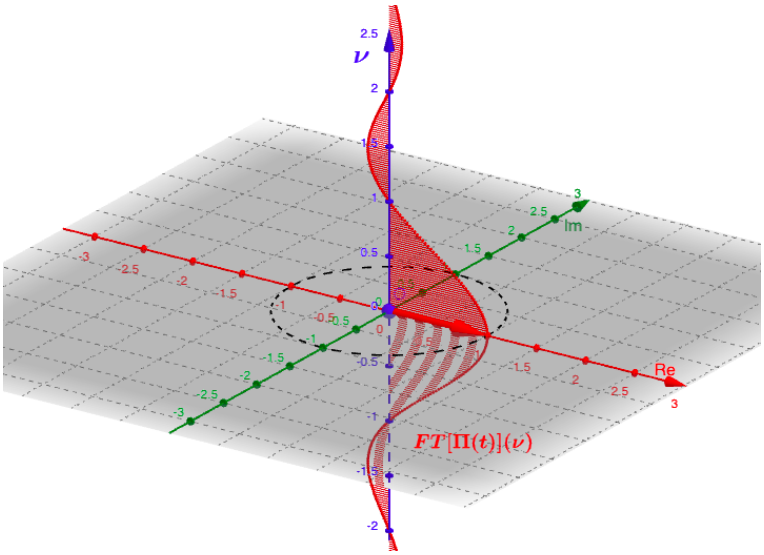

Figure 31. Illustration in the complex plane of the red vector corresponding to $\sum_{t_i=-\infty}^{+\infty} \Pi(t_i) e^{-i2\pi\nu t_i} dt_i$ and the same quantity shown by means of the red dots along the real axis as a function of the frequency $\nu \in [-3, 3]$.

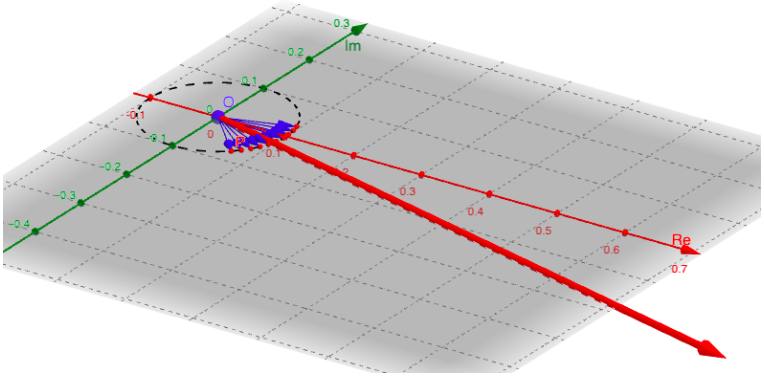

Figure 32. Illustration in the complex plane of the 10 individual vectors corresponding to the expression $\Pi(t_i - \tau) e^{-i2\pi\nu t_i} dt_i$ for the case $\nu = 0.2$ and $\tau = 0.2$. Co-addition of these individual vectors results into the red vector. The latter now contains both a real and an imaginary component.

$$f(x) = \int_{-\infty}^{\infty} FT[f](s) \exp(2i\pi xs) ds, \tag{72}$$

it suffices f to be of summable square, i.e. that the following integral exists

$$\int_{-\infty}^{\infty} |f(x)|^2 dx. \tag{73}$$

The definition of FT can be extended to the distributions. The FT of a distribution is not necessarily of summable square. Let us also note that the functions f and $FT[f]$ can be real

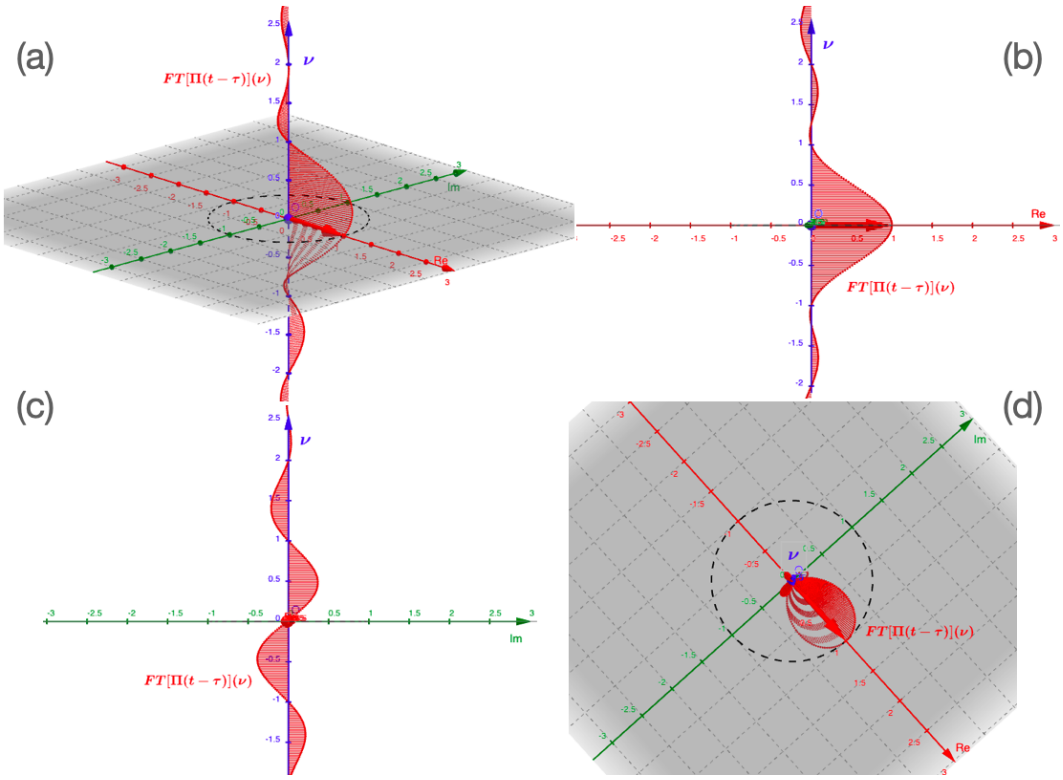

Figure 33. Illustration in the complex plane of the red vector corresponding to $\sum_{t_i=-\infty}^{+\infty} \Pi(t_i - \tau) e^{-i2\pi\nu t_i} dt_i$ for the case $\tau = 0.2$ and the same quantity shown by means of the red dots along both the real and imaginary axes as a function of the frequency $\nu \in [-3, 3]$. (a) and (d) refer to side and top views. We see that the Fourier transform $FT[\Pi(t - \tau)](\nu)$ is a complex function, revealing a helicoidal structure around the ν axis. (b) and (c) refer to views along the real and imaginary axes, respectively. We see that the real part of the Fourier transform is even whereas its imaginary part is odd.

or complex. However, in the reminder we shall only encounter the case of functions f being real.

We can generalize the FT to several dimensions, by defining $f(\mathbf{r})$ on the space $\mathfrak{R}^n$. Let $\mathbf{r}, \mathbf{w} \in \mathfrak{R}^{\mathbf{n}}$, we then have

$$FT[f(\mathbf{r})](\mathbf{w}) = \int_{-\infty}^{\infty} f(\mathbf{r}) \exp(-2i\pi \mathbf{w}\mathbf{r}) d\mathbf{r}. \tag{74}$$

As a reminder, if $f(t)$ designates a function of time, $FT[f](s)$ represents its content as a function of time frequencies. Similarly, if $f(\mathbf{r})$ is defined on $\mathfrak{R}^2$, where $\mathfrak{R}^2$ represents a two-dimensional space, the function $FT[f(\mathbf{r})](\mathbf{w})$ represents the space frequency content of $f(\mathbf{r})$, where $\mathbf{w} \in \mathfrak{R}^{\mathbf{2}}$.

Among the interesting properties of the Fourier transform, let us remind:

(i) Linearity:

$$FT[af] = a\, FT[f], \tag{75}$$

with the constant $a \in \mathfrak{R}$,

$$FT[f+g] = FT[f] + FT[g]. \tag{76}$$

(ii) Symmetry and parity:

The considerations of symmetry are very useful during the study of the Fourier transform. Let $P(x)$ and $I(x)$ be the even and odd parts of $f(x)$ such that

$$f(x) = P(x) + I(x), \tag{77}$$

we find that

$$FT[f](s) = 2\int_0^\infty P(x)\cos(2\pi xs)dx - 2i\int_0^\infty I(x)\sin(2\pi xs)dx. \tag{78}$$

From this result, we deduce that if $f(x)$ is real, the real part of $FT[f](s)$ will be even and its imaginary part will be odd (cf. Fig. 33) whereas if $f(x)$ is complex, the imaginary part of $FT[f](s)$ will be even and its real part will be odd. As previously mentioned, we shall essentially consider the cases of real functions in 1-D and 2-D spaces.

(iii) Similarity:

The relationship of similarity is the following one

$$FT[f(x/a)](s) = |a|\, FT[f(x)](as) \tag{79}$$

where $a \in \mathfrak{R}$, is a constant. The dilation of a function causes a contraction of its Fourier transform. This very visual property is very useful to understand that a function whose support is very compact, has a very spread transform. In the analysis of temporal frequencies, one would state that a pulse of very short duration results in a very broad frequency spectrum, that is to say, contains frequencies all the higher as the pulse is brief. This is the classical relation of the spectrum of a wave packet, according to which the knowledge of the properties of a signal cannot be arbitrarily precise both in time and in frequency.

(iv) Translation:

The translation relation is written as

$$FT[f(x-a)](s) = \exp(-2i\pi as)\, FT[f(x)](s). \tag{80}$$

A translation of the function in its original space corresponds to a phase rotation of its Fourier transform in the transformed space.

(v) Derivative theorem:

If $f'(x)$ represents the derivative of the function $f(x)$, we derive that

$$FT[f'(x)](s) = i2\pi s\, FT[f(x)](s). \tag{81}$$

Indeed,

$$FT[f'(x)](s) = FT[\frac{df}{dx}](s) = \int_{-\infty}^{+\infty} \frac{df}{dx} \exp(-i2\pi xs)\, dx =$$
$$\int_{-\infty}^{+\infty} [\frac{d[f\exp(-i2\pi xs)]}{dx} - \frac{f d[\exp(-i2\pi xs)]}{dx}]\, dx =$$
$$\int_{-\infty}^{+\infty} \frac{d[f\exp(-i2\pi xs)]}{dx} dx - \int_{-\infty}^{+\infty} \frac{f d[\exp(-i2\pi xs)]}{dx}\, dx =$$
$$0 - (-i2\pi s) \int_{-\infty}^{+\infty} f\exp(-i2\pi xs)\, dx = i2\pi s\, FT[f(x)](s), \tag{82}$$

and thus

$$FT[f^n(x)](s) = FT[\frac{d^n f}{dx^n}](s) = (i2\pi s)^n\, FT[f(x)](s). \tag{83}$$

This theorem provides an easy way to calculate the Fourier transform of the n^{th} derivative of a function $f(x)$ if one knows the Fourier transform $FT[f(x)](s)$ of $f(x)$.

(vi) Door function:

The door function, denoted $\Pi(x)$, is defined by (see Fig. 34)

$$\Pi(x) = 1 \quad \text{if } x \in [-0.5, 0.5], \quad \text{and} \quad \Pi(x) = 0 \quad \text{otherwise.} \tag{84}$$

It is easy to find that

$$FT[\Pi(x)](s) = sinc(s) = \frac{\sin(\pi s)}{\pi s}. \tag{85}$$

Applying the similarity relation, we also find that

$$FT[\Pi(x/a)](s) = |a|\, sinc(as) = |a|\, \frac{\sin(\pi as)}{\pi as}. \tag{86}$$

The door function is also sometimes called the window function or simply window.

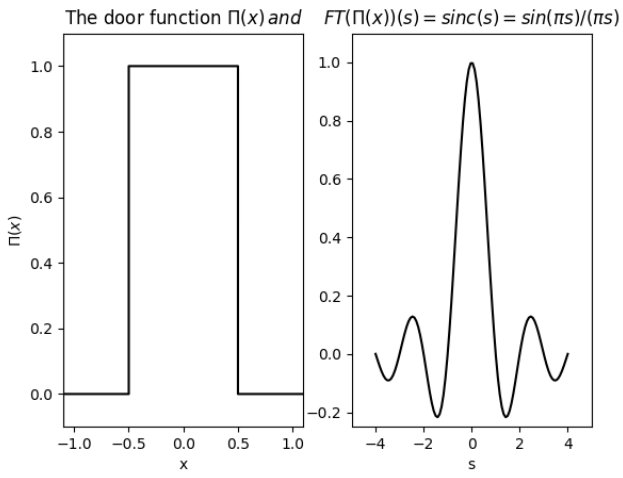

Figure 34. The door function and its Fourier transform (cardinal sine).

(vii) Distribution of Dirac:

The Dirac distribution, also called Dirac peak, is noted $\delta(x)$. It is defined by the following integral, which exists only in the sense of the distributions

$$\delta(x) = \int_{-\infty}^{\infty} \exp(2i\pi xs)ds. \tag{87}$$

Its Fourier transform is therefore 1 in the interval $]-\infty, +\infty[$ since $\delta(x)$ appears above as the inverse Fourier transform of 1.

(viii) The Dirac comb:

The Dirac comb function, noted $\text{Ш}(x)$, also known as the *Sha* function of period 1 (i.e. $\Delta x = 1$), is defined as follows

$$\text{Ш}(x) = \sum_{n=-\infty}^{+\infty} \delta(x - n) \tag{88}$$

where n represents an integer number.

We shall demonstrate hereafter that the Fourier transform of the Dirac comb function of period 1 is another Dirac comb function of period 1, i.e.

$$FT[\text{Ш}(x)](s) = \text{Ш}(s) = \sum_{m=-\infty}^{+\infty} \delta(s - m) \tag{89}$$

where m is also an integer number.

We first establish that

$$\begin{aligned} FT[\text{Ш}(x)](s) &= \int_{-\infty}^{\infty} \sum_{n=-\infty}^{+\infty} \delta(x - n) \exp(-2i\pi xs)dx, \\ &= \sum_{n=-\infty}^{+\infty} \int_{-\infty}^{\infty} \delta(x - n) \exp(-2i\pi xs)dx, \\ &= \sum_{n=-\infty}^{+\infty} FT[\delta(x - n)](s), \\ &= \sum_{n=-\infty}^{+\infty} \exp(-2i\pi ns). \end{aligned} \tag{90}$$

The Fourier transform $FT[\text{Ш}(x)](s)$ thus appears as the sum of an infinite series of terms. We immediately see that $FT[\text{Ш}(x)](s + 1) = FT[\text{Ш}(x)](s)$, meaning that it is a periodic function with a period $\Delta s = 1$. This allows us to restrict its study to just one of the space frequency intervals $\Delta s = 1$; let us choose $s \in [-0.5, 0.5]$. We then notice that whenever $s \neq 0$, $FT[\text{Ш}(x)](s)$ may be assimilated to a vector being the sum of an infinite number of basic Fresnel vectors having a module of 1 and taking all possible orientations in the complex plane, thus resulting into a vector having a module tending towards zero (see Fig. **??**). We thus expect that $FT[\text{Ш}(x)](s) = 0$ for $s \neq 0$. When $s = 0$, the series diverges and tends towards infinity.

We are now going to show that $FT[\text{Ш}(x)](s)$ corresponds to a Dirac comb with a period $\Delta s = 1$. Limiting the sum of terms in Eq. (90) to those between N and $-N$ and assuming later that $N \to \infty$, we successively obtain

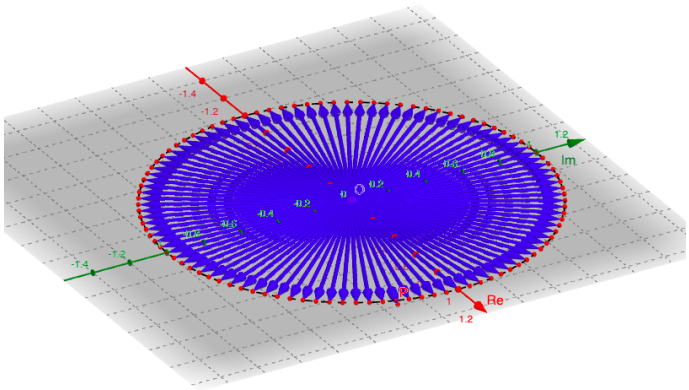

Figure 35. Representation of a large number (2N = 100) of Fresnel vectors entering Eq. (90) and which summation tends towards 0.

$$
\begin{aligned}
FT[\text{Ш}(x)]_N(s) &= \sum_{n=-N}^{N} \exp(-2i\pi ns) \\
&= \frac{\exp[-2i\pi(N+1)s]-1}{\exp(-2i\pi s)-1} + \frac{\exp[2i\pi(N+1)s]-1}{\exp(2i\pi s)-1} - 1 \\
&= \exp(-i\pi Ns)\frac{\exp[-i\pi(N+1)s]-\exp[i\pi(N+1)s]}{\exp(-i\pi s)-\exp(i\pi s)} + \exp(i\pi Ns)\frac{\exp[i\pi(N+1)s]-\exp[-i\pi(N+1)s]}{\exp(i\pi s)-\exp(-i\pi s)} - 1 \\
&= [\exp(-i\pi Ns)+\exp(i\pi Ns)]\frac{\exp[-i\pi(N+1)s]-\exp[i\pi(N+1)s]}{\exp(-i\pi s)-\exp(i\pi s)} - 1 \\
&= 2\cos(\pi Ns)\frac{\sin[\pi(N+1)s]}{\sin(\pi s)} - 1.
\end{aligned}
\tag{91}
$$

Assuming that $N \to \infty$, we may set $N+1 \simeq N$ in the previous expression and since $\sin(2x) = 2\sin(x)\cos(x)$, we find for $s \to 0$ that $\sin(\pi s) \simeq \pi s$ and thus

$$
\begin{aligned}
FT[\text{Ш}(x)]_N(s) &\simeq \frac{\sin(2\pi Ns)}{\sin(\pi s)} - 1, \text{ (a)} \\
&\simeq 2N\frac{\sin[2\pi Ns]}{2\pi Ns}, \text{ (b)} \\
&\simeq 2N \to \infty, \text{ (c)}
\end{aligned}
\tag{92}
$$

since $sinc(x) = \sin(x)/x \to 1$ when $x \to 0$. It is then also easy to show that the integration of Eq. (92(b)) over the frequency $s \in [-0.5, 0.5]$ yields $\int_{-1/2}^{1/2} FT[\text{Ш}(x)]_N(s)ds = 1$. Given this and the facts that the central peak of $FT[\text{Ш}(x)]_N(s)$ has a width equal to $1/N \to 0$ and an intensity $FT[\text{Ш}(x)]_N(s=0) \to \infty$ as $N \to \infty$, it does exactly behave like a Dirac function in the space frequency interval $s \in [-0.5, 0.5]$. Since it is periodic with a period $\Delta s = 1$, we conclude that $FT[\text{Ш}(x)](s) = \text{Ш}(s)$.

Making use of the similarity relationship Eq. (79), we also derive the useful relation

$$
FT[\text{Ш}(x/P)](s) = P\,\text{Ш}(Ps). \tag{93}
$$

4.4.3 Applications of the Fourier transform

We propose hereafter several astrophysical applications that make use of the previous remarkable properties of the Fourier transform.

(i) Equally bright double star

Let us first consider the case of a double star which two point-like components are equally bright and separated by an angle $2\zeta_0$. Making use of Eqs. (46), (58) and (60), one may easily establish using the properties (80) and (87) that the normalized intensity $I'(\zeta)$ takes the simple form

$$I'(\zeta) = \frac{\delta(\zeta - \zeta_0) + \delta(\zeta + \zeta_0)}{2} \tag{94}$$

and that the visibility v measured with an interferometer composed of 2 telescopes separated by the baseline X is given by the expression

$$v = |\gamma_{12}(0)| = |cos(2\pi\zeta_0 u)| \tag{95}$$

where $u = X/\lambda$.

(ii) 1-D Gaussian star

A second nice application consists in deriving the visibility of the interference fringes measured with the same interferometer of a $1-D$ Gaussian star which intensity $I(\zeta)$ distribution is given by the following expression[3]

$$I(\zeta) = \exp(\frac{-4\ln(2)\zeta^2}{\mathrm{FWHM}^2}) \tag{96}$$

where $FWHM$ represents the angular full width at half maximum of the $1-D$ Gaussian star. The expression of the corresponding visibility is then easily found to be

$$v = |\gamma_{12}(0,u)| = \exp\left(\frac{-\pi^2 u^2\ \mathrm{FWHM}^2}{4\ln(2)}\right), \tag{97}$$

and as already outlined before we notice that narrower is the angular size of the star, broader is its visibility content in angular space frequencies.

(iii) Uniformly bright square star

In the third proposed application, we ask to establish the expression of the visibility of a $2-D$ uniformly bright square star which each angular side is ζ_0, i.e. $I(\zeta) = Cte\ \Pi(\zeta/\zeta_0)\ \Pi(\eta/\zeta_0)$.

The expression to be derived is the following one

$$v = |\gamma_{12}(0,u,v)| = |\frac{sin(\pi\zeta_0 u)}{\pi\zeta_0 u}\frac{sin(\pi\zeta_0 v)}{\pi\zeta_0 v}|. \tag{98}$$

A video illustrating the expected visibility of a uniformly bright square star for various values of its angular size ζ_0 has been prepared using the Geogebra open source applications (https://www.geogebra.org). The corresponding file Visibility_Square_Star.mp4 can be downloaded via the URL: https://orbi.uliege.be/handle/2268/253241.

[3] It is good to remember or demonstrate that $\int_{-\infty}^{+\infty}\exp(-\pi x^2)dx = 1$ and also that $FT[\exp(-\pi x^2)](s) = \exp(-\pi s^2)$. To establish these relations, consider first to solve the double integral $\int_{-\infty}^{+\infty}\int_{-\infty}^{+\infty}\exp[-\pi(x^2+y^2)]dxdy$ and make a change from the cartesian coordinates (x,y) to the polar ones (r,φ).

(iv) Uniformly bright circular stellar disc

A generalization of the previous application consists in deriving the visibility of a star which is seen as a projected $2-D$ uniform circular disc which angular radius is ρ_{UD} and its angular diameter θ_{UD}.

Due to the circular symmetry of the problem, it is convenient to make use of polar coordinates in Eq. (57) as follows:

$$\begin{aligned} u &= X/\lambda = R\cos(\psi)/\lambda \\ v &= Y/\lambda = R\sin(\psi)/\lambda, \end{aligned} \tag{99}$$

where R denotes the baseline between the two telescopes of the interferometer, and

$$\begin{aligned} \zeta &= \theta\cos(\phi) \\ \eta &= \theta\sin(\phi). \end{aligned} \tag{100}$$

Eq. (57) then transforms into

$$|\gamma_{12}(0, R/\lambda, \psi)| = |\frac{1}{\pi\rho_{UD}^2}\int_0^{\rho_{UD}} \theta \int_0^{2\pi} \exp\left[-i2\pi\theta R/\lambda(\cos(\phi)\cos(\psi) + \sin(\phi)\sin(\psi))\right] d\phi d\theta|. \tag{101}$$

Making use of the additional changes of variables

$$\begin{aligned} z &= 2\pi\theta R/\lambda \\ \Phi &= \pi/2 - \phi + \psi, \end{aligned} \tag{102}$$

Eq. (101) becomes

$$|\gamma_{12}(0, R/\lambda, \psi)| = |(\frac{\lambda}{2\pi R})^2 \frac{1}{\pi\rho_{UD}^2}\int_0^{2\pi\rho_{UD}R/\lambda} \theta \int_{-3\pi/2+\psi}^{\pi/2+\psi} \cos(z\sin(\Phi)) d\Phi d\theta|. \tag{103}$$

Reminding the definition of the zero order Bessel function $J_0(x)$

$$J_0(x) = \frac{1}{\pi}\int_0^{\pi} \cos[x\sin(\theta)] d\theta, \tag{104}$$

and the relation existing between $J_0(x)$ and the first order Bessel function $J_1(x)$, namely

$$xJ_1(x) = \int x' J_0(x') dx', \tag{105}$$

Eq. (103) successively reduces to

$$|\gamma_{12}(0, R/\lambda)| = |(\frac{\lambda}{2\pi R})^2 \frac{1}{\pi\rho_{UD}^2} 2\pi \int_0^{2\pi\rho_{UD}R/\lambda} zJ_0(z) dz| \tag{106}$$

and

$$|\gamma_{12}(0, R/\lambda)| = |2\frac{J_1(2\pi\rho_{UD}R/\lambda)}{2\pi\rho_{UD}R/\lambda}|. \tag{107}$$

We thus find that the expression (46) of the fringe visibility for the case of a star seen as a projected $2-D$ uniform circular disc with an angular dimater $\theta_{UD} = 2\rho_{UD}$ is

$$v = \left(\frac{I_{\max} - I_{\min}}{I_{\max} + I_{\min}}\right) = |\gamma_{12}(0,u)| = \left|\frac{2J_1(\pi\theta_{UD}u)}{\pi\theta_{UD}u}\right|, \tag{108}$$

where we have set $u = R/\lambda$. As a reminder, the Bessel function has the following properties

$$\begin{aligned} J_1(x = 3.8317...) &= 0 \\ \lim_{x\to 0}\frac{J_1(x)}{x} &= 1/2, \end{aligned} \tag{109}$$

which allow us to easily understand the behavior of the visibility function illustrated in Fig. 36. A simulation illustrating the formation of fringe patterns for the case of a circular stellar disc which is uniformly bright has been prepared using the Geogebra open source applications (https://www.geogebra.org). It can be viewed on the video ZvCt.mp4 to be downloaded via the URL: https://orbi.uliege.be/handle/2268/253241.

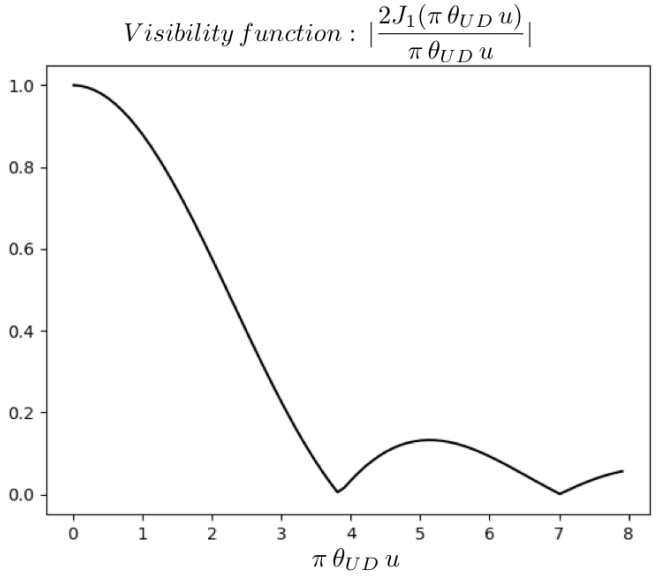

Figure 36. Visibility function expected for a star consisting of a uniformly bright circular disc with an angular diameter θ_{UD}.

One could then wonder whether it is possible to observe interferometric fringes from our nearest star, i.e. the Sun? Figure 37 illustrates such fringes in while light obtained on 9th of April 2010 using a micro interferometer consisting of 2 holes with a diameter of 11.8 μ separated by a baseline of 29.4 μ. This micro-interferometer was placed in front of the objective of an EOS 5D Canon camera. Since the picture was taken in white light, it is possible to see the effects due to color dispersion. It is then easy to get an estimate of the fringe visibility, using Eq. (108), assuming that the Sun is a uniform disc with an angular diameter of 30'.

(v) The general case of a double star

Let us derive the expressions of the module and phase of the complex degree of mutual coherence $\gamma_{12}(\tau = 0, u, v)$ for the case of a binary star consisting of two unequally bright point-like components with an unknown orientation projected on the plane of the sky.

Figure 37. Solar fringes photographed with an EOS 5D Canon camera in front of which was set a micro-interferometer consisting of two holes having a diameter of 11.8 μ separated by a baseline of 29.4 μ.

Assuming that we are measuring the angular separation between the two unresolved stars as being ζ_0, η_0 with the angular coordinates ζ, η oriented along the East-West and North-South directions, respectively, just alike the u, v space frequencies, and adopting I_1, I_2 for the intensities of the two individual unresolved stars, we easily find for $I'(\zeta, \eta)$

$$I'(\zeta,\eta) = \frac{I_1\delta(\zeta - \frac{\zeta_0}{2})\delta(\eta - \frac{\eta_0}{2}) + I_2\delta(\zeta + \frac{\zeta_0}{2})\delta(\eta + \frac{\eta_0}{2})}{I_1 + I_2}, \tag{110}$$

where δ represents the Dirac function. We immediately verify that the integration of $I'(\zeta, \eta)$ over the coordinates ζ, η is correctly normalized (i.e. = 1).

Inserting Eq. (110) into Eq. (57), and making use of the properties of variable separation, Dirac function and translation of the Fourier transform, we successively obtain:

$$\begin{aligned}
\gamma_{12}(\tau = 0, u, v) &= \frac{1}{I_1 + I_2}[I_1\, FT\{\delta(\zeta - \frac{\zeta_0}{2})\,\delta(\eta - \frac{\eta_0}{2})\}(u,v) + \\
&\qquad I_2\, FT\{\delta(\zeta + \frac{\zeta_0}{2})\,\delta(\eta + \frac{\eta_0}{2})\}(u,v)], \\
&= \frac{1}{I_1 + I_2}[I_1\, FT\{\delta(\zeta - \frac{\zeta_0}{2})\}(u)\, FT\{\delta(\eta - \frac{\eta_0}{2})\}(v) + \\
&\qquad I_2\, FT\{\delta(\zeta + \frac{\zeta_0}{2})\}(u)\, FT\{\delta(\eta + \frac{\eta_0}{2})\}(v)], \\
&= \frac{1}{I_1 + I_2}[I_1\, \exp(-i\pi(\zeta_0 u + \eta_0 v)) + I_2\, \exp(i\pi(\zeta_0 u + \eta_0 v))].
\end{aligned} \tag{111}$$

Defining the relative intensities of the two stars as being

$$\begin{aligned}
\epsilon &= \frac{I_1}{I_1 + I_2}, \\
1 - \epsilon &= \frac{I_2}{I_1 + I_2},
\end{aligned} \tag{112}$$

the expression (111) of $\gamma_{12}(\tau = 0, u, v)$ can be successively rewritten as

$$\begin{aligned}
\gamma_{12}(\tau = 0, u, v) &= \epsilon\, \exp(-i\pi(\zeta_0 u + \eta_0 v)) + (1 - \epsilon)\, \exp(i\pi(\zeta_0 u + \eta_0 v)), \\
&= \cos(\pi(\zeta_0 u + \eta_0 v)) + i(1 - 2\epsilon)(\sin(\pi(\zeta_0 u + \eta_0 v)).
\end{aligned} \tag{113}$$

Still better! Adopting for the expression of $\gamma_{12}(\tau = 0, u, v)$ the following form (cf. Eq. (31))

$$\gamma_{12}(\tau = 0, u, v) = |\gamma_{12}(\tau = 0, u, v)|\exp(i\beta_{12}), \tag{114}$$

we successively find for the module of the complex degree of mutual coherence (i.e. the visibility V of the fringes)

$$V = |\gamma_{12}(\tau = 0, u, v)| = \sqrt{\cos^2(\pi(\zeta_0 u + \eta_0 v)) + (1 - 2\epsilon)^2 \sin^2(\pi(\zeta_0 u + \eta_0 v))}$$
$$= \sqrt{\epsilon^2 + (1 - \epsilon)^2 + 2\epsilon(1 - \epsilon)\cos(2\pi(\zeta_0 u + \eta_0 v))} \tag{115}$$

and for its phase β_{12}

$$\beta_{12} = \arctan\,[(1 - 2\epsilon)\tan(\pi(\zeta_0 u + \eta_0 v))], \text{ or also}$$
$$\beta_{12} = \arcsin\,[\frac{(1 - 2\epsilon)\sin(\pi(\zeta_0 u + \eta_0 v))}{|\gamma_{12}(\tau = 0, u, v)|}]. \tag{116}$$

Some astronomers prefer to represent the previous relations in terms of the flux ratio between the two stars, i.e. the quantity $I_{21} = I_2/I_1$.

Noticing that

$$\epsilon = \frac{1}{1 + I_{21}}, \tag{117}$$

we obtain

$$V = |\gamma_{12}(\tau = 0, u, v)| = \sqrt{\frac{1 + I_{21}^2 + 2I_{21}\cos(2\pi(\zeta_0 u + \eta_0 v))}{(1 + I_{21})^2}}, \text{ and}$$
$$\beta_{12} = \arctan\,[\frac{I_{21} - 1}{I_{21} + 1}\tan(\pi(\zeta_0 u + \eta_0 v))], \text{ or still}$$
$$\beta_{12} = \arcsin\,[\frac{\frac{I_{21}-1}{I_{21}+1}\sin(\pi(\zeta_0 u + \eta_0 v))}{|\gamma_{12}(\tau = 0, u, v)|}]. \tag{118}$$

Noticing that the quantity $\zeta_0 u + \eta_0 v$ is merely the scalar product between the angular vector $\mathbf{Z_0}(\zeta_0, \eta_0)$ joining the two stars and the baseline vector $\mathbf{U}(u, v)$, i.e. $\mathbf{Z_0U}$, we may replace in all the previous relations the former quantity by

$$\zeta_0 u + \eta_0 v = \mathbf{Z_0U} = \rho\frac{B}{\lambda}\cos(\theta - \omega), \tag{119}$$

where ρ $(= \sqrt{\zeta_0^2 + \eta_0^2})$ represents the module of the angular vector $\mathbf{Z_0}(\zeta_0, \eta_0)$, i.e. the angular separation between the two components of the binary star, B $(= \sqrt{u^2 + v^2})$ the module of the projected baseline, and finally θ and ω the position angles of the projected line joining the two stars and of the baseline projected on the plane of the sky, respectively (see Figures 38 & 39).

To be complete, let us mention that the dots plotted in Figs. 38 & 39 refer to the changing u, v coordinates of a projected baseline at positions $u_0 = 1.4, v_0 = 2.6$ on the horizontal plane (latitude $\varphi = 52°$) seen during the rotation of the Earth from a binary star ($\zeta_0 = 1$, $\eta_0 = 1$) with declination $\delta = 10°$. A time interval of 30 minutes separates each dot, starting 6 hours before and ending 6 hours after passing the local meridian.

Simulations illustrating the fringe patterns expected for the case of a binary star observed with different baselines have been prepared using the Geogebra open source applications

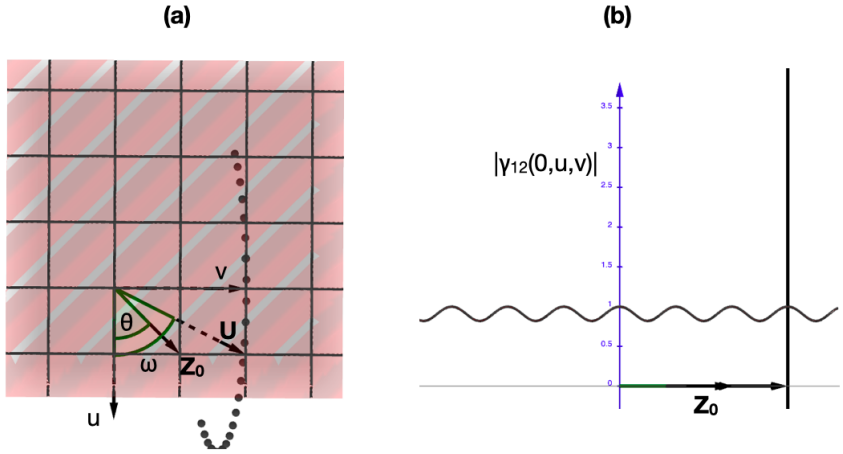

Figure 38. (a) Top view of the (u,v) plane and representation of a given vector **U** with components (u=1, v=2) and of the angular vector $\mathbf{Z_0}$ ($\zeta_0 = 1$, $\eta_0 = 1$) corresponding to the separation between the two components of a double star. The dots projected on the (u, v) plane represent the positions of a fixed baseline on Earth as seen every 30 minutes from the binary star starting 6 hours before and ending 6 hours after passing the meridian (see the text). The angles θ and ω refer to the position angles of the $\mathbf{Z_0}$ and **U** vectors as measured from the u axis. The grey lines seen at 45° refer to positions in the (u, v) plane for which the visibility of the interferometric fringes of the double star characterized by a flux ratio of 10 is maximum. (b) Expected visibilty ($V = |\gamma_{12}(0, u, v)|$) of the fringes caused by the same double star along any axis parallel to the angular vector $\mathbf{Z_0}$.

(https://www.geogebra.org). They can be viewed on the video Interf_Binary_Star.mp4 to be downloaded via the URL: https://orbi.uliege.be/handle/2268/253241.

In the remainder, we shall explain how to calculate the (u, v) coverage corresponding to a selected baseline of an interferometer located on Earth, seen from a distant celestial source during the Earth's rotation.

5 Coverage of the (u,v) plane during the Earth's rotation

Let us first define three different coordinate systems of reference S, S' and S" as follows. They are all centered on the Earth center. The first system S has its z axis pointing towards the celestial source of interest. Its y axis is perpendicular to the z axis and is contained in the meridian plane (see Figure 40). The x axis is perpendicular to the two previous ones, forming a right angle oriented system of coordinates. The second system of reference S' just differs from the previous one by a rotation around the x' (= x) axis by an angle δ which corresponds to the declination of the star. The S' system does therefore possess its y' axis oriented along the South-North direction and the x', z' axes are located in the equatorial plane of the Earth (see Figure 40). Finally, the third system of reference S" differs from the S' system by a simple rotation around its y" (= y') axis by an angle HA which represents the Hour Angle of the celestial object as measured in the S" system. The observer O is thus supposed to be located in the S" system, at the latitude φ, and an interferometric baseline may be defined in the horizontal plane as the vector **B** being a linear combination of the two unit vectors **R** and **S** oriented towards the West-East and South-North directions, respectively. We easily find that their coordinates defined in the S" system are the following ones:

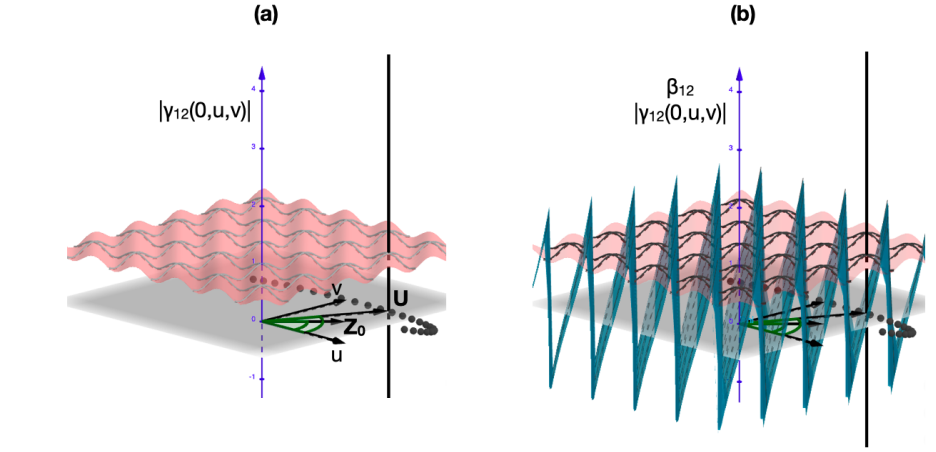

Figure 39. (a) 3-D view of the visibilty (V = $|\gamma_{12}(0,u,v)|$) of the fringes caused by the double star described in the previous figure caption. (b) Same as (a) but with in addition the superimposition of the angle β_{12} defined in Eq. (118) illustrating the fact that when an asymmetric object is observed with an interferometer, the complex degree of mutual coherence $\gamma_{12}(0,u,v)$) is a complex (and not any longer a real) quantity (cf. Eq. (114)). In that case both the observed visibility V = $|\gamma_{12}(0,u,v)|$ and the phase angle β_{12} contain information relative to the observed source.

$$\begin{aligned} \mathbf{R} &= (1,0,0), \\ \mathbf{S} &= (0,\cos(\varphi),-\sin(\varphi)), \end{aligned} \tag{120}$$

with

$$\mathbf{B} = \alpha\,\mathbf{R} + \beta\,\mathbf{S}, \tag{121}$$

α and β being two constants associated with the length and orientation of the baseline **B** in the local horizontal plane.

By means of the coordinate transformations between the S' and S", and S and S' systems, namely

$$\begin{aligned} x' &= z''\sin(HA) + x''\cos(HA), \\ y' &= y'' \\ z' &= z''\cos(HA) - x''\sin(HA), \text{ and} \\ x &= x', \\ y &= -z'\sin(\delta) + y'\cos(\delta), \end{aligned} \tag{122}$$

we then find that the $u = x/\lambda$, $v = y/\lambda$ coordinates may be expressed in terms of the x'', y'', z'' coordinates as follows

$$\begin{aligned} u &= \frac{x}{\lambda} = \frac{x'}{\lambda} = \frac{z''\sin(HA) + x''\cos(HA)}{\lambda}, \\ v &= \frac{y}{\lambda} = \frac{-z'\sin(\delta) + y'\cos(\delta)}{\lambda} = \frac{-(z''\cos(HA) - x''\sin(HA))\sin(\delta) + y''\cos(\delta)}{\lambda}, \end{aligned} \tag{123}$$

and then that the u, v coordinates of the **B** vector projected on the plane perpendicular to the line-of-sight become

$$u = \frac{-\beta \sin(\varphi) \sin(HA) + \alpha \cos(HA)}{\lambda},$$
$$v = \frac{(\beta \sin(\varphi) \cos(HA) + \alpha \sin(HA)) \sin(\delta) + \beta \cos(\varphi) \cos(\delta)}{\lambda}. \quad (124)$$

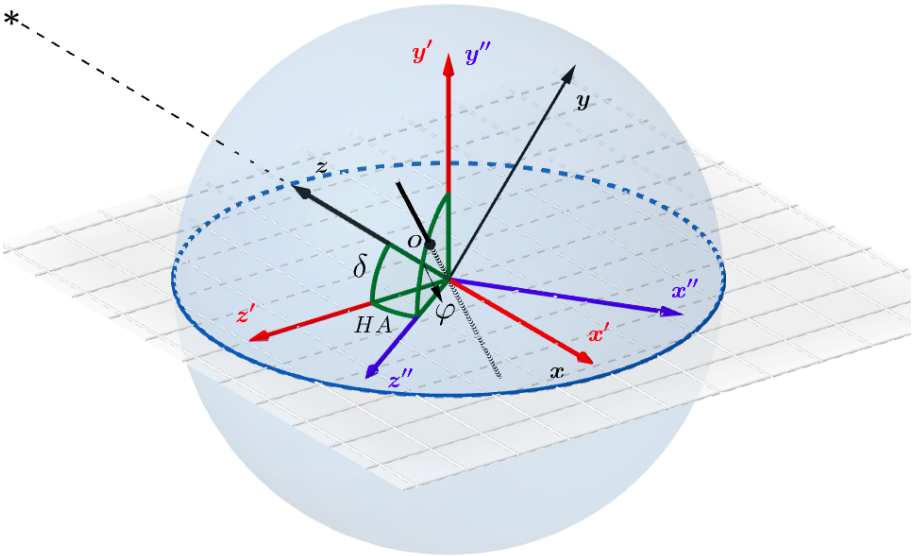

Figure 40. From the coordinate system S associated with the distant star to the system S" with respect to which the interferometer is fixed. The observer is located at the position O (see text).

The (u, v) dots illustrated in Figs. 38 & 39 were calculated by means of Eq. (124) for the following values of the parameters: $\alpha = 1.4$, $\beta = 2.6$, $\lambda = 1$, $\varphi = 52°$, $\delta = 10°$, $\zeta_0 = 1$, $\eta_0 = 1$ and $HA \in [-6$ hrs, ..., 6 hrs] by steps of 30 min.

Figure 41 shows the projected positions of 10 yellow telescope apertures composing an interferometer. We may mentally construct the various projected baselines between those apertures and visualize how the accessible (u, v) spatial frequencies change during the rotation of the globe supposed to represent the Earth as seen from a distant star. The video Rotating_Earth_UV_Plane.mp4 illustrating this can be downloaded via the URL: https://orbi.uliege.be/handle/2268/253241.

6 Some examples of interferometers

One of the most respected sanctuaries of optical interferometry was located on the plateau of Caussols, north of Grasse, in the south of France. The I2T (in French, "Interféromètre à 2 Télescopes"), made of 2 telescopes with an aperture of 26cm each and separated by a baseline of up to 144m was characterized by an angular resolution $\Phi \sim 0.001''$ attainable for objects with an apparent magnitude brighter than $V_{lim} \sim 6$ (see Figure 42, left). First interference fringes were obtained on Vega in 1975 (Fig. 42, right). About twenty angular

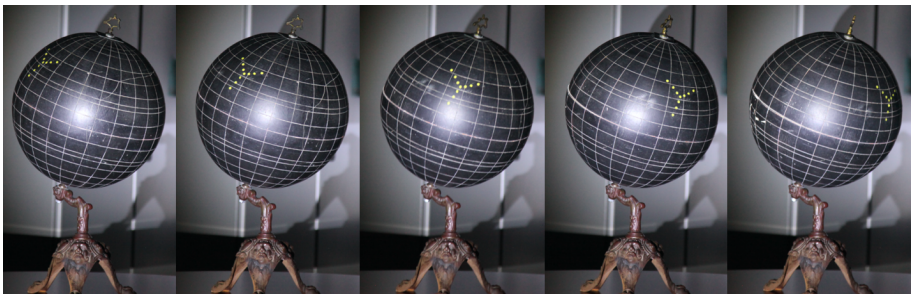

Figure 41. Projected positions of 10 telescope apertures as seen from a distant star while the Earth, represented by a globe, rotates as a function of time.

diameters of stars have been measured using the same I2T by Prof. Antoine Labeyrie and his close collaborators. In order to equalize the light paths collected from the stars passing through the two telescopes, optical delay lines are mandatory. These have been successfully used for the first time in 1975 (see Fig. 43 for an illustration of how delay lines work and Figs. 44 and 45 for views on modern optical delay lines in use at the VLTI, ESO, Chile).

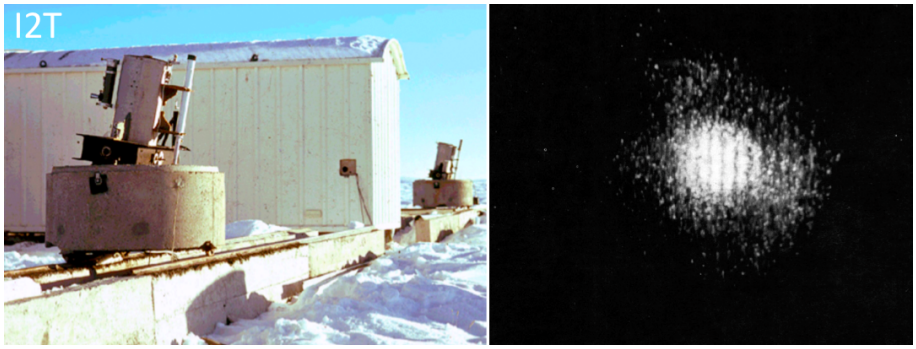

Figure 42. First fringes obtained with the I2T on Vega (Labeyrie et al. 1975, © Observatoire de la Côte d'Azur).

The GI2T (in French, "Grand Interféromètre à 2 Télescopes") composed of two 1.5m telescopes was subsequently used by the same team. The two big telescopes could in principle be set 2 km apart, corresponding to an angular resolution $\Phi \sim 0.0001''$ (see Fig. 46).

Since the beginning of the 21^{st} century, the modern sanctuary of stellar interferometry and aperture synthesis is undoubtedly the Very Large Telescope Interferometer (VLTI) of ESO (Southern European Observatory), located in Chile on Mount Paranal (see Fig. 47). The VLTI is a European interferometer that can re-combine the signal from 2, 3 or 4 telescopes depending on the instrument used. It has 4 telescopes of 8.2m and 4 mobile telescopes of 1.8m. Only telescopes of the same size can presently be re-combined together. The auxiliary telescopes of 1.8m can be easily moved from one each other allowing a better coverage of the (u, v) plane. The maximum base length of this interferometer is about 200m.

CHARA is another very performing interferometer located on the heights of Los Angeles, California (see Fig. 48). It is installed on the historic observatory of Mount Wilson. Remember that it was with the 2.5m telescope of this observatory that the first measurement of a stellar diameter was made by Michelson and Pease by installing a beam of 7m at the top of

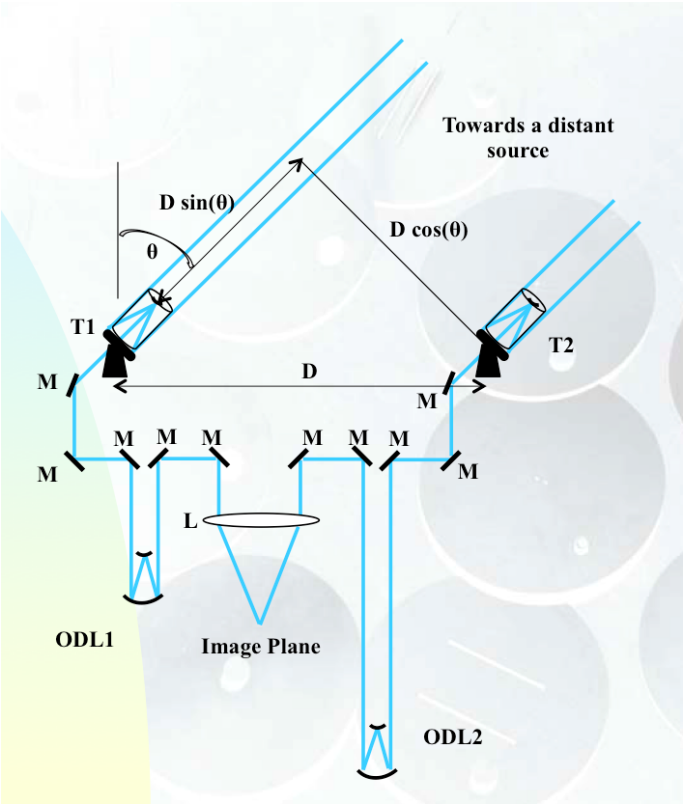

Figure 43. Use of optical delay lines to compensate for the continuous change in the lengths of the two light paths as the Earth rotates.

Figure 44. View inside the optical delay line tunnel of the VLTI at ESO, Paranal, Chile.

the telescope. The CHARA interferometric array, operational since 1999 is composed of 6 telescopes of 1m in diameter. These 6 telescopes can be either re-combined by 2, by 3 since 2008 and recently the 6 together. The maximum base length of this interferometer is 330m allowing to achieve an angular resolution of 200 μarcsec.

It is mainly used for angular diameter measurements but also for the detection and characterization of tight binary stars as well as for the detection of exo-zodiacal clouds (clouds of dust gravitating around the stars). Another famous optical/IR interferometer was the Keck

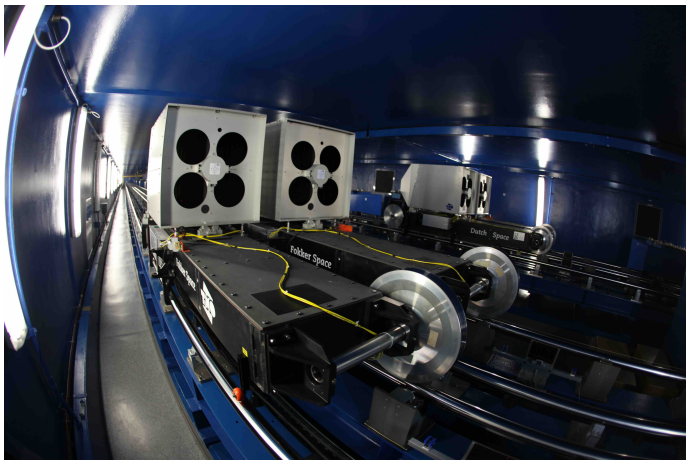

Figure 45. Zoom on one of the optical delay lines used in the tunnel of the VLTI at ESO, Paranal, Chile.

Figure 46. The GI2T constructed by Antoine Labeyrie and his close collaborators on the plateau of Caussols, north of Grasse, near Nice (France, © Observatoire de la Côte d'Azur)

.

Interferometer made of two 10m telescopes separated by a fixed baseline of 85m (see Fig. 49) on top of Mauna Kea (Hawaii, USA).

7 Three important theorems and some applications

When we previously established the relation existing between the structure of a celestial source and the visibility of the fringes observed with an interferometer (Sections 3.3 and 4.4), we implicitly assumed that the size of the apertures was infinitely small (pinhole apertures). Use of the fundamental theorem allows one to calculate the response function of an interferometer equipped with finite size apertures. This theorem actually formalizes, in mathematical terms, the physical connection existing between the focal plane and the pupil plane of an optical instrument (telescope, interferometer, grating, etc.). Use of the convolution theorem will then enable us to establish the relation between a celestial source that is extended and its observed image in the focal plane of an optical instrument. Finally, the Wiener-Khinchin theorem establishes the relation between the frequency content of the point spread function of an optical instrument and its pupil plane characteristics.

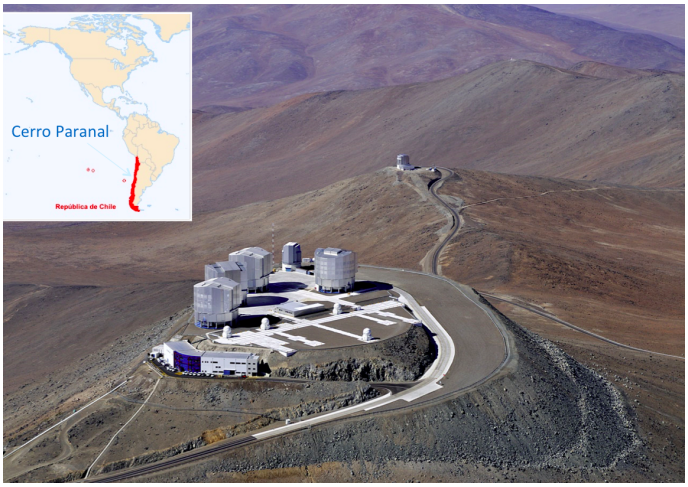

Figure 47. The Very Large Telescope Interferometer (VLTI) at the top of Paranal (Chile).

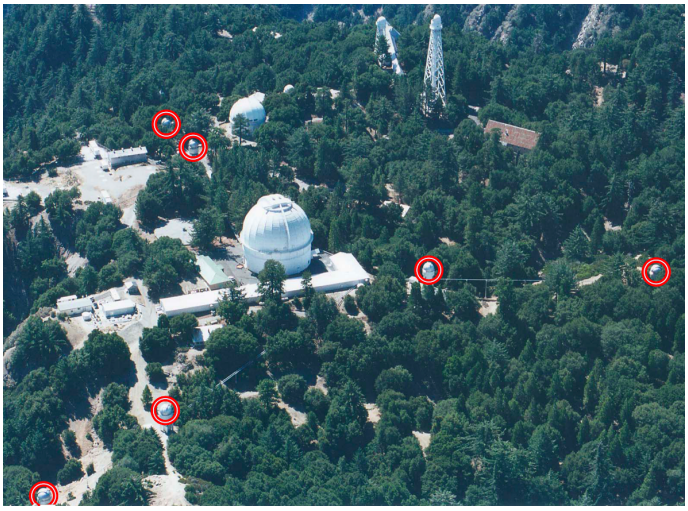

Figure 48. The CHARA interferometer composed of six 1m telescopes at Mount Wilson Observatory (California, USA). © The Observatories of the Carnegie Institution.

7.1 The fundamental theorem: relation between the pupil and focal planes

The fundamental theorem that we shall demonstrate here merely stipulates that given a converging optical system which can be assimilated to the lens or to the mirror of a telescope, or of an optical interferometer, the complex amplitude distribution $a(p, q)$ of the electromagnetic field of radiation in the focal plane is the Fourier transform of the complex amplitude distribution $A(x, y)$ of the electromagnetic field in the pupil plane, i.e.

$$a(p,q) = \int_{R^2} A(x,y) \exp\left[-i2\pi(px + qy)\right] dxdy, \tag{125}$$

or in a more compact form

$$a(p,q) = FT[A(x,y)](p,q), \tag{126}$$

with

$$p = \frac{x'}{\lambda f} \quad \text{and} \quad q = \frac{y'}{\lambda f}, \tag{127}$$

Figure 49. The Keck interferometer on top of Mauna Kea (Hawaii, USA). © Ethan Tweedie.

where x', y' refer to the Cartesian coordinates in the focal plane, λ to the wavelength of the monochromatic light under consideration and f to the effective focal length of the converging system.

Figure 50 represents a convergent optical system, its focal point F', its principal planes P, P' and its principal points H and H'. The latter degenerate with the optical center in the case of a thin lens or with the bottom of the dish in the case of a single mirror. The two orthonormal coordinate systems (O, x, y, z) and (F', x', y', z') make it possible to locate the input pupil plane and the image focal plane of the optical system. The term 'pupil plane' serves as the support for the definition of the vibration state at the entrance of the collector while the 'focal plane' serves as the support for the definition of the image that the collector gives of the source located at infinity. Defining the action of the collector is thus to establish the transformation that it operates on the radiation between these two planes.

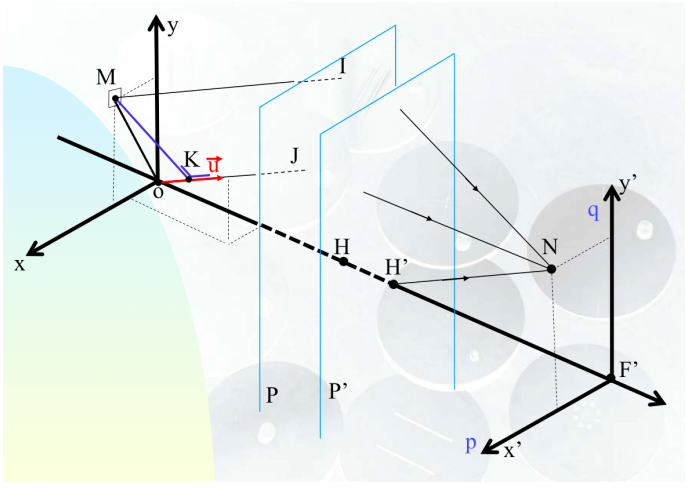

Figure 50. Fourier transform by a focusing optical system represented by its main planes P and P'. For the case of a thin lens, the latter would be degenerated into a single plane passing through its center.

The **hypotheses** underlying this theorem are:
H1. The optical system is free from any geometric aberration.
H2. The edges of the diaphragm do not disturb the electromagnetic field of radiation, that is to say that the diaphragm behaves as an "all (1) or nothing (0)" function with respect to this field. This is equivalent to assume that the dimensions of the collecting aperture(s) are large with respect to the wavelength of the light.
H3. No disturbance, other than those imposed by the optical system, intervenes between the pupil and the focal planes. The optical elements are thus assumed to be perfectly transparent or reflective.
H4. The light source is located at an infinite distance from the optical system and can thus be considered to be point-like.
H5. The disturbances occurring between the source and the pupil plane are weak and have very long evolution times relative to the period (i.e. $T = 1/\nu = \lambda/c$) of the radiation.
H6. The radiation is monochromatic and has a fixed polarization plane.

Theorem statement:
Within a multiplicative coefficient of the variables, the amplitude distribution in the focal plane is the Fourier transform of the amplitude distribution in the pupil plane.

Demonstration:
Consider the different points (x, y) of the pupil plane. H6 (i.e. the previous hypothesis 6) makes it possible to represent the electrical component of the electromagnetic field by the real part of the vibration distribution

$$A(x, y) \exp(i2\pi\nu t), \tag{128}$$

with the very general representation of the expression of the complex amplitude $A(x, y)$

$$A(x, y) = \mathcal{A}(x, y) \exp[i\Phi(x, y)]P_0(x, y), \tag{129}$$

where $\mathcal{A}(x, y)$ and $\Phi(x, y)$ represent the amplitude and phase of the electric field and $P_0(x, y)$ the input pupil function which is 1 inside the pupil and 0 outside (in agreement with H2 and H3).

In agreement with the Huygens-Fresnel principle, we will consider in the following that every point reached by a wave can be considered as a secondary source re-emitting a vibration with the same amplitude, the same frequency ν, the same polarization and the same phase (within a constant phase shift of $\pi/2$) as those of the incident vibration at this point. The point $N(x',y')$ of the focal plane will thus receive vibrations emitted by all the points of the pupil plane. The laws of geometrical optics, deduced from the Fermat principle, make it possible to write that the rays which, after the optical system, converge at the point N of the image focal plane, were, before the optical system, parallel to $H'N$. Having assumed that the source is at infinity (in agreement with H4), the amplitude will be preserved between the pupil plane and the focal plane. From the point $M(x,y)$ of the pupil plane, the point $N(x',y')$ of the focal plane will thus receive the vibration

$$A(x, y) \exp(i2\pi\nu t + i\Psi). \tag{130}$$

Let us take as the zero phase shift reference that of the ray passing through the point O along the direction OJN . The phase shift Ψ can then be expressed using the difference between the optical paths

$$\delta = d(MIN) - d(OJN), \tag{131}$$

where $d()$ refers to the distance along the specified path, and the relation

$$\Psi = 2\pi\delta/\lambda. \tag{132}$$

If the point K corresponds to the orthogonal projection of M onto OJ, M and K belong to the same wave plane which, after the optical system, will converge at the N point of the focal plane.
The Fermat principle, according to which the optical path between a point and its image is constant (rigorous stigmatism) or extremum (approximate stigmatism) makes it possible to write that the difference in optical path $(MIN)-(KJN)$ behaves in the neighborhood of zero as an infinitely small second order with respect to the $d(I,J)$ and thus also with respect to $d(O,M)$ and $d(O,K)$, which are of the same order as $d(I,J)$. As a result (see Fig. 50),

$$\delta = -d(O,K) = -|(\mathbf{OM}\,\mathbf{u})|, \tag{133}$$

$\mathbf{u}$ designating the unit vector along the direction $H'N$ and $(\mathbf{OM}\,\mathbf{u})$ the scalar product between the vectors $\mathbf{OM}$ and $\mathbf{u}$. If the angle that $H'N$ makes with the optical axis is small, the vector of components $(x'/f,\, y'/f,\, 1)$ is the vector director of $H'N$ and has a norm close to 1 (at first order because $f >> |x'|, |y'|$). Moreover, $\mathbf{OM}$ has for components $(x,\, y,\, 0)$. Using Eq. (133) in (132), the expression (130) becomes

$$A(x,y)\exp\left(i2\pi\nu t - xx'/\lambda f - yy'/\lambda f\right). \tag{134}$$

Choosing as new variables in the focal plane those defined in (127), we get

$$A(x,y)\exp\left[-i2\pi(xp+yq)\right]\exp\left(i2\pi\nu t\right). \tag{135}$$

gular re The resulting vibration at the point N will be the resultant of the vibrations transmitted towards N by all the points of the pupil plane.
The equi-phase wave surfaces which reach the pupil plane are not planes if the radiation has been disturbed between the source and the entrance pupil. But the hypotheses $H4$ and $H5$ make it possible to affirm that the pupil plane is spatially coherent, that is to say that at the time scale of the vibration periods, the relative phase shift of its different points is constant. Consequently, to calculate the resulting vibration at the point $N(p,q)$ of the focal plane, it is necessary to sum up the amplitudes that N receives from the different points of the pupil plane. The amplitude distribution $a(p,q)$ in the focal plane then becomes

$$a(p,q) = \int_{R^2} A(x,y)\exp\left[-i2\pi(xp+yq)\right]dxdy, \tag{136}$$

that is, the complex amplitude distribution in the focal plane $a(p,q)$ is the Fourier transform of the complex amplitude distribution $A(x,y)$ in the pupil plane, i.e.

$$a(p,q) = FT[A(x,y)](p,q). \tag{137}$$

Simulations illustrating all the concepts of the fundamental theorem have been prepared using the Geogebra open source applications (https://www.geogebra.org). They can be viewed on the videos Fundamental_Th_1.mp4 and Fundamental_Th_2.mp4 to be downloaded via the URL: https://orbi.uliege.be/handle/2268/253241.

7.1.1 Applications of the fundamental theorem

(i) The case of a single square aperture

Considering first the case of a single square aperture as depicted in Fig. 51 (left) and a point-like source perfectly located at zenith, i.e. the plane wavefronts arrive parallel to the aperture with a constant and real amplitude $A(x, y) = A_0$, we find that the calculation of the amplitude in the focal plane is straightforward

$$a(p, q) = A_0 \, FT[\Pi(x/a) \, \Pi(y/a)](p, q). \tag{138}$$

Making use of the separation of the variables x, y and of the relation (86), Eq. (126) successively transforms into

$$a(p, q) = A_0 \, FT[\Pi(x/a)](p) \, FT[\Pi(y/a)](q), \tag{139}$$

$$a(p, q) = A_0 \, a^2 \, \frac{sin(\pi ap)}{\pi ap} \, \frac{sin(\pi aq)}{\pi aq}. \tag{140}$$

This is the impulse response, in amplitude, for a square pupil and in the absence of any external disturbance. Adopting the definition (10) for the intensity of the vibrations, we find that (see Fig. 51, at right)

$$i(p, q) = a(p, q) \, a^*(p, q) = |a(p, q)|^2 = i_0 \, a^4 \, [\frac{sin(\pi ap)}{\pi ap}]^2 \, [\frac{sin(\pi aq)}{\pi aq}]^2. \tag{141}$$

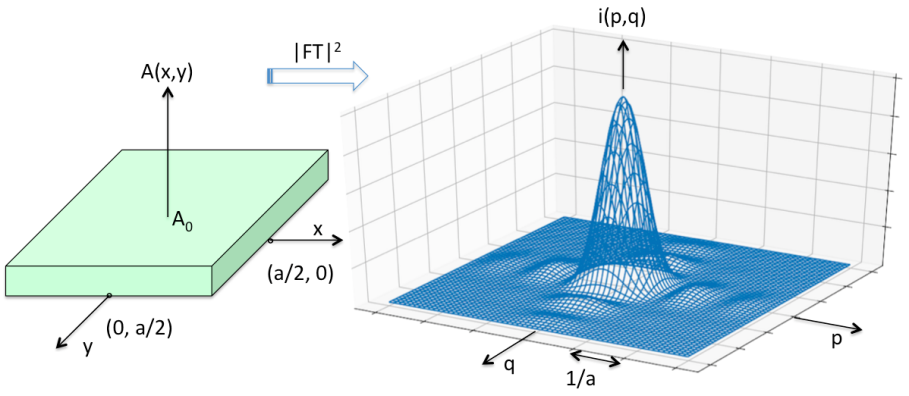

Figure 51. Complex amplitude distribution $A(x, y)$ in the plane of a single square aperture (left) and resulting response function in intensity $i(p, q)$ (right).

Defining the angular resolution Φ of an optical system as being the angular width of the response function in intensity between the first minima, we obtain for the values of $\pi pa = \pm\pi$ (resp. $\pi qa = \pm\pi$), i.e. $p = \pm 1/a$ (resp. $q = \pm 1/a$) and with the definition (127) for p, q

$$\frac{x'}{\lambda f} = \pm\frac{1}{a} \quad (\text{resp.} \quad \frac{y'}{\lambda f} = \pm\frac{1}{a}), \tag{142}$$

$$\Phi = \frac{\Delta x'}{f} = \frac{\Delta y'}{f} = \frac{2\lambda}{a}. \tag{143}$$

The angular resolution Φ is thus inversely proportional to the size a of the square aperture, and proportional to the wavelength λ. Working at short wavelengths with a big size aperture thus confers a better angular resolution.

Up to now, we have considered that the source S, assumed to be point-like and located at an infinite distance from the optical system, was on the optical axis of the instrument. Suppose now that it is slightly moved away from the zenith direction by a small angle. Let $(b/f, c/f, 1)$ be the unit vector representing the new direction of the source, the previous one being (0, 0, 1). The plane wavefront falling on the square aperture will not have anymore a constant amplitude A_0 because each point of the pupil touched by such a wavefront will experience a phase shift given by the angle

$$\Psi = \frac{2\pi\delta}{\lambda} = \frac{2\pi(xb/f + yc/f)}{\lambda} \tag{144}$$

and consequently the correct expression of the complex amplitude $A(x, y)$ to be inserted in Eq. (126) becomes

$$A(x, y) = A_0\, \Pi(x/a)\Pi(y/a)\, \exp[\frac{i2\pi(xb/f + yc/f)}{\lambda}]. \tag{145}$$

Proceeding as previously, we easily find that

$$a(p, q) = A_0\, FT[\Pi(\frac{x}{a})](p - \frac{b}{\lambda f})\, FT[\Pi(\frac{y}{a})](q - \frac{c}{\lambda f}) \tag{146}$$

and finally

$$i(p, q) = a(p, q)\, a^*(p, q) = |a(p, q)|^2 = i_0\, a^4 \left[\frac{sin[\pi a(p - \frac{b}{\lambda f})]}{\pi a(p - \frac{b}{\lambda f})}\right]^2 \left[\frac{sin[\pi a(q - \frac{c}{\lambda f})]}{\pi a(q - \frac{c}{\lambda f})}\right]^2. \tag{147}$$

The resulting intensity response function in the focal plane is nearly the same as the one previously calculated for the case $b = 0, c = 0$. It is being merely translated by a linear offset (b, c) in the x', y' focal plane and implies the invariance of the response function for a reference star that is being slightly offset from the optical axis of the system.

(ii) The case of a circular aperture

Considering now a circular aperture with radius R, the complex amplitude $A(x, y)$ in the pupil plane may be represented as a circular symmetric distribution, i.e. $A(\rho, \varphi) = A_0$ for $\rho < R, \varphi \in [0, 2\pi]$ and $A(\rho, \varphi) = 0$ for $\rho > R$ (see Figure 52, at left). We naturally expect the distribution of the complex amplitude in the focal plane to be also circular symmetric, i.e.

$$a(\rho') = FT[A(\rho, \varphi)](\rho'). \tag{148}$$

It is here interesting to note that performing the above Fourier transform is quite alike deriving the expression of the visibility of a $2-D$ uniform circular disc star which angular diameter is θ_{UD} (see the last application in Section 4.5). We may just make use of the result (108) with appropriate changes of the corresponding variables. We easily find that

$$a(\rho') = A_0\pi R^2[2J_1(\frac{2\pi R\rho'/(\lambda f)}{2\pi R\rho'/(\lambda f)})]. \tag{149}$$

The resulting intensity response function is thus given by

$$i(\rho') = a(\rho')^2 = A_0^2(\pi R^2)^2[2J_1(\frac{2\pi R\rho'/(\lambda f)}{2\pi R\rho'/(\lambda f)})]^2. \tag{150}$$

This is the very expression of the famous Airy disc (see Fig. 52, at right).

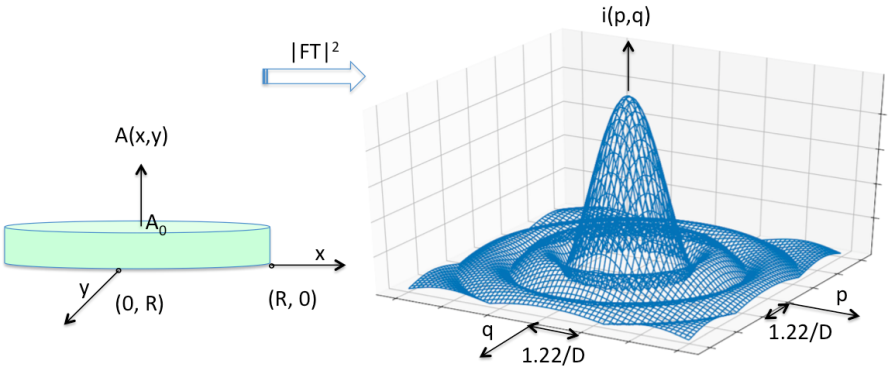

Figure 52. The Airy disc: complex amplitude distribution $A(\rho, \varphi) = A_0$ in the plane of a circular aperture (left) and the resulting response function in intensity $i(\rho')$ (right).

Knowing that the first order Bessel function $J_1(x) = 0$ for $x \sim 3.96$, it is easy to deduce that the angular resolution Φ of a telescope equipped with a circular objective which diameter is $D = 2R$ is given by

$$\Phi = \frac{\Delta\rho'}{f} = \frac{2.44\,\lambda}{D}. \tag{151}$$

(iii) The two telescope interferometer

Figure 53 (upper left) illustrates the principle of optically coupling two telescopes. Such a system is equivalent to a huge telescope in front of which would have been placed a screen pierced with two openings corresponding to the entrance pupils of the two telescopes. The pupil function $A(x, y)$ of this system is shown in that same Figure for the case of two square apertures.

Let us now calculate the impulse response function $a(p, q)$ of such a system. Representing the distribution of the complex amplitude over each of the individual square apertures by means of the function $A_0(x, y)$ and assuming that the distance between their optical axes is B, we find that

$$a(p, q) = FT[A_0(x + B/2, y) + A_0(x - B/2, y)](p, q). \tag{152}$$

Making use of the relation (80), the previous equation reduces to

$$a(p, q) = [\exp(i\pi pB) + \exp(-i\pi pB)]\, FT[A_0(x, y)](p, q), \tag{153}$$

$$a(p, q) = 2\, cos(\pi pB)\, FT[A_0(x, y)](p, q) \tag{154}$$

and finally

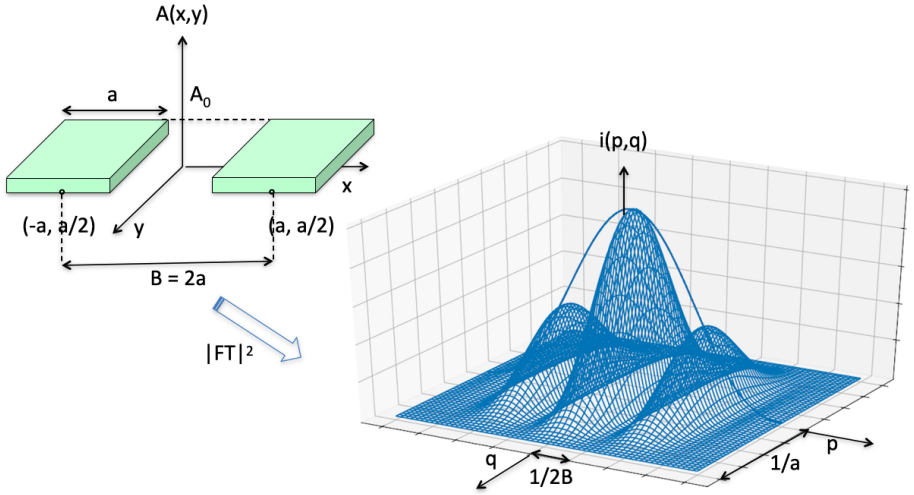

Figure 53. The two telescope interferometer: distribution of the complex amplitude for the case of two square apertures (upper left) and the corresponding impulse response function (lower right).

$$i(p,q) = a(p,q)a^*(p,q) = |a(p,q)|^2 = 4\,cos^2(\pi pB)\,\{FT[A_0(x,y)](p,q)\}^2. \tag{155}$$

Particularizing this intensity distribution to the case of two square apertures, or circular apertures, and making use of relations (141) or (150) leads to the respective results

$$i(p,q) = A_0^2\,(2a^2)^2\,[\frac{sin(\pi pa)}{\pi pa}]^2\,[\frac{sin(\pi qa)}{\pi qa}]^2\,cos^2(\pi pB) \tag{156}$$

or

$$i(p,\rho') = A_0^2(2\,\pi R^2)^2[\frac{2J_1(2\pi R\rho'/(\lambda f))}{2\pi R\rho'/(\lambda f)}]^2\,cos^2(\pi pB). \tag{157}$$

Figure 53 (lower right) illustrates the response function for the former case. We see that the impulse response of each individual telescope is modulated by the $\cos(2\pi pB)$ function and that the resulting impulse response function shows consequently a more detailed structure along the p axis, leading to a significantly improved angular resolution Φ along that direction. The angular width Φ of the bright central fringe is equal to the angular width separating the two minima located on its two sides. We thus find successively

$$\pi pB = \pm\frac{\pi}{2}, \tag{158}$$

$$p = \pm\frac{1}{2B}, \tag{159}$$

$$\Delta p = \frac{1}{B} \tag{160}$$

and making use of relation (127)

$$\Phi = \frac{\Delta x'}{f} = \frac{\lambda}{B}. \tag{161}$$

The angular resolution of the interferometer along the direction joining the two telescopes is approximately equivalent to that of a single dish telescope which diameter is equal to the baseline B separating them, and not any longer to the diameter D of each single telescope (see Eqs. (143) or (151)).

From all the previous relations, we find that the angular resolution Φ of an optical instrument characterized by (a) a circular aperture having a diameter D, (b) a square aperture with a side a and (c) an interferometer with a baseline B are respectively:

$$\begin{aligned} \Phi &= \frac{\lambda}{\frac{D}{2.44}}, \ (a) \\ \Phi &= \frac{\lambda}{\frac{a}{2}}, \ (b) \\ \Phi &= \frac{\lambda}{\frac{B}{1}}. (c) \end{aligned} \tag{162}$$

We then naturally conclude that given a circular aperture with a diameter D, the best would be to mask the whole aperture at the exception of two holes separated by a baseline D which would confer to that facility an angular resolution $\Phi = \lambda/D$ which is superior by a factor 2.44 to the angular resolution $\Phi = 2.44\lambda/D$ characterizing the full circular aperture. Using in parallel adaptive optics, masking interferometry has been frequently used by astronomers to get the best angular resolution out of a single aperture telescope.

7.1.2 Other types of beam recombination

When establishing the expression for the response function of an interferometer composed of two single square or circular apertures (see Section 6.1.3, Eqs. (156-157)), we implicitly assumed that the exit pupil perfectly matched the entrance pupil (see Figs. 14, 15, 19 and 54). The baseline B between the two entrance pupil apertures was indeed equal to the baseline B' between the two exit pupil apertures.

This type of recombination of the two beams is referred to as the Fizeau-type or homothetic one. As we have seen in Section 3.4, Michelson and Pease have used another type of beam recombination, known as the Michelson Stellar Interferometer or still, the densified recombination type (see Fig. 55).

When the two exit beams are being superimposed, resulting in the baseline $B' = 0$, the recombination is referred to as being co-axial, or the Michelson Interferometer type (see Fig. 56).

A more general model of beam recombination, that includes the three previously described ones, is illustrated in Fig. 57. Two main collectors receive the light beams from a distant celestial source. While passing through the beam reducers, the beams are compressed by a magnification factor M, corresponding to the ratio between the focal lengths of the two lenses of the focal reducers. The two compressed beams are then relayed by means of a set of 4 mirrors, just like in the Michelson Stellar Interferometer. Before entering the exit pupil of the recombining lens, their separation or baseline is $B' < B$. To calculate the response function of such an interferometer, we just need to apply the fundamental theorem to this

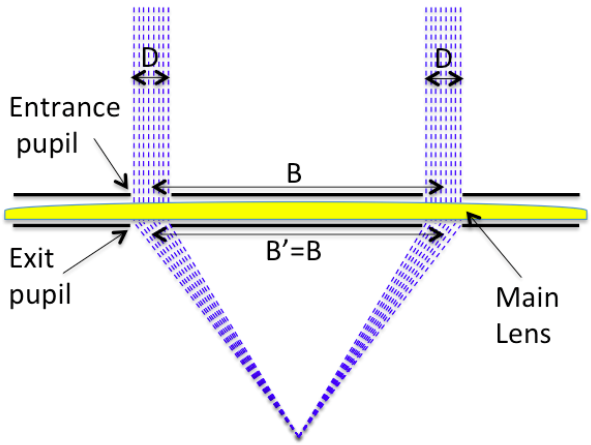

Figure 54. The two beams of light rays, represented with blue dashed lines, collected by the two entrance pupil apertures are separated by a baseline B which is identical to the baseline B' between the two apertures in the exit pupil plane of the main converging lens.

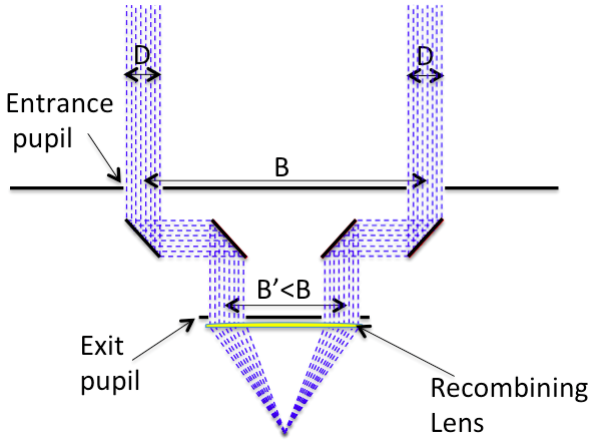

Figure 55. Sketch of the Michelson Stellar Interferometer. The baseline B between the two entrance pupil apertures is much larger than the baseline B' between the two apertures in front of the recombining lens. The 45° inclined black lines symbolize reflective plane mirrors. In the case of the Michelson-Pease experiment, these four mirrors were set on a 7m beam just above the 2.5m Wilson telescope (see Fig. 20).

secondary Fizeau-type interferometer with a baseline B', taking into account the correct expression for the distribution of the complex amplitude of the electric field over the two exit pupil apertures.

Considering a point-like celestial source emitting a plane wave making an angle θ_0 with respect to the line joining the two telescopes, the angle between the outcoming beam - compressed in size by the magnification factor $M(= f_{in}/f_{out})$ - and the main axis of the optical

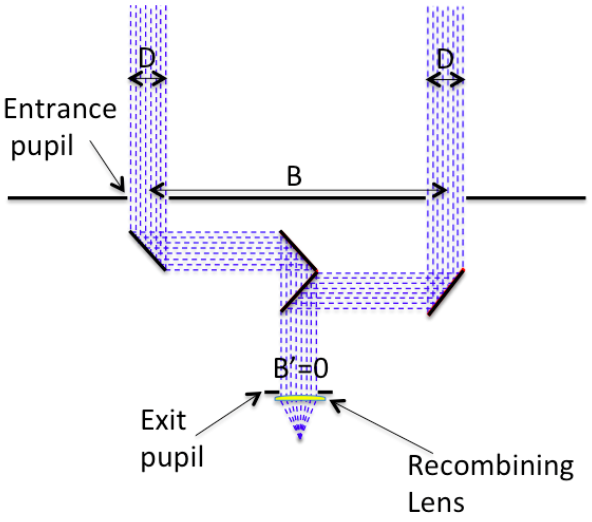

Figure 56. The Michelson Interferometer. In this case, the beam recombination is co-axial corresponding to the exit pupil baseline $B' = 0$.

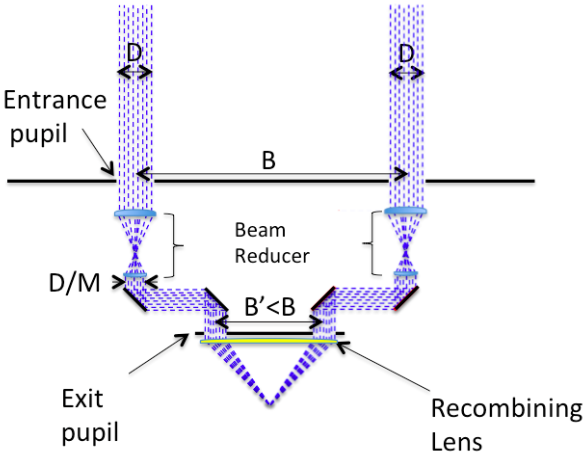

Figure 57. General case of beam recombination. The two beams of parallel light rays from a distant celestial source are first collected by two unit telescopes having a diameter D. The beams are then compressed by a magnification factor M. They are subsequently relayed by a system of plane mirrors to the exit pupil of the recombining lens. At that stage, their separation (baseline) is $B' < B$.

system is $M\theta_0$ (since $\sin[\theta_0] \simeq \theta_0$, given that $\theta_0 << 1$, see Fig. 58). The resulting complex amplitude in the focal plane of the recombining lens is along the p direction, i.e. along the line joining the two exit pupil apertures (see Fig. 59 and Eq. (125))

$$a(p) = FT[A_1(x)](p) + FT[A_2(x)](p) \tag{163}$$

where $A_1(x)$ and $A_2(x)$ represent the distribution of the complex amplitude in the two exit pupil apertures along the x axis.

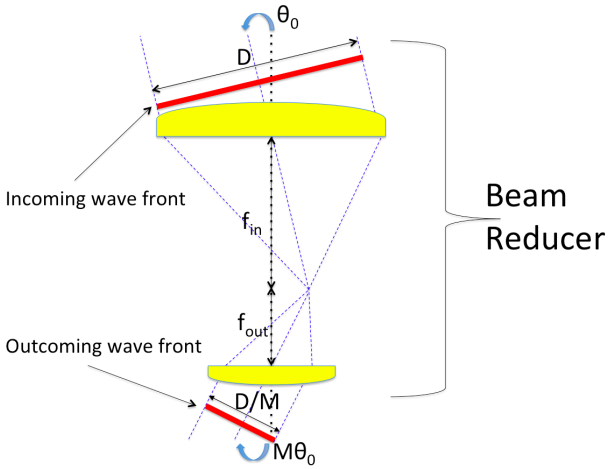

Figure 58. Propagation of an incoming plane wave from a distant celestial object with an inclination angle θ_0 through a beam reducer. The beam size is being reduced by the magnification factor $M = f_{in}/f_{out}$ while the outcoming direction of the beam has changed into $M\theta_0$.

We subsequently find that

$$FT[A_1(x)](p) = \int_{-(B'+D/M)/2}^{-(B'-D/M)/2} M \exp[-2i\pi(px)] \exp[2i\pi M \sin[\theta_0](x - (B/M - B')/2)/\lambda] dx,$$
$$FT[A_2(x)](p) = \exp[2i\pi(d/\lambda)] \int_{(B'-D/M)/2}^{(B'+D/M)/2} M \exp[-2i\pi(px)] \exp[2i\pi M \sin[\theta_0](x + (B/M - B')/2)/\lambda] dx. \quad (164)$$

In this expression, we have taken into account the fact that most of existing interferometers are equipped with a delay line and we have assumed here that an extra length d affects the path of the second beam. This explains the origin of the factor $\exp[2i\pi(d/\lambda)]$ in the expression of $FT[A_2(x)](p)$. The limits of integration are straightforward to establish (see Fig. 59, Level 3). The presence of the factor M merely accounts for the fact that when a beam is compressed, its constant amplitude is being multiplied by M (and the intensity $i(p)$ by M^2 in order to preserve energy conservation). The factor $\exp[-2i\pi(px)]$ merely accounts for the pupil-to-image relationship from Fourier optics (cf. the fundamental theorem). Since for the case of a co-phased array, the path differences affecting the arrival of the plane waves at the centres of the two apertures at Level 1 in Fig. 59 are $+\delta$ and $-\delta$ ($= \pm(B/2)\sin[\theta_0] \simeq \pm(B/2)\theta_0$), the latter remain unaffected when reaching the centres of the two apertures in the exit pupil plane (Level 3). Nevertheless, their relative inclination has changed from θ_0 to $M\theta_0$. Therefore, we easily understand the origin of the two factors $\exp[2i\pi M \sin[\theta_0](x - (B/M - B')/2)/\lambda]$ and $\exp[2i\pi M \sin[\theta_0](x + (B/M - B')/2)/\lambda]$ appearing in the two previous equations. After several successful changes of variables (see Appendix), Eq. (163) reduces to

$$a(p) = 2D \exp[i\pi(d/\lambda)] \frac{\sin[(\pi D/M)(p - M\sin[\theta_0]/\lambda)]}{(\pi D/M)(p - M\sin[\theta_0]/\lambda)} \cos[\pi(B'p + (d - B\sin[\theta_0])/\lambda)]. \quad (165)$$

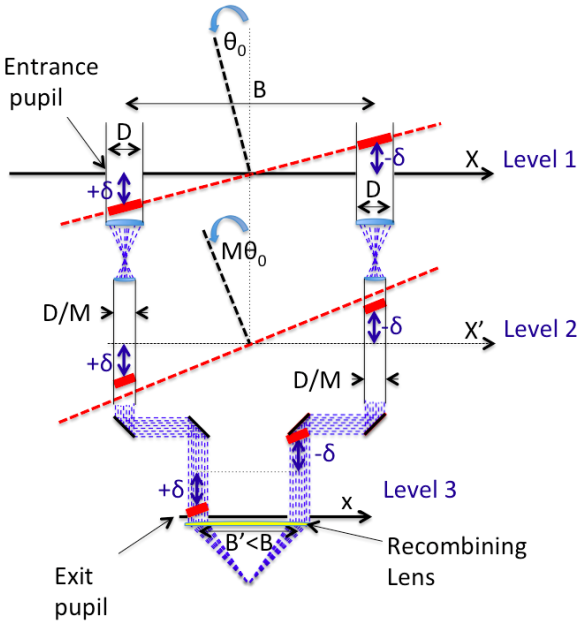

Figure 59. Propagation of an incoming plane wave from a distant celestial object with an inclination angle θ_0 through two beam reducers (Level 1 - Level 2). When arriving in the exit pupil plane (Level 3), the delays $\pm\delta$ of the plane waves near the centres of the two apertures are the same but their inclination is now $M\theta_0$.

The corresponding expression for the intensity $i(p) = |a(p)|^2$ becomes

$$i(p) = 4D^2 \left[\frac{\sin[(\pi D/M)(p - M\sin[\theta_0]/\lambda)]}{(\pi D/M)(p - M\sin[\theta_0]/\lambda)}\right]^2 [\cos[\pi(B'p + (d - B\sin[\theta_0])/\lambda)]]^2. \quad (166)$$

The previous equations describe the response function of any interferometer having its entrance and exit baselines such as $0 \leq B' \leq B$.

In the absence of an internal delay d, the previous expression for $i(p)$ can be rewritten as

$$i(p) = 4D^2 \left[\frac{\sin[(\pi D/M)(p - M\sin[\theta_0]/\lambda)]}{(\pi D/M)(p - M\sin[\theta_0]/\lambda)}\right]^2 [\cos[\pi B'(p - B\sin[\theta_0]/(B'\lambda)]]^2. \quad (167)$$

Some nice features become outstanding: we first notice that the width of the envelope function is governed by the factor $\pi D/M$ which is related to the size of the beam after compression. The angular separation of the fringes (λ/B') is essentially determined by the exit pupil baseline B'. It does neither depend on the main baseline B nor on the magnification (or beam compression) M. This last equation also reveals that for the response function to be field invariant, we must have $M = B/B'$. In that case, the centre of the main envelope (cf. Airy disc for the case of a circular aperture) will always coincide with the central fringe peak, whatever the position (θ_0) of the source in the field of view.

Let us now consider the case of Fizeau-type interferometry for which we have $d = 0$ (no delay line is being used) and in addition $M = 1$, $B' = B$, also $\sin[\theta_0] \simeq \theta_0$, Eq. (167) then reduces to

$$i(p) = 4D^2 \left[\frac{\sin[(\pi D)(p-\theta_0/\lambda)]}{(\pi D)(p-\theta_0/\lambda)}\right]^2 \left[\cos[\pi(B(p-\theta_0/\lambda))]\right]^2. \quad (168)$$

Posing $\theta_0 = b/f$ in the latter equation, we simply recover the result previously established for the case of Fizeau interferometry (see Eqs. (147) and (156)). We also note here that the response function of a Fizeau-type interferometer is field invariant.

Finally, the response function of a co-axial interferometer is easily derived by inserting the value $B' = 0$ in Eq. (166):

$$i(p) = 4D^2 \left[\frac{\sin[(\pi D/M)(p-M\theta_0/\lambda)]}{(\pi D/M)(p-M\theta_0/\lambda)}\right]^2 \left[\cos[\pi(d-B\theta_0)/\lambda]\right]^2. \quad (169)$$

We note here that the cos factor is only a function of d and θ_0, and not any longer of p.

In conclusion, we have established in this section a very general expression (see Eq. (166)) for the response function of an interferometer composed of two similar apertures separated by a baseline B and which beams have been compressed by a magnification factor M. In the exit pupil plane, the new baseline between the two beams is B' ($0 < B' < B$) such that the fringe separation is essentially governed by the latter term.

7.2 The convolution theorem

The fundamental theorem has allowed us to take into account the finite size of the apertures of an optical system instead of considering that the apertures are made of pinholes. However, we have considered that the source is point-like. To treat the case of an extended source, we shall make use of the convolution theorem.

The convolution theorem states that the convolution of two functions $f(x)$ and $g(x)$ is given by the following expression

$$f(x) * g(x) = (f * g)(x) = \int_R f(x-t)g(t)dt. \quad (170)$$

Figure 60 illustrates such a convolution product for the case of two rectangular functions $f(x) = \Pi(x/a)$ and $g(x) = \Pi(x/b)$ having the widths a and b, respectively.

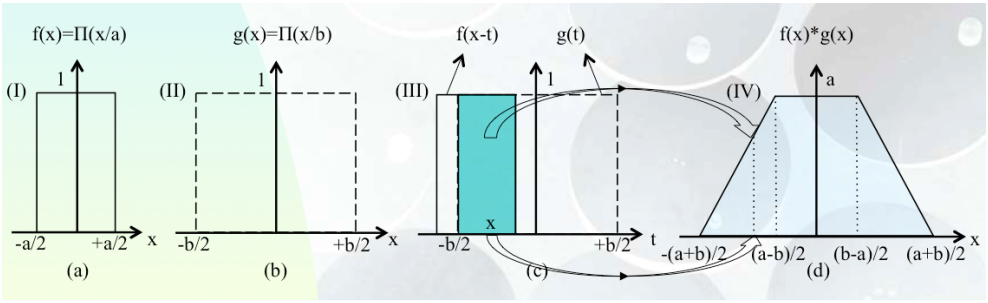

Figure 60. Convolution product of two 1-D rectangular functions. (a) $f(x)$, (b) $g(x)$, (c) $g(t)$ and $f(x-t)$. The dashed area represents the integral of the product of $f(x-t)$ and $g(t)$ for the given x offset, (d) $f(x) * g(x) = (f * g)(x)$ represents the previous integral as a function of x.

Every day when the Sun is shining, it is possible to see nice illustrations of the convolution product while looking at the projected images of the Sun on the ground

which are actually produced through small holes in the foliage of the trees (see the illustration in Fig. 61 and the video Solar_Discs.mp4 to be downloaded via the URL: https://orbi.uliege.be/handle/2268/253241).

It is a good exercise to establish the relation existing between the observed surface brightness of those Sun images, the shape of the holes in the foliage of the trees, their distance from the ground and the intrinsic surface brightness distribution of the Sun. A nice tool to simulate convolved products of the Sun image with different types (square, heart, ...) of apertures has been designed by Mr. Pierre Collette and is accessible on the web via the URL: http://users.skynet.be/pcollette/camobs.html.

Figure 61. Projected images of the Sun on the ground actually produced through small holes in the foliage of trees (bamboo trees at IUCAA, Pune, India, June 2016). These images actually result from the convolution of the intrinsic Sun intensity distribution and the shapes of the holes in the trees.

7.2.1 The convolution theorem

A very powerful and efficient theorem that we shall make use just hereafter states that the Fourier transform of the convolution product of two functions is simply given by the direct product of their Fourier transforms, i.e.

$$FT[f(x) * g(x)](s) = FT[f(x)](s)\, FT[g(x)](s). \tag{171}$$

The demonstration of the so-called convolution theorem is rather straightforward. Indeed,

$$FT[f(x) * g(x)](s) = \int \int f(y)g(x-y)dy \exp(-i2\pi xs)dx. \tag{172}$$

Making use of the change of variables

$$\begin{aligned} z &= x - y, \text{ and thus} \\ dz &= dx, \end{aligned} \tag{173}$$

the previous equation successively transforms into

$$\begin{aligned} FT[f(x) * g(x)](s) = \int \int f(y)g(z)dy \exp(-i2\pi(z+y)s)dz = \\ \int f(y) \exp(-i2\pi ys)dy \int g(z) \exp(-i2\pi zs)dz = \\ FT[f(x)](s)\, FT[g(x)](s). \end{aligned} \tag{174}$$

Similarly, it is easy to prove that the Fourier transform of the direct product of two functions is merely given by the convolution product of their Fourier transforms

$$FT[f(x)\,g(x)](s) = FT[f(x)](s) * FT[g(x)](s). \tag{175}$$

As before we successively find that

$$\begin{aligned} FT[f(x)](s) * FT[g(x)](s) = \int\int f(x)\exp(-i2\pi xt)dx \int g(y)\exp(-i2\pi y(s-t))\,dy\,dt = \\ \int\int f(x)\,g(y)\int \exp(-i2\pi(x-y)t)dt\exp(-i2\pi ys)\,dy\,dx = \\ \int\int f(x)\,g(y)\,\delta(x-y)\exp(-i2\pi ys)\,dy\,dx = \\ \int f(y)\,g(y)\exp(-i2\pi ys)\,dy = \\ FT[f(y)\,g(y)](s). \end{aligned} \tag{176}$$

7.2.2 Application to the case of the two telescope interferometer

We have previously seen that for the case of a point-like source having an intrinsic surface brightness distribution $O(p,q) = \delta(p)\delta(q)$, there results the formation of an image $e(p,q)$ in the focal plane which is the impulse response $e(p,q) = i(p,q) = |a(p,q)|^2$ of the optical instrument (see Eqs. (141), (150), (156), (157) for the case of a single square aperture, a single circular aperture, an interferometer composed of two square or circular apertures, respectively). Considering now an extended source represented by its intrinsic surface brightness distribution $O(p,q)$, application of the convolution theorem in two dimensions directly leads to the expression of its brightness distribution $e(p,q)$ in the focal plane of the optical system

$$e(p,q) = O(p,q) * |a(p,q)|^2 \tag{177}$$

or more explicitly

$$e(p,q) = \int_{R^2} O(r,s)|a(p-r,q-s)|^2 dr ds. \tag{178}$$

Since the Fourier transform of the convolution product of two functions is equal to the product of their Fourier transforms, we find that

$$FT[e(p,q)] = FT[O(p,q)]\,FT[|a(p,q)|^2] \tag{179}$$

and also that the inverse Fourier transform of $FT[O(p,q)]$ leads to the result

$$O(p,q) = FT^{-1}[FT[O(p,q)]] = FT^{-1}[\frac{FT[e(p,q)]}{FT[|a(p,q)|^2]}], \tag{180}$$

namely, that it should be possible to recover interesting information on the intrinsic surface brightness distribution of the source $O(p,q)$ at high angular resolution provided that we get sufficient information at high frequencies in the (u,v) plane on the object $FT[e(p,q)]$ itself as well as on a reference point-like object $FT[|a(p,q)|^2]$.

7.2.3 Interferometric observations of an extended celestial source

Considering the case of a celestial source observed with a two-telescope aperture interferometer and represented by its intrinsic brightness distribution $O(p,q)$, we find by means of Eqs. (156) and (177) that

$$e(p,q) = O(p,q) * \left[|a_0(p,q)|^2 \cos^2(\pi p B) \right], \tag{181}$$

where $|a_0(p,q)|^2$ represents the response function of each of the two individual but similar apertures composing the interferometer and separated along the X axis by the baseline B.

Since we assume that none of the individual apertures allows one to resolve the source, the previous equation reduces to

$$e(p,q) = |a_0(p,q)|^2 \left[O(p,q) * \cos^2(\pi p B) \right]. \tag{182}$$

Making use of the trigonometric relation $\cos(2x) = 2\cos^2(x) - 1$, the previous equation may be re-written as

$$e(p,q) = |a_0(p,q)|^2 \left[\frac{1}{2} \int_R O(p,q) dp\, dq + \frac{1}{2} O(p,q) * \cos(2\pi p B) \right], \tag{183}$$

or still

$$e(p,q) = |a_0(p,q)|^2 \, \frac{1}{2} \int_R O(p,q) dp\, dq \left[1 + \frac{O(p,q)}{\int_R O(p,q) dp\, dq} * \cos(2\pi p B) \right]. \tag{184}$$

Representing the normalized intensity distribution by the quantity

$$O'(p,q) = \frac{O(p,q)}{\int_R O(p,q) dp} \tag{185}$$

and defining the multiplicative constant

$$A = |a_0(p,q)|^2 \, \frac{1}{2} \int_R O(p,q) dp\, dq, \tag{186}$$

we subsequently obtain

$$e(p,q) = A \left[1 + O'(p,q) * \cos(2\pi p B) \right]. \tag{187}$$

Detailing the above convolution product as

$$e(p,q) = A \left[1 + \int \int O'(r,s) \cos[2\pi(p-r)B] dr ds \right], \tag{188}$$

and since $O'(r,s)$ is a real function, the previous equation may be transformed as follows

$$e(p,q) = A \left[1 + \Re \left\{ \int O''(r) e^{-i2\pi r B} dr \, e^{i2\pi p B} \right\} \right], \tag{189}$$

where

$$O''(r) = \int O'(r,s) ds \tag{190}$$

represents the normalized intensity distribution of the source integrated along the s axis and $\mathfrak{R}$ the real part of the expression between the curly brackets.

Defining the complex quantity (also known as the complex degree of mutual coherence, cf. Eq. (30))

$$\gamma(B) = \int O''(r) e^{-i2\pi rB} dr, \tag{191}$$

which may be rewritten as

$$\gamma(B) = |\gamma(B)| e^{i\beta}, \tag{192}$$

we obtain

$$e(p,q) = A\left[1 + |\gamma(B)| \cos\left(2\pi pB + \beta\right)\right]. \tag{193}$$

The visibility of the fringes being defined by

$$v = \left(\frac{e(p,q)_{\max} - e(p,q)_{\min}}{e(p,q)_{\max} + e(p,q)_{\min}}\right), \tag{194}$$

we find

$$v = |\gamma(B)| = |FT[O''(r)](B)|. \tag{195}$$

We have thus recovered the important result (i.e. the Zernicke-van Cittert Theorem), first established for the case of two point-like apertures, according to which the visibility of the fringes is the Fourier transform of the normalized intensity distribution of the source.

It is now good to distinguish two cases.

Let us first assume that the observed extended source is symmetric with respect to the y (or equivalently s) axis. In that case, the normalized intensity distribution $O''(r)$ of the source slice at r is a symmetric function of r and given that the Fourier transform of a symmetric function is even, we find that the complex degree of mutual coherence expressed by Eq. (192) is even and that consequently the angle $\beta = 0$ or $\beta = \pi$. In practice, this means that the white fringe is observed at its expected position $p = 0$.

The general case is that of a celestial source being characterized by an asymmetric source intensity distribution $O(p,q)$ such that $\beta \neq 0$. There will then result a systematic phase shift of the position of the fringe pattern in the focal plane of the instrument in accordance with Eq. (193). Recovering the value of that phase shift β provides additional information in order to characterize the intensity source profile $O(p,q)$.

Simulations illustrating the Zernicke-van Cittert theorem for the cases of a circular and two triangular shaped celestial sources have been prepared using the Geogebra open source applications (https://www.geogebra.org). They can be viewed on the video Visibility_Asymmetric_Source.mp4 to be downloaded via the URL: https://orbi.uliege.be/handle/2268/253241.

We describe hereafter some of the techniques used to retrieve the source angle β when observing an extended source with an interferometer.

7.2.4 Measurement of the intrinsic source phase angle β

(i) First difficulty: precise pointing of the telescopes

Let us consider the case of an interferometer composed of two similar apertures characterized by the complex amplitude distribution $A_0(x,y)$ and separated along the x axis by the baseline

length B. Let us also assume that we are not observing a point-like star perfectly aligned along the optical axis of the individual telescope apertures but slightly inclined, i.e. its angular position with respect to the optical axis is given by

$$\begin{aligned} \zeta_0 &= x'_0/f = x'_0\lambda/(f\lambda) = p_0\lambda, \\ \eta_0 &= y'_0/f = y'_0\lambda/(f\lambda) = q_0\lambda. \end{aligned} \tag{196}$$

Reminding Eqs. (144) & (145) and the properties of the Fourier transform (product, translation, convolution, ...), it is then easy to establish that the distribution of the complex amplitude in the focal plane is successively given by

$$\begin{aligned} a(p,q) &= FT[(A_0(x-B/2,y) + A_0(x+B/2,y))\exp(i2\pi(xp_0+yq_0))](p,q), \\ &= FT[(A_0(x-B/2,y) + A_0(x+B/2,y))](p,q) * FT[\exp(i2\pi(xp_0+yq_0))](p,q), \\ &= [2\cos(\pi pB)FT[A_0(x,y](p,q)] * \delta(p-p_0,q-q_0), \\ &= 2\cos[\pi(p-p_0)B]FT[A_0(x,y](p-p_0,q-q_0)]. \end{aligned} \tag{197}$$

The response function of the interferometer is thus given by the expression

$$i(p,q) = 4\cos^2[\pi B(p-p_0)]\, FT^2[A_0(x,y)](p-p_0,q-q_0). \tag{198}$$

The conclusion is that the positioning of the fringes produced by a star in the focal plane of the interferometer is sensitive to the pointing of the telescopes. Let us however notice that the fringes remain fixed with respect to the point spread function of the individual apertures which position in the focal plane also depends on the star position.

(ii) Second difficulty: the atmospheric piston effect

Although adaptive optics will correct for any atmospheric wavefront deformations over each single aperture, there will remain a differential atmospheric piston over the two single apertures (see Figure 62). Indeed, the effect of the atmosphere is to induce an unknown phase delay φ over each telescope aperture of the interferometer.

The distribution of the complex amplitude in the focal plane of the interferometer will then be successively given by

$$\begin{aligned} a(p,q) &= FT[A_0(x-B/2,y)\exp(i\varphi_1) + A_0(x+B/2,y)\exp(i\varphi_2)](p,q), \\ &= \exp\frac{i(\varphi_1+\varphi_2)}{2}[\exp\frac{i(\varphi_1-\varphi_2)}{2}\exp(-i\pi Bp) + \exp\frac{-i(\varphi_1-\varphi_2)}{2}\exp(i\pi Bp)]FT[(A_0(x,y)](p,q), \\ &= \exp\frac{i(\varphi_1+\varphi_2)}{2}\cos[\pi Bp + \frac{(\varphi_2-\varphi_1)}{2}]\,2FT[(A_0(x,y)](p,q). \end{aligned} \tag{199}$$

In this case, the response function of the interferometer becomes

$$i(p,q) = |a(p,q)|^2 = \cos^2[\pi Bp + \frac{(\varphi_2-\varphi_1)}{2}]\,4FT^2[(A_0(x,y)](p,q). \tag{200}$$

Here also we see that the precise positioning of the fringes produced by a star will be affected by the time variable atmospheric piston above the two apertures. There will result very fast translational motions of the fringes in the focal plane of the interferometer and in order to integrate the fringes, use of a fringe tracker will be mandatory.

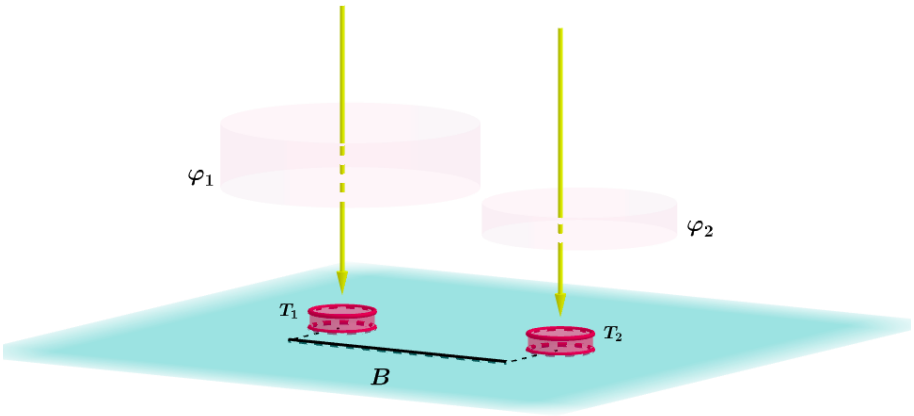

Figure 62. Differential atmospheric piston effect. The difference in height of the atmospheric layers at various positions over the ground will affect the complex amplitude of the electromagnetic field by the constant phase shifts φ_1 and φ_2 over the two individual telescope apertures (T_1 and T_2) of the interferometer.

(iii) The solutions

If the main target is close to a reference star, hopefully brighter, located in the same isoplanetic field of view, we could of course measure the differential positioning of the fringes of the main target with respect to those due to the reference star which would be similarly affected by the atmospheric piston effect.

Another possibility would be that we try to resolve an extended region associated with a point-like component pertaining to the target of interest. For instance, a bright extended emission line region superimposed over a point-like component. In that case, we would take as the reference object the point-like component well detected in its spectral continuum.

Another very cute solution that has been inspired from radio interferometry is to observe the target of interest simultaneously with at least three independent apertures (see Figure 63).

Indeed, from the precise positioning of the three independent sets of fringes observed in the focal plane of the interferometer, we would measure the phase angles Φ_{12}, Φ_{23} and Φ_{31} which expressions are related to the intrinsic source phases β_{12}, β_{23} and β_{31} (see Eqs. (114), (116) and (118)) and to the phases ϕ_{12}, ϕ_{23} and ϕ_{31}, induced by the differential atmospheric pistons as well as by instrumental effects associated with each pair of apertures:

$$\begin{aligned} \Phi_{12} &= \beta_{12} + \phi_{12}, \\ \Phi_{23} &= \beta_{23} + \phi_{23}, \\ \Phi_{31} &= \beta_{31} + \phi_{31}. \end{aligned} \tag{201}$$

Since (see Eq. (200))

$$\phi_{12} + \phi_{23} + \phi_{31} = \frac{\phi_2 - \phi_1}{2} + \frac{\phi_3 - \phi_2}{2} + \frac{\phi_1 - \phi_3}{2} = 0, \tag{202}$$

we obtain the interesting relation

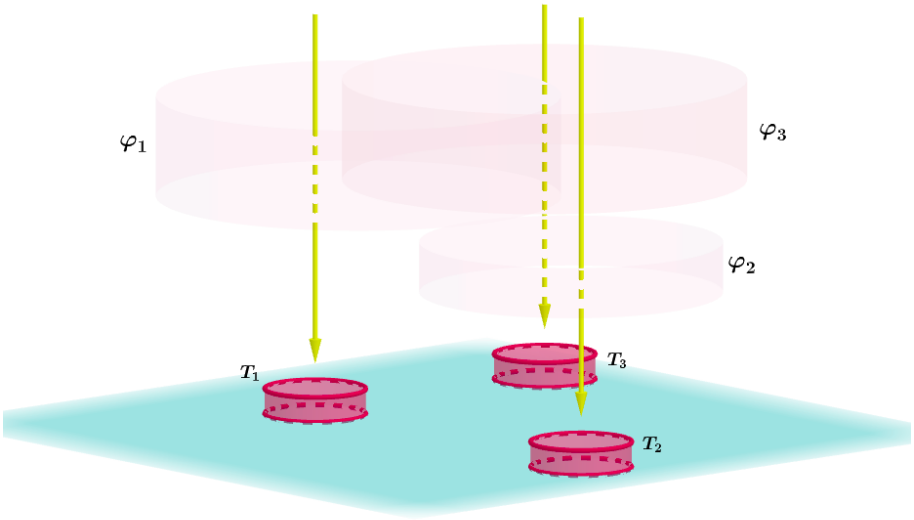

Figure 63. Differential atmospheric piston effects over a three telescope aperture (T_1, T_2 and T_3) interferometer (see text).

$$\Phi_{12} + \Phi_{23} + \Phi_{31} = \beta_{12} + \beta_{23} + \beta_{31}. \tag{203}$$

So from simultaneous interferometric observations with 3 telescope apertures, we are capable to establish one constraint on the intrinsic source phase angles β_{12}, β_{23} and β_{31}. Such a sum of Fourier phase angles around a close loop of baselines is called a *closure phase*. Interferometrists also refer to the *closure phase* as the argument of the *triple product of the complex visibilities* associated with each of the three baselines, or to as the *bispectrum*.

Let us also note that the closure phase is insensitive to the precise angular position ζ_0, η_0 (see Eq. (196)) of the source in the focal plane. Indeed, assuming that we are simultaneously observing the source with the three apertures such that the three projected baseline vectors on the (u, v) plane are such that

$$\mathbf{U_{12}} + \mathbf{U_{23}} + \mathbf{U_{31}} = \mathbf{0}, \tag{204}$$

we then also have

$$\mathbf{U_{12}}.\mathbf{Z_0} + \mathbf{U_{23}}.\mathbf{Z_0} + \mathbf{U_{31}}.\mathbf{Z_0} = (\mathbf{U_{12}} + \mathbf{U_{23}} + \mathbf{U_{31}}).\mathbf{Z_0} = 0, \tag{205}$$

where $\mathbf{Z_0}$ (ζ_0, η_0) represents the angular position vector of the source offset from the optical axis, projected on the plane of the sky.

If we would make use of N telescope apertures, we should be able to set $(N-1)(N-2)/2$ constraints on the $N(N-1)/2$ intrinsic source phase angles associated with the observed source. For the case of non redundant baselines, the fraction Fr of intrinsic source phase information retained by the closure phases is a steadily increasing function of the number of telescopes composing the interferometric array:

$$Fr = \frac{N-2}{66\,N}. \tag{206}$$

For $N = 3$, we find that $Fr = 33.333...\%$, for $N = 6$ (cf. the Charra Array), $Fr = 66.666...\%$ and for $N = 66$ (cf. the ALMA Array), $Fr = 96.969...\%$.

7.3 The Wiener-Khinchin theorem

Finally, the Wiener-Khinchin theorem allows one to easily figure out what is the space frequency content of the point spread function for a given entrance pupil of an optical instrument. We may then directly find out which information is recoverable in terms of space frequency when observing an extended source.

The Wiener-Khinchin theorem merely states that the Fourier transform of the response function of an optical system, i.e. the Fourier transform of the Point Spread Function in our case, is given by the auto-correlation of the distribution of the complex amplitude in the pupil plane. In mathematical terms, the theorem can be expressed as follows

$$FT[|a(p,q)|^2](x,y) = FT[i(p,q)](x,y) = \int_{-\infty}^{+\infty}\int_{-\infty}^{+\infty} A^*(x'+x,y'+y)A(x',y')dx'dy'. \quad (207)$$

When establishing the expression (180), we wrote that the quantity $FT[|a(p,q)|^2]$ appearing in its denominator could be retrieved from the observation of a point-like star. The Wiener-Khinchin theorem states that it can also be retrieved from the auto-correlation of the distribution of the complex amplitude $A(x,y)$ in the pupil plane. Figure 64 illustrates the application of this theorem to the case of an interferometer composed of two circular apertures having a diameter a and separated by the baseline B. We see that the autocorrelation of an interferometer gives access to high space frequencies.

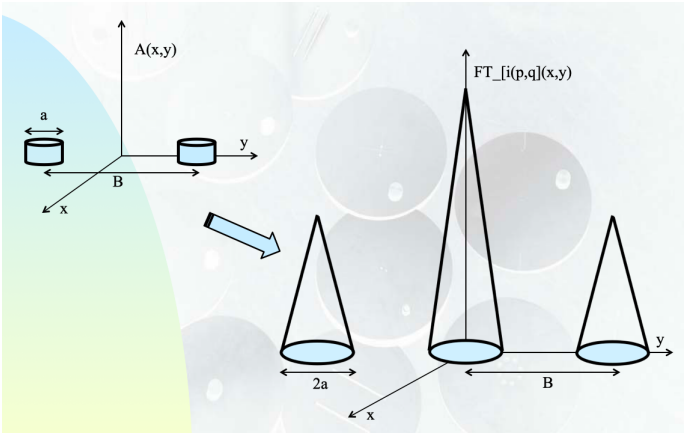

Figure 64. Diagram representing the autocorrelation function versus the space frequency, for a two telescope interferometer, each having a diameter a, separated by the baseline B.

A simple demonstration of the Wiener-Khinchin theorem (207) is given below.
We may successively establish that

$$FT[i(p,q)](x,y) = FT[|a(p,q)|^2](x,y) = FT[a^*(p,q)a(p,q)](x,y), \quad (208)$$

$$FT[i(p,q)](x,y) = \int\int \exp[-2i\pi(px+qy)] \int\int A^*(x'',y'')\,\exp[2i\pi(px''+qy'')]\,dx''dy'' \int\int A(x',y')\,\exp[-2i\pi(px'+qy')]\,dx'dy'dpdq, \quad (209)$$

$$FT[i(p,q)](x,y) = \int\int \exp[(2i\pi\{p[x'' - (x' + x)] + q[y'' - (y' + y)]\})] \int\int A^*(x'',y'')\,dx''dy'' \int\int A(x',y')\,dx'dy'dpdq \tag{210}$$

and taking into account the definition (87) of the Dirac distribution

$$FT[i(p,q)](x,y) = \int\int\int\int \delta[x''-(x'+x)]\,\delta[y''-(y'+y)]\,A^*(x'',y'')\,A(x',y')\,dx'dy'dx''dy''. \tag{211}$$

We finally find that

$$FT[i(p,q)](x,y) = \int\int A^*(x' + x, y' + y)\,A(x',y')\,dx'dy' = \int_{-\infty}^{+\infty}\int_{-\infty}^{+\infty} A^*(x' + x, y' + y)\,A(x',y')\,dx'dy', \tag{212}$$

i.e. the quoted result, namely that the Fourier transform of the impulse response function of an optical system can be represented by the autocorrelation of the distribution of the complex amplitude $A(x, y)$ in the pupil plane.

7.4 Appendix

In this appendix, we detail the calculations leading from Eqs. (163)-(164) to Eq. (165).

First of all, we proceed with the following change of variables in the expression of $FT[A_1(x)](p)$: $y = -x, dy = -dx$. We then replace y by x and dy by dx. Putting the factor $\exp[i\pi d/\lambda]$ in evidence, the summation of $FT[A_1(x)](p)$ and $FT[A_2(x)](p)$ leads to

$$\begin{aligned} a(p) = \exp[i\pi(d/\lambda)]\{\exp[-i\pi(d/\lambda)]M\exp[-i\pi M\sin[\theta_0](B/M - B')/\lambda]\cdot \\ \int_{(B'-D/M)/2}^{(B'+D/M)/2}\exp[2i\pi x(p - M\sin[\theta_0]/\lambda)]dx + \\ \exp[i\pi(d/\lambda)]M\exp[i\pi M\sin[\theta_0](B/M - B')/\lambda]\cdot \\ \int_{(B'-D/M)/2}^{(B'+D/M)/2}\exp[-2i\pi x(p - M\sin[\theta_0]/\lambda)]dx\} \end{aligned} \tag{213}$$

and subsequently

$$\begin{aligned} a(p) = M\exp[i\pi(d/\lambda)]\int_{(B'-D/M)/2}^{(B'+D/M)/2}\{\exp[i\pi[2x(p - M\sin[\theta_0]/\lambda) - (d + M\sin[\theta_0](B/M - B')] + \\ \exp[-i\pi[2x(p - M\sin[\theta_0]/\lambda) - (d + M\sin[\theta_0](B/M - B')]dx\}, \end{aligned} \tag{214}$$

$$a(p) = 2M\exp[i\pi(d/\lambda)]\int_{(B'-D/M)/2}^{(B'+D/M)/2}\cos[\pi[2x(p - M\sin[\theta_0]/\lambda) - (d + M\sin[\theta_0](B/M - B')]dx. \tag{215}$$

Let us now make use of the change of variables
$z = \pi[2x(p - M\sin[\theta_0]/\lambda) - (d + M\sin[\theta_0](B/M - B')]$ such that $dx = dz/[2\pi(p - M\sin[\theta_0]/\lambda)]$, Eq. (215) then transforms into

$$\begin{aligned} a(p) = \frac{2M\exp[i\pi(d/\lambda)]}{2\pi(p - M\sin[\theta_0]/\lambda)}\{\sin[\pi\{(B' + D/M)(p - M\sin[\theta_0]/\lambda) - (d + M\sin[\theta_0](B/M - B'))/\lambda\}] \\ - \sin[\pi\{(B' - D/M)(p - M\sin[\theta_0]/\lambda) - (d + M\sin[\theta_0](B/M - B'))/\lambda\}]\}, \end{aligned} \tag{216}$$

and still

$$\begin{aligned} a(p) = \frac{D\exp[i\pi(d/\lambda)]}{\pi D[p - M\sin[\theta_0]/\lambda]/M}\{\sin[\Gamma + \Lambda] - \sin[\Gamma - \Lambda]\}, \\ \text{with } \Gamma = \pi\{B'(p - M\sin[\theta_0]/\lambda) - (d + M\sin[\theta_0](B/M - B'))/\lambda\}, \\ \text{and } \Lambda = \pi D(p - M\sin[\theta_0]/\lambda)/M. \end{aligned} \tag{217}$$

Making use of the well known relation $\sin(\Gamma + \Lambda) - \sin(\Gamma - \Lambda) = 2\cos(\Gamma)\sin(\Lambda)$, the previous equation reduces to

$$\begin{aligned} a(p) = 2D\exp[i\pi(d/\lambda)]\frac{\sin[\pi D[(p - M\sin[\theta_0]/\lambda)]/M]}{\pi D[(p - M\sin[\theta_0]/\lambda)]/M}\cdot \\ \cos[\pi\{B'(p - M\sin[\theta_0]/\lambda) - (d + M\sin[\theta_0](B/M - B'))/\lambda\}] \end{aligned} \tag{218}$$

and since

$$\pi\{B'(p - M\sin[\theta_0]/\lambda) - (d + M\sin[\theta_0](B/M - B'))/\lambda\} = \pi\{B'p + (d - B\sin[\theta_0])/\lambda\}, \quad (219)$$

we finally obtain

$$a(p) = 2D\exp[i\pi(d/\lambda)]\frac{\sin[\pi D[(p - M\sin[\theta_0]/\lambda)]/M]}{\pi D[(p - M\sin[\theta_0]/\lambda)]/M} \cdot \cos[\pi\{B'p + (d - B\sin[\theta_0])/\lambda\}] \quad (220)$$

which is the same result as that quoted in Eq. (165).

References

1. J. Surdej, see http://www.aeos.ulg.ac.be/teaching.php (2018)

2. H. Réboul, *Introduction à la théorie de l'Observation en Astrophysique* (Masson, 1979)

3. P. Léna, D. Rouan, F., Lebrun, F. Mignard, D., Pelat, D., *Observational Astrophysics* (Astronomy and Astrophysics Library, 2012)

4. A. Glindemann, *Principles of Stellar Interferometry* (Astronomy and Astrophysics Library, 2011)

5. D. Buscher, *Practical Optical Interferometry: Imaging at Visible and Infrared Wavelengths* (Cambridge University Press, 2015)